Low Energy Properties of the Antiferromagnetic Quantum Critical Metal in Two Dimensions

Low Energy Properties of the Antiferromagnetic Quantum Critical Metal in Two Dimensions

by

Peter Lunts, M.Sc.

A Thesis
Submitted to the School of Graduate Studies
in Partial Fulfillment of the Requirements
for the degree Doctor of Philosophy

McMaster University

DOCTOR OF PHILOSOPHY, Department of Physics and Astronomy, McMaster University (2017), Hamilton, Ontario.

TITLE: Low Energy Properties of the Antiferromagnetic Quantum Critical Metal in Two Dimensions

AUTHOR: Peter Lunts, M. Sc. (Perimeter Institute and University of Waterloo)

SUPERVISOR: Dr. Sung-Sik Lee

NUMBER OF PAGES: xviii, 83

Abstract

In this thesis, we study the low-energy effective theory for the antiferromagnetic quantum critical metal in two dimensions. The theory has been the subject of intense study for more than twenty years, due to the novel physics of non-Fermi liquid metals and its potential relevance to high-temperature superconductors and heavy-fermion compounds.

In the first part of the thesis, we present the perturbative study of the theory in $3 - \epsilon$ space dimensions by extending the earlier one-loop analysis to higher-loop orders. We show that the ϵ expansion is not organized by the standard loop expansion, and a two-loop graph becomes as important as one-loop graphs even in the small ϵ limit due to an infrared singularity caused by an emergent quasilocality. This qualitatively changes the nature of the infrared fixed point, and the ϵ expansion is controlled only after the two-loop effect is taken into account. Furthermore, we show that a ratio between velocities emerges as a small parameter, which suppresses a large class of diagrams.We show that the critical exponents do not receive quantum corrections beyond the linear order in ϵ in the limit that the ratio of velocities vanishes.

In the second part of the thesis, we present a nonperturbative solution to the theory in two dimensions based on an ansatz that is inspired by the perturbative analysis. Being a strongly coupled theory, it can still be solved reliably in the low-energy limit as quantum fluctuations are organized by the ratio of velocities that dynamically flows to zero in the low-energy limit. We predict the exact critical exponents that govern the universal scaling of physical observables at low temperatures.

Acknowledgments

I am extremely grateful to my advisor Sung-Sik Lee for all the training, mentoring, and guidance he provided throughout these years. I particularly value all the hours he gave to discuss problems with me, always willing to lend his time, no matter how tedious it was or how much I asked of him. Most importantly, his philosophy and attitude towards science and his work in general will continue to inspire me, in anything I do.

I would like to thank my other main collaborator, Andres Schlief. It was truly great to work with him. He is not only a great collaborator, but a great friend. I am very happy that we spent so much time together, and got to know each other so well.

During my time at Perimeter, I have made many friends, and I have enjoyed my time with all of them. I would like to thank Anton, Anushya, Carlos, Chris, Clement, Dalimil, Gabriel, Heidar, Holger, João, Julian, Markus, Martin, Max, Mehdi, Miles, Nima, Pablo, Pedro, Ross, Sedigh, Shouvik, Siavash, Subhro, Wen, and Will. I would also like to thank my great friends Danny, Bobby and Chris for supporting me and making efforts to see me despite the distances.

I owe everything to my parents. I still continue to discover just how much they have taught me. I would not have completed my studies, had they not taught me the value of an education and showed me the happiness that comes with learning. I cannot thank them, my grandmother and my sisters enough for their continual support and encouragement during these years. My sisters in particular made every effort to make it seem like we are still living in the same house.

Most of all, I thank Lauren for everything, everything, everything.

Contents

List of Figures

List of Tables

Declaration of Authorship

This thesis is based on two published works, which are summarized in

- Chapter 2

  P. Lunts, A. Schlief, and S.-S. Lee, *Emergence of a control parameter for the antiferromagnetic quantum critical metal*, Phys. Rev. B 95, 245109 (2017)

- Chapter 3

  A. Schlief*, P. Lunts*, and S.-S. Lee, *Exact Critical Exponents for the Antiferromagnetic Quantum Critical Metal in Two Dimensions*, Phys. Rev. X 7, 021010 (2017)
  *co-first authors.

In the first paper, Peter Lunts performed most of the calculations and wrote the draft with Sung-Sik Lee. Andres Schlief performed some of the calculations, and was responsible for Appendix E (Appendix A V). Sung-Sik Lee provided guidance. All authors discussed the work extensively and edited the draft.

In the second paper, Peter Lunts and Andres Schlief each performed roughly half of the calculations, with help from Sung-Sik Lee. Peter Lunts was largely responsible for the calculations in Appendices A and C (Appendices B I and B III), and Andres Schlief was largely responsible for the calculations in Appendices B and D (Appendices B II and B IV). Sung-Sik Lee provided guidance and wrote the draft. All authors discussed the work extensively and edited the draft.

Dedicated to my parents

Chapter 1

Introduction

Phase transitions are one of the most fascinating topics in physics [1], with a long history and an application in many seemingly unrelated areas of physics, and even in non-science disciplines [2]. In condensed matter, they are a central area of research, and will continue to be, as long as new phases of matter are being discovered.

First order, or discontinuous, phase transitions are not particularly interesting from a theoretical perspective. This is because discontinuous phase transitions contain only a finite correlation length, and therefore cannot be "universal", i.e. independent of the microscopic details. Second order, or continuous, phase transitions, on the other hand, have a divergent correlation length, and they are believed to have universality: they can be entirely characterized by the symmetries and topologies of both phases and the dimension. Universality is a very powerful idea, as it enables the characterization of phase transitions in a huge number of systems and materials within a universality class by the study of a single theory.

Among continuous phase transitions, arguably the most interesting are *quantum phase transitions* (QPTs) [3]. QPTs are driven not by the thermal fluctuations, but by the inherent quantum fluctuations arising from the particle-wave duality, which are present even at zero temperature. Quantum fluctuations allow for more variety in QPTs, and a very rich set of universality classes has already been found that have no analogue in classical phase transitions[3, 4]. The critical behavior at the zero temperature *quantum critical point* (QCP) controls the physics not only at the critical point but also within the region at finite temperatures inside the "quantum critical fan", as shown in Fig. 1.1.

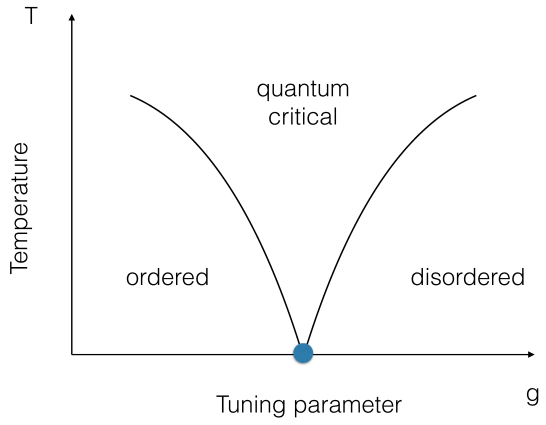

Figure 1.1: A schematic phase diagram of a quantum phase transition.

QPTs in insulators are relatively simple: at the QCP the only low energy degree of freedom is the order parameter. Metals, on the other hand, contain a Fermi surface (FS), whose low energy excitations can interact with the order parameter. Theories of QCPs in metals must therefore necessarily include these excitations and interactions, which increases the complexity of the problem. Here we focus on metals in two spatial dimensions, where quantum fluctuations are strong at low energies. In metals near QCPs, the order parameter is strongly dressed by the

particle-hole excitations near the FS, but the behavior of the fermions in turn is expected to be heavily modified by the interactions with the order parameter. In other words, the conventional theory of metals, known as Landau Fermi liquid theory [5], is expected to break down due to the strong quantum fluctuations of the order parameter, leading to a *non-Fermi liquid* (nFL). In the rest of chapter we review the essentials of Fermi liquid theory, and the different scenarios for realizing nFLs at a QCP.

I Fermi Liquids

Landau Fermi liquid theory [5] is the canonical description of conventional metals. The main assumption is that the interactions are short range, which is valid in most metals, where the Coulomb interaction is rendered short ranged by screening. Under this assumption, Landau postulated that the low energy excitations near the FS are quasiparticles, which carry the same statistics and quantum numbers as the non-interacting fermions, but have a renormalized mass and a finite lifetime. The lifetime τ of the quasiparticles grows with proximity to the FS as $\tau \propto |\vec{k} - \vec{k}_F|^{-2}$ where k is its momentum and k_F is the Fermi momentum, which grows faster than the timescale associated with its energy that grows as $\propto |\vec{k} - \vec{k}_F|^{-1}$. Therefore, at lower energies, the quasiparticles are more stable, and Landau's picture becomes more precise.

The degree of quasiparticle stability can be quantified using the spectral function of the fermionic excitations, $A(\omega, \vec{k}) \equiv -2\text{Im}\, G^R(\omega, \vec{k})$, where $G^R(\omega, \vec{k})$ is the retarded Green's function. The spectral function can be decomposed as $A(\omega, \vec{k}) = 2\pi Z \delta(\omega - \epsilon(\vec{k})) + A'(\omega, \vec{k})$, where $\epsilon(\vec{k})$ is the energy of the fermion, and $A'(\omega, \vec{k})$ is the incoherent part[6]. Z is called the "quasiparticle weight" and it is the overlap between the quasiparticle and the bare fermion. Without interactions, $A'(\omega, \vec{k})$ would vanish, and $Z = 1$. In the presence of interactions Z decreases, but as long as $Z > 0$ and there is a finite overlap, the quasiparticle picture put forth by Landau holds.

Landau's theory was initially postulated, and only after was properly derived using many-body techniques [7]. Later, it was also explained using the renormalization group (RG) approach [8, 9]. Similar to Wilson's RG [10], fermions with higher energies, i.e. further away from the FS, are integrated out to renormalize fermions closer to the FS. The energy cutoff of the fermions Λ is made smaller relative to the size of the FS K_F, as in Fig. 1.2.

At low energies, with $\Lambda/K_F \to 0$, all excitations are very close to the FS, and the scattering due to the local four-fermion interaction is highly restricted. Specifically, only forward scattering and BCS scattering survive, thus leading to coherent quasiparticles which undergo a superconducting phase transition at low enough temperatures.

Fermi liquid theory predicts scaling forms of many observables at low temperature, such as the electrical resistivity $\rho \sim \rho_0 + AT^2$ and specific heat $C \sim \gamma T$. These signatures have

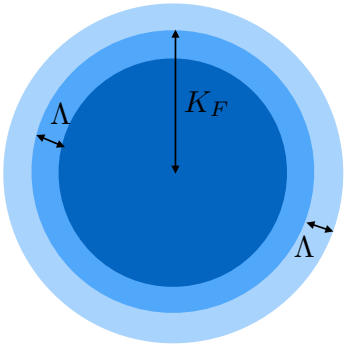

Figure 1.2: The RG scheme based on Wilson, which is used in Ref. [8]. K_F is the Fermi momentum, and the middle circle denoted to have the radius K_F is the Fermi surface. The inner and outer circles have radii $K_F \pm \Lambda$, respectively, where Λ is a UV cutoff. The low energy theory describes excitations in the region between the inner and outer circles. As $\Lambda/K_F \to 0$, this region shrinks, restricting the phase space available for scattering.

been observed in conventional metals[11], and therefore the experimental observation of different scaling forms of resistivity and specific heat are a strong indication that Landau theory is breaking down[12].

II Non-Fermi Liquids

II-1 Description

Non-Fermi liquids are metallic states that do not fall under the quasiparticle picture. They can be defined most easily as states with $Z = 0$. They arise most naturally when an additional gapless bosonic degree of freedom mediates a singular interaction between fermions. This is precisely the situation at QCPs, where the gapless boson is the order parameter interacting with the fermions [13, 14]. Additionally, there are other systems, where the gapless boson is present in an extended region of parameter space at zero temperature, providing a critical phase: the gapless boson can be an emergent gauge field interacting with a spinon Fermi surface [15–22], or a Goldstone mode in a symmetry broken phase where the generators of the broken symmetry group do not commute with the translation operators, such as a phase where magnetic translation is broken [23]. From now on we focus on the nFLs at QCPs.

From a theoretical perspective, the most interesting case is that of two spatial dimensions. In

higher dimensions, the quantum fluctuations of the order parameter are weaker, and the deviation from Fermi liquid behavior is expected to be small. On the other hand, in one dimension, there are only isolated Fermi points instead of a Fermi surface [24–27]. The same challenges and new physics that comes with an extensive number of gapless modes are absent in one dimension. As a result, the low energy physics of metals in one dimension is often described by relativistic field theories. The dimension of two is a sweet spot: the strong quantum fluctuations of the order parameter interact with infinitely many gapless modes, and we expect strong deviations from Fermi liquid theory to arise there. The rest of this thesis is devoted to studying two dimensional theories.

Various QCPs lead to different classes of nFLs in two dimensions, depending on the properties of the symmetry broken state, specifically the ordering wavevector $\vec{Q}$ of the order parameter. If $\vec{Q} = 0$, the critical fluctuations of the order parameter scatter fermions on all points on the Fermi surface, thus creating a "hot Fermi surface". This is the case in ferromagnetic [28] and nematic [29] QCPs. If $\vec{Q} \neq 0$, the order parameter scatters fermions only between isolated points on the Fermi surface that are connected by $\vec{Q}$, called "hot spots", at low energies. This is the case in charge density wave [30] and spin density wave [31–33] QCPs. The latter is the main subject of this thesis. Before focusing on it, we will review the theoretical progress which has been made in general nFL theories.

II-2 Summary of past progress

Theories of a two dimensional Fermi surface interacting with a critical boson are notoriously difficult problems. If one integrates out the boson, and tries to apply the approach of Shankar [8, 9], the long-range effective interactions between fermions results in the proliferation of non-forward scatterings, which is hard to keep track of. On the other hand, if one integrates out the fermions, and tries to study the Ginzburg-Landau type action for the collective mode using Hertz-Millis theory[13, 14], the gapless fermions induce infinitely many marginal interactions between the bosons, which renders this approach intractable as well. Therefore, all gapless degrees of freedom must be kept to describe the low-energy physics based on a local effective field theory. The form of the interaction between fermions and boson is of the Yukawa type, $g\,\phi\,\psi^\dagger\psi$. The interaction strength g is a relevant coupling in two dimensions, and treating the theory perturbatively from the Gaussian fixed point is not a viable option. In order to include the quantum effects in a controlled manner, many approaches have been used, and we summarize them briefly here, in chronological order.

The first approach has focused on the flavor number N of the fermions [18, 19, 34]. In real systems, it is fixed to be a small number $N \sim \mathcal{O}(1)$. However, one can generalize N to arbitrary values, and then there are two options. The first is to use N itself as a small tuning parameter and expand about the $N \to 0$ theory with Nk_F fixed [18, 35]. This amounts to ignoring the

physics of the Fermi surface relative to that of the order parameter. However, it is not clear if the $N \to 0$ results are smoothly connected to the results at $N \sim \mathcal{O}(1)$, because the $N \to 0$ limit reduces the number of gapless fermion modes to a finite number. The other option is to take the $N \to \infty$ limit, as is standard in relativistic field theories [18, 19, 34]. In this limit the fermionic excitations would dominate the physics at low energies, which is qualitatively similar to the free case with $g = 0$. That is why the $1/N$ expansion has been used for a long time. However, it was shown later that for all classes of nFL theories this approach is not feasible, as the number diagrams at each order in $1/N$ is infinite, contrary to the naive scaling analysis [36–38].

Other theories have focused an introducing a tuning parameter ϵ into the kinetic term of the boson, $|\vec{q}|^2 \to |\vec{q}|^{1+\epsilon}$ [21, 39]. This approach reduces the effect of the boson by artificially reducing its density of states. It also saves the limit of $N \to \infty$, as the theory is controlled at large N with fixed $\epsilon N \sim \mathcal{O}(1)$ [40]. This procedure is appealing for the additional reason that all the symmetries of the original theory are preserved for all values of ϵ. However, the non-local dynamics of the boson will not be renormalized under the RG procedure, and therefore the low energy physics of the original local theory cannot be correctly captured if the boson acquires an anomalous dimension, as is generally expected to happen[41].

A final perturbative approach that has recently been developed is dimensional regularization, where the dimension of space is tuned to the upper critical dimension to make g marginal. Among them, the co-dimensional regularization scheme of Refs. [42, 43] is the one we choose to focus on, for reasons explained below. In it, the dimension and shape of the Fermi surface is held fixed as the dimension of space increases. This gives a theory in general dimensions where the density of states of the fermions has been reduced. By tuning the theory in this way, fluctuations of both the fermion and boson are reduced, allowing for a controlled approach. Furthermore, the theory remains local at all dimensions, which is a significant advantage over the method of tuning the dynamics. The disadvantage of this extension is that some symmetries of the theory are broken. In the nFL theories with $\vec{Q} = 0$, the global $U(1)$ symmetry is broken down to Z_2 [42]. In the nFL theories with $\vec{Q} \neq 0$, the fermion numbers at pairs of hot spots connected by $\vec{Q}$ are no longer conserved upon extension[43]. In this thesis we use the co-dimensional regularization of Ref. [43] to study the antiferromagnetic (AF) QCP, as we believe that the preservation of locality and number of gapless modes is more crucial than the preservation of the symmetries that are lost in this approach. We will see that the perturbative solution obtained from the co-dimensional regularization is smoothly connected to the non-perturbative solution in two dimensions.

III Antiferromagnetic criticality

The AF QCP is believed to be present in many layered materials. Of the materials, the most prominent are the electron-doped cuprates [44, 45], iron pnictides [46], and heavy fermion compounds [47, 48]. We show their phase diagrams in Fig. 1.3.

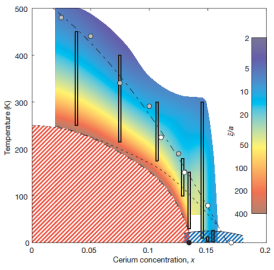

(a) Motoyama et al. (2007)

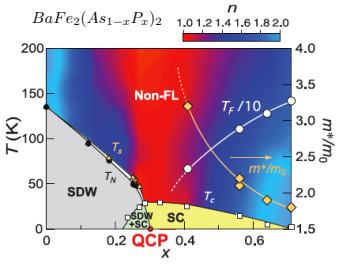

(b) Hashimoto et al. (2012)

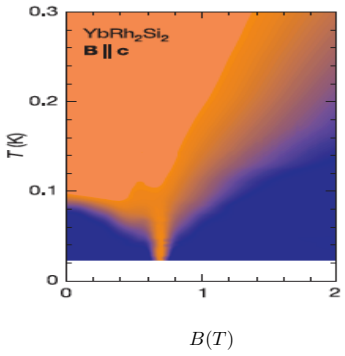

(c) Custers et al. (2003)

Figure 1.3: The phase diagrams of the various materials containing an AF QCP. The figures in (a), (b), (c) are taken from Refs. [45], [46], and [48], respectively.

A key feature of the AF QCP is the FS reconstruction that occurs across the phase transition. In the disordered phase, the shape of the Fermi surface is determined by the underlying band structure. At the critical point, the electrons near the hot spots strongly interact with the gapless AF collective mode. Once the system is tuned into the ordered phase, the electrons at the hot spots become gapped. This breaks the FS into disconnected pockets. We illustrate this in Fig. 1.4, using the FS that is applicable to the cuprates.

Of the material classes mentioned in this section, the electron-doped cuprates and the iron-pnictides are more similar, while the heavy-fermion compounds stand out from the other two. The largest difference is that in addition to the FS and AF fluctuations they contain more degrees of freedom in the form of localized spins that interact with the itinerant electrons. This drastically increases the complexity of the problem. Also, as can be seen in Fig. 1.3(c), the tuning parameter for the transition is often magnetic field, which breaks time reversal symmetry. In

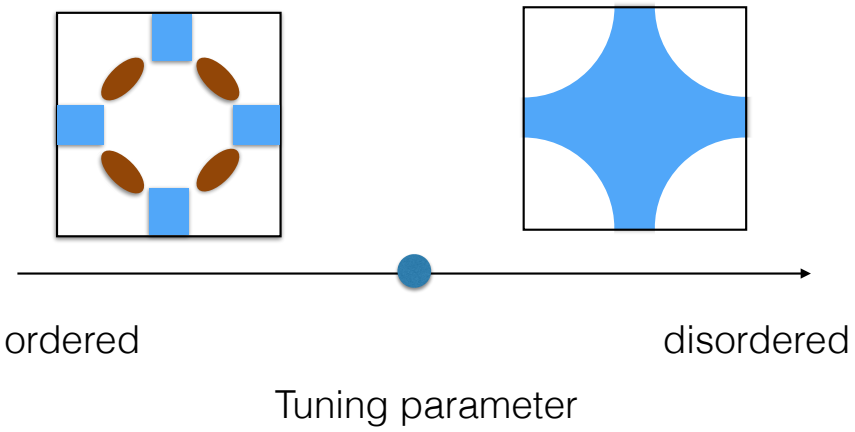

Figure 1.4: The reconstruction of the FS in momentum space across the AF QCP.

order to avoid these complications, we restrict ourselves to studying the AF QCP in the electron-doped cuprates[31, 32] and the iron-pnictides[49, 50], which has time reversal symmetry and no additional degrees of freedom. In order to simplify our study further, we focus on the Fermi surface specific to electron-doped cuprates shown in Fig. 1.5(a), which has only a single band and C_4 symmetry, and we study the most common scenario where the ordering wave vector is commensurate.

Now we write down the action for the AF QCP in two dimensions. The form of this action is dictated by the gapless degrees of freedom, the symmetries present, and the fact that the action must be local in space. The FS in Fig. 1.5(a) has eight hot spots. We take $\vec{Q}_{AF} \equiv \vec{Q} = (\pi, \pi)$,

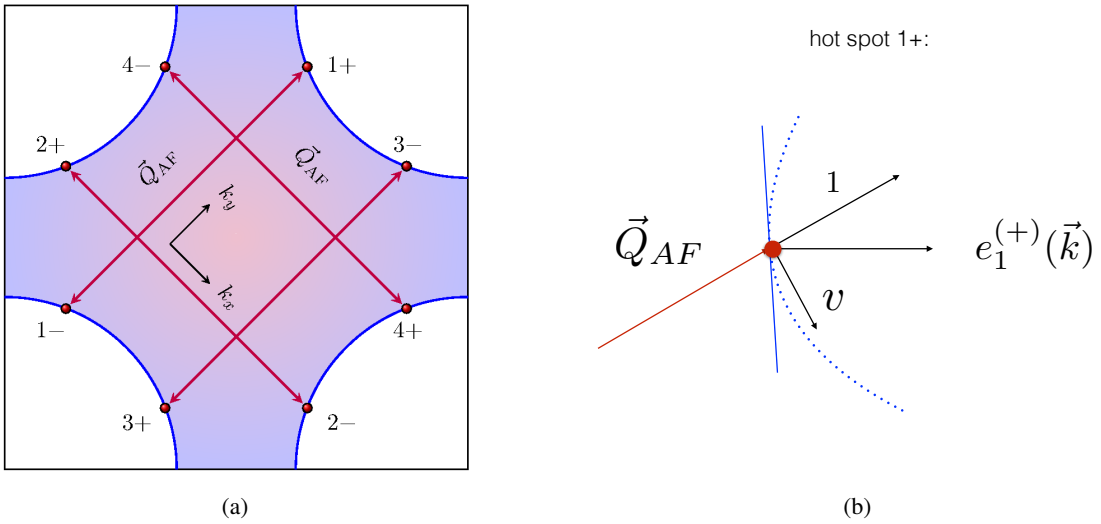

Figure 1.5: a) The first Brillouin zone of a metal in two dimensions with C_4 symmetry. The shaded region represents the occupied states. The AF ordering wavevector $\vec{Q}_{AF}$ is denoted by red arrows. The hot spots are the red dots connected by $\vec{Q}_{AF}$. b) The linearized FS at the hot spot $(1, +)$. The velocities parallel and perpendicular to $\vec{Q}_{AF}$ are set to be 1 and v, respectively. Other hot spots are linearized according to the C_4 symmetry.

which is the most common value of $\vec{Q}_{AF}$ seen in experiments[32]. The commensurate order

ensures that the critical boson field is real. At low energies the relevant degrees of freedom are the fermions near the hot spots interacting with the critical boson, which scatters the fermions between pairs of hot spots. The local action is given by

$$\begin{aligned}\mathcal{S} = \quad & \sum_{n=1}^{4}\sum_{m=\pm}\sum_{\sigma=\uparrow,\downarrow}\int \frac{d^3k}{(2\pi)^3}\,\psi^{(m)*}_{n,\sigma}(k)\left[ik_0 + e^m_n(\vec{k};v)\right]\psi^{(m)}_{n,\sigma}(k) \\ & +\frac{1}{2}\int\frac{d^3q}{(2\pi)^3}\left[q_0^2+c^2|\vec{q}|^2\right]\vec{\phi}(-q)\cdot\vec{\phi}(q) \\ & +g_0\sum_{n=1}^{4}\sum_{\sigma,\sigma'=\uparrow,\downarrow}\int\frac{d^3k}{(2\pi)^3}\frac{d^3q}{(2\pi)^3}\left[\vec{\phi}(q)\cdot\psi^{(+)*}_{n,\sigma}(k+q)\vec{\tau}_{\sigma,\sigma'}\psi^{(-)}_{n,\sigma'}(k)+c.c.\right] \\ & +\frac{u_0}{4!}\int\frac{d^3k}{(2\pi)^3}\frac{d^3p}{(2\pi)^3}\frac{d^3q}{(2\pi)^3}\left[\vec{\phi}(k+q)\cdot\vec{\phi}(p-q)\right]\left[\vec{\phi}(-k)\cdot\vec{\phi}(-p)\right]. \end{aligned} \tag{1}$$

Here, $k=(k_0,\vec{k})$ denotes the Matsubara frequency and the two-dimensional momentum $\vec{k}=(k_x,k_y)$. $\psi^{(m)}_{n,\sigma}$ are the fermion fields that carry spin $\sigma=\uparrow,\downarrow$ at the hot spots labeled by $n=1,2,3,4$, $m=\pm$. From now on, we use a rotated axis in which the ordering wave vector is $\vec{Q}_{AF}=\pm\sqrt{2}\pi\hat{k}_x,\pm\sqrt{2}\pi\hat{k}_y$ up to the reciprocal lattice vectors $\sqrt{2}\pi(\hat{k}_x\pm\hat{k}_y)$. With this choice the fermion dispersions are $e^{\pm}_1(\vec{k};v)=-e^{\pm}_3(\vec{k};v)=vk_x\pm k_y$, $e^{\pm}_2(\vec{k};v)=-e^{\pm}_4(\vec{k};v)=\mp k_x+vk_y$, where $\vec{k}$ is the momentum deviation from each hot spot. This is illustrated in Fig. 1.5(b). The curvature of the Fermi surface can be ignored, since the patches of Fermi surface connected by the ordering vector are not parallel to each other with $v\neq 0$. The Fermi velocity along the ordering vector has been set to unity by rescaling $\vec{k}$. v is the component of Fermi velocity that is perpendicular to $\vec{Q}_{AF}$. $\vec{\phi}(q)$ is the boson field with three components which describes the AF collective mode with frequency q_0 and momentum $\vec{Q}_{AF}+\vec{q}$. $\vec{\tau}$ represents the three generators of the $SU(2)$ group. c is the velocity of the AF collective mode. g_0 is the Yukawa coupling between the collective mode and the electrons near the hot spots, and u_0 is the quartic coupling between the collective modes. All higher order couplings are irrelevant under the Gaussian scaling.

The $1/N$ expansion was initially used to compute the low-energy observables of Eq. (1) [38, 51–53], and for a long time those results were believed to hold qualitatively at $N\sim\mathcal{O}(1)$. The results include that i) $v\to 0$ in the low energy limit, and the hot spots become pairwise nested with each other, ii) both fermion and boson strongly renormalize each other's dynamics, and the dynamical critical exponent at the one-loop order is $z=2$, iii) higher-loop quantum corrections further renormalize z. However, in Ref. [38] it was found that the $1/N$ expansion breaks down and these results are not reliable. We will see that some of the findings of the $1/N$ expansion still hold, but some results are qualitatively modified in the controlled expansion we employ.

III-1 Outline of the thesis

The action in Eq. (1) is the subject of this thesis. In Chapter 1, we extend the work of Ref. [43] in applying the co-dimensional regularization scheme to this problem. We compute the beta functions to higher-loop order than in Ref. [43] for reasons explained therein. We find that the theory is only controlled once these higher-loop effects are taken into account. Additionally, we find a novel control parameter, which suggests that the theory can be controlled even in two dimensions. In Chapter 3, we expand on this suggestion, and work with the theory directly in two dimensions. By relying on the intuition from the results in Chapter 2, we use an interaction-driven scaling and self-consistently show that the theory can indeed be controlled by the new control parameter. This allows us to extract exact critical exponents and low energy observables.

Chapter 2

Emergence of a control parameter for the antiferromagnetic quantum critical metal from the ϵ-expansion

The work of Sur and Lee [43] attempted to understand the AF QCP in a controlled way by using the co-dimensional regularization scheme. For the related problem of the nematic quantum critical metal, the co-dimensional regularization scheme was shown to provide controlled access to the low-energy fixed point [42], unlike the $1/N$ expansion, which was found to break down in Refs. [36, 38]. The upper critical dimension for the AF critical metal is $d = 3$, where from here on d represents the number of space dimensions. Sur and Lee performed a perturbative calculation in $d = 3 - \epsilon$ to the one-loop order. They found a stable fixed point to the leading order in ϵ that is smoothly connected to $\epsilon = 0$. An important feature of their fixed point, is that the system exhibits an emergent locality with vanishingly small velocities along some directions, while a ratio of velocities flows to an order one value. However, at this fixed point, the perturbative expansion is not controlled, as certain higher-loop diagrams are expected to have divergent coefficients[54]. The divergences are caused by the emergent locality which enhances quantum fluctuations at low energies.

In this work, we extend the earlier one-loop analysis to include higher-loop effects. We find that the ϵ-expansion is not simply organized by the number of loops, and certain higher-loop diagrams are enhanced by IR singularities caused by the emergent quasi-locality. As a result, a two-loop diagram qualitatively modifies the nature of the fixed point even to the leading order in ϵ[54]. We show that the ϵ-expansion is controlled with the inclusion of the two-loop effect. Furthermore, the ratio between velocities is shown to flow to zero in the low energy limit, which protects the critical exponents from receiving higher-loop corrections. This is similar to the nematic critical point in d-wave superconductors, where an emergent anisotropy in velocities leads to asymptotically exact results to all orders in the $1/N$ expansion[55].

Following our work in this chapter, we actually managed to solve the problem exactly in two-dimensions, using a non-perturbative ansatz[56], which is the subject of Chapter 3. The ansatz assumes that the structure of the fixed point found in this chapter holds all the way down to $\epsilon = 1$, which is not a-priori guaranteed. According to the non-perturbative solution, the AF collective mode is strongly dressed by particle-hole excitations. In contrast, electrons have zero anomalous dimension, and exhibit a relatively weak departure from the Fermi liquid with dynamical critical exponent $z = 1$. The non-perturbative solution actually applies to more general theories, and the same conclusion holds for the AF quantum critical point in the presence of a one-dimensional Fermi surface embedded in general dimensions, $2 \leq d < 3$[57].

The ϵ-expansion and the non-perturbative solution[56, 57] are independent and complimentary. The former is a brute-force perturbative analysis, which is straightforward but valid only near the upper critical dimension. The latter approach is non-perturbative, and it is based on an ansatz that is confirmed by a self-consistent computation. The agreement of the results from the two different approaches provides an independent justification of the ansatz used in the non-perturbative solution.

I Dimensional regularization

We start by generalizing the theory in Eq. (1) by tuning the number of co-dimensions of the one-dimensional Fermi surface[42, 43, 58]. For this, we pair fermions on opposite sides of the Fermi surface into two component spinors, $\Psi_{1,\sigma} = (\psi^{(+)}_{1,\sigma}, \psi^{(+)}_{3,\sigma})^T$, $\Psi_{2,\sigma} = (\psi^{(+)}_{2,\sigma}, \psi^{(+)}_{4,\sigma})^T$, $\Psi_{3,\sigma} = (\psi^{(-)}_{1,\sigma}, -\psi^{(-)}_{3,\sigma})^T$, $\Psi_{4,\sigma} = (\psi^{(-)}_{2,\sigma}, -\psi^{(-)}_{4,\sigma})^T$. In the spinor basis, the kinetic term for the fermions becomes $S_F = \sum_{n=1}^{4}\sum_{\sigma=\uparrow,\downarrow}\int \frac{d^3k}{(2\pi)^3}\ \bar{\Psi}_{n,\sigma}(k)\left[i\gamma_0 k_0 + i\gamma_1\varepsilon_n(\vec{k};v)\right]\Psi_{n,\sigma}(k)$, where $\gamma_0 = \sigma_y$ and $\gamma_1 = \sigma_x$ (σ_i being the Pauli matrices), $\bar{\Psi}_{n,\sigma} = \Psi^{\dagger}_{n,\sigma}\gamma_0$ with $\varepsilon_1(\vec{k};v) = e_1^+(\vec{k};v)$, $\varepsilon_2(\vec{k};v) = e_2^+(\vec{k};v)$, $\varepsilon_3(\vec{k};v) = e_1^-(\vec{k};v)$, $\varepsilon_4(\vec{k};v) = e_2^-(\vec{k};v)$. The general theory in d spatial dimensions reads

$$
\begin{aligned}
\mathcal{S} \;=\; & \sum_{n=1}^{4}\sum_{\sigma=1}^{N_c}\sum_{j=1}^{N_f}\int dk\ \bar{\Psi}_{n,\sigma,j}(k)\Big[i\mathbf{\Gamma}\cdot\mathbf{K} + i\gamma_{d-1}\varepsilon_n(\vec{k};v)\Big]\Psi_{n,\sigma,j}(k) \\
& + \frac{1}{4}\int dq\ \Big[|\mathbf{Q}|^2 + c^2|\vec{q}|^2\Big]\mathrm{Tr}\left[\Phi(-q)\ \Phi(q)\right] \\
& + i\frac{g\mu^{(3-d)/2}}{\sqrt{N_f}}\sum_{n=1}^{4}\sum_{\sigma,\sigma'=1}^{N_c}\sum_{j=1}^{N_f}\int dkdq\ \bar{\Psi}_{\bar{n},\sigma,j}(k+q)\Phi_{\sigma,\sigma'}(q)\gamma_{d-1}\Psi_{n,\sigma',j}(k) \\
& + \frac{\mu^{3-d}}{4}\int dk_1dk_2dq\ \Big[u_1\mathrm{Tr}\left[\Phi(k_1+q)\Phi(k_2-q)\right]\mathrm{Tr}\left[\Phi(-k_1)\Phi(-k_2)\right] \\
& + u_2\mathrm{Tr}\left[\Phi(k_1+q)\Phi(k_2-q)\Phi(-k_1)\Phi(-k_2)\right]\Big]. \qquad (2)
\end{aligned}
$$

Here we consider $SU(N_c)$ spin and N_f flavors of fermions for generality. $k = (\mathbf{K}, \vec{k})$ is the $(d+1)$-dimensional energy-momentum vector with $dk \equiv \frac{d^{d+1}k}{(2\pi)^{d+1}}$. $\vec{k} = (k_x, k_y)$ still denotes the two original momentum components, and $\mathbf{K} = (k_0, k_1, ..., k_{d-2})$ denotes the frequency and the momentum components along the $(d-2)$ co-dimensions that have been added. $\mathbf{\Gamma} = (\gamma_0, \gamma_1, ..., \gamma_{d-2})$ together with γ_{d-1} are the gamma matrices which satisfy the Clifford algebra $\{\gamma_\mu, \gamma_\nu\} = 2I\delta_{\mu,\nu}$ with $\mathrm{Tr}[I] = 2$. $\Psi_{n,\sigma,j}$ with $\sigma = 1, 2, ..., N_c$ and $j = 1, 2, ..., N_f$ is in the fundamental representation of both the enlarged spin group $SU(N_c)$ and the flavor group $SU(N_f)$. $\Phi(q) = \sum_{a=1}^{N_c^2-1}\phi^a(q)\tau^a$ is a matrix field for the collective mode, where τ^a are the generators of $SU(N_c)$ with $\mathrm{Tr}[\tau^a\tau^b] = 2\delta_{ab}$. The Yukawa interaction scatters fermions between pairs of hot spots denoted as $(n, \bar{n})$ with $\bar{1} = 3$, $\bar{2} = 4$, $\bar{3} = 1$, $\bar{4} = 2$. The Yukawa and quartic interactions have scaling dimensions $(3-d)/2$ and $(3-d)$, respectively, at the non-interacting fixed point. μ is the energy scale introduced to make g, u_1, u_2 dimensionless. For $N_c \leq 3$, u_1 and u_2 are not independent couplings because of the identity, $\mathrm{Tr}[\Phi^4] = \frac{1}{2}(\mathrm{Tr}[\Phi^2])^2$.

The energy of the fermions is given by $E_n(k_1, ..., k_{d-2}, \vec{k}) = \pm\sqrt{\sum_{i=1}^{d-2}k_i^2 + \varepsilon_n^2(\vec{k})}$, which supports a one-dimensional Fermi surface embedded in the d-dimensional momentum space. To understand the substance of this generalization, it is instructive to look at the theory in $d = 3$. There, the γ matrices that satisfy the Clifford algebra are chosen to be $(\gamma_0, \gamma_1, \gamma_2) = (\sigma_y, \sigma_z, \sigma_x)$, and we identify $k_1 = k_z$. The kinetic term of the three-dimensional action for the

spinors Ψ_1, Ψ_3 is written in terms of the original fermions $\psi_n^{(m)}$ as

$$H_0 = \sum_{\sigma=1}^{N_c}\sum_{j=1}^{N_f}\int dk\,(vk_x \pm k_y)\left[\psi^{(\pm)*}_{1,\sigma,j}\psi^{(\pm)}_{1,\sigma,j} - \psi^{(\pm)*}_{3,\sigma,j}\psi^{(\pm)}_{3,\sigma,j}\right] \mp k_z\left[\psi^{(\pm)*}_{1,\sigma,j}\psi^{(\pm)}_{3,\sigma,j} + h.c.\right] \quad (3)$$

and the kinetic term for the spinors Ψ_2, Ψ_4 is obtained from Eq. (3) using the C_4 symmetry. Eq. (3) describes an AF QCP in $d = 3$ with a p_z-wave CDW. It is therefore itself a physical theory, which can arise in an experimental setup [43]. The CDW gaps out the Fermi surface in the z-direction, leaving the one-dimensional Fermi surface embedded in three dimensions. To illustrate this, we show the resulting spectrum of the theory in $d = 3$ in Fig. 2.1.

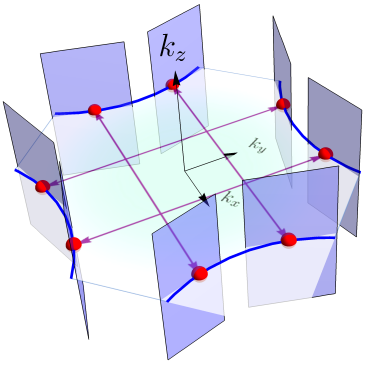

Figure 2.1: The theory in Eq. (2) at $d = 3$. The Fermi surface is still given by the one-dimensional blue lines. The planes at each hot spot are the spectral gap proportional to k_z, which comes from the p_z-wave charge density wave with momentum $2\vec{k}_F$ in Eq. (3).

The theory in Eq. (2) respects the $U(1) \times SU(N_c) \times SU(N_f)$ internal symmetry. It is also invariant under the C_4 transformations in the (k_x, k_y) plane, the $SO(d-1)$ that rotates $(k_0, ..., k_{d-2})$, and time-reversal. When $N_c = 2$, there is an additional pseudospin symmetry, which rotates $\Psi_{n,\sigma,j}(k)$ into $i\tau^{(y)}_{\sigma,\sigma'}\bar{\Psi}^T_{n,\sigma',j}(-k)$[38].

In three spatial dimensions both interactions are marginal, which is a fortunate coincidence. We therefore expand around $d = 3$ using $\epsilon = 3 - d$ as a small parameter. We use the minimal subtraction scheme to compute the beta functions, which dictate the renormalization group (RG) flow of the velocities and couplings. To make the quantum effective action finite in the ultraviolet (UV), we add counter terms which can be written in the following form,

$$\mathcal{S}_{CT} = \sum_{n=1}^{4}\sum_{\sigma=1}^{N_c}\sum_{j=1}^{N_f}\int dk\;\bar{\Psi}_{n,\sigma,j}(k)\left[i\mathcal{A}_1\mathbf{\Gamma}\cdot\mathbf{K} + i\mathcal{A}_3\gamma_{d-1}\varepsilon_n\left(\vec{k};\frac{\mathcal{A}_2}{\mathcal{A}_3}v\right)\right]\Psi_{n,\sigma,j}(k)$$
$$+\frac{1}{4}\int dq\left[\mathcal{A}_4\,|\mathbf{Q}|^2 + \mathcal{A}_5\,c^2\,|\vec{q}|^2\right]\mathrm{Tr}\left[\Phi(-q)\,\Phi(q)\right]$$

$$+i\mathcal{A}_6\frac{g\mu^{(3-d)/2}}{\sqrt{N_f}}\sum_{n=1}^{4}\sum_{\sigma,\sigma'=1}^{N_c}\sum_{j=1}^{N_f}\int dk\,dq\,\left[\bar{\Psi}_{\bar{n},\sigma,j}(k+q)\Phi_{\sigma,\sigma'}(q)\gamma_{d-1}\Psi_{n,\sigma',j}(k)\right]$$
$$+\frac{\mu^{3-d}}{4}\int dk_1\,dk_2\,dq\,\Big[\mathcal{A}_7u_1\mathrm{Tr}\left[\Phi(k_1+q)\Phi(k_2-q)\right]\mathrm{Tr}\left[\Phi(-k_1)\Phi(-k_2)\right]$$
$$+\mathcal{A}_8u_2\mathrm{Tr}\left[\Phi(k_1+q)\Phi(k_2-q)\Phi(-k_1)\Phi(-k_2)\right]\Big], \tag{4}$$

where

$$\mathcal{A}_n\equiv\mathcal{A}_n(v,c,g,u;\epsilon)=\sum_{m=1}^{\infty}\frac{Z_{n,m}(v,c,g,u)}{\epsilon^m}. \tag{5}$$

$Z_{n,m}(v,c,g,u)$ are finite functions of the couplings. The counter terms are computed order by order in ϵ. The general expressions for the dynamical critical exponent, the anomalous scaling dimensions of the fields, and the beta functions of the velocities and couplings are summarized in Section III.

II The modified one-loop fixed point

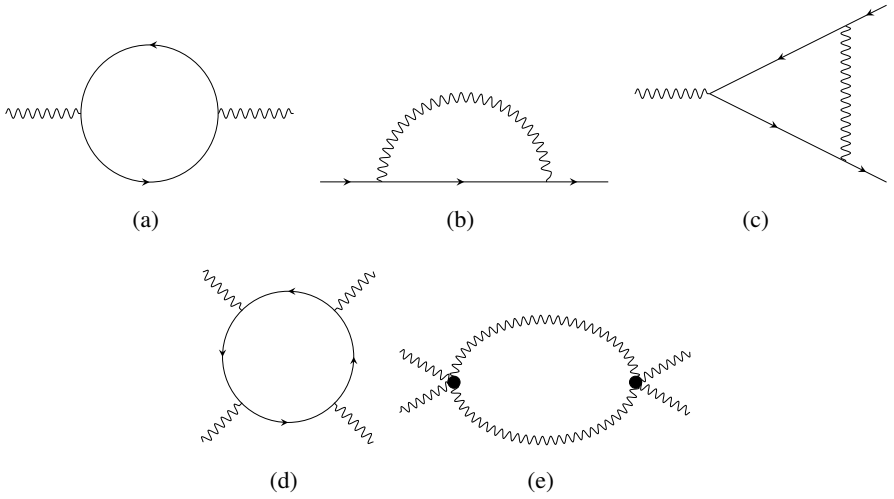

Figure 2.2: One-loop diagrams.

We begin by reviewing the one-loop RG analysis of Ref. [43]. The conclusion of the analysis is that the theory flows to a quasi-local non-Fermi liquid state, where c, v flow to zero as $1/l$ for $d<3$ and as $1/\log(l)$ at $d=3$ in the logarithmic length scale l, with their ratio fixed to be $w\equiv v/c=\frac{N_cN_f}{N_c^2-1}$ in the low energy limit with $l\to\infty$. Along with the emergent quasi-locality, the couplings also flow to zero such that $\lambda\equiv g^2/v$ and $\kappa_i\equiv u_i/c^2$ flow to $\lambda^*=\frac{4\pi(N_c^2+N_cN_f-1)}{N_c^2+N_cN_f-3}\epsilon$ and $\kappa_i^*=0$ in the low energy limit.

The perturbative expansion is controlled by the ratios between the couplings and the velocities, and the dynamical critical exponent becomes $z=1+\frac{N_c^2+N_cN_f-1}{2(N_c^2+N_cN_f-3)}\epsilon$. With $w\sim\mathcal{O}(1)$ at

the one-loop fixed point, general diagrams are estimated to scale as $I \sim \lambda^{\frac{V_g}{2}} \kappa_i^{V_u} c^{V_u - L_b + \frac{E-2}{2}}$, where V_g is the number of Yukawa vertices, V_u is the number of quartic vertices, L_b is the number of boson loops, and E is the number of external lines. Because c flows to zero, magnitudes of higher-loop quantum corrections are controlled not only by λ but also by c. In particular, the quantum correction to the spatial part of the boson kinetic term becomes $\mathcal{A}_5 \sim I/c^2 \sim \lambda^{\frac{V_g}{2}} \kappa_i^{V_u} c^{V_u - L_b - 2}$, where the counter term is further enhanced by a factor of $1/c^2$ because the velocity in the classical action is already small.

In three dimensions ($\epsilon = 0$), all higher-loop diagrams are suppressed because λ flows to zero faster ($\lambda \sim 1/l$) than the velocities ($v \sim c \sim 1/\log(l)$). Therefore, the critical point in three dimensions is described by the stable quasi-local marginal Fermi liquid [59], where the Fermi liquid is broken by logarithmic corrections from the one-loop effect[43]. Below three dimensions ($\epsilon > 0$), however, some higher-loop diagrams cannot be ignored because c flows to zero while $\lambda^* \sim \epsilon$. For example, $\mathcal{A}_5$ from Fig. 2.3 is divergent at the one-loop fixed point. It might seem strange that the higher-loop graph suddenly becomes important for any nonzero ϵ while it is negligible at $\epsilon = 0$. This apparent discontinuity originates from the fact that the small ϵ limit and the low energy limit do not commute. If the small ϵ limit is taken first, all higher-loop graphs are suppressed. However, since we are ultimately interested in the theory at $d = 2$, we fix ϵ to a small but finite value, and then take the low energy limit of the corresponding theory. In this case, c flows to zero, and the IR singularity caused by the softening of the collective mode enhances the magnitude of the two-loop graph. Since certain higher-loop diagrams can be enhanced by the IR singularity in the small c limit, we cannot ignore all higher-order quantum corrections from the outset even in the small ϵ limit.

The largest contribution to the renormalization of c comes from the boson self-energy in Fig. 2.3. We call the addition of this two-loop diagram to the one-loop diagrams (Fig. 2.2) the "modified-one-loop" (M1L) order. As will be shown later, the flow of c is modified by the two-loop graph in Fig. 2.3 such that the effect of other higher-loop diagrams is negligible in the small ϵ limit. There also exists a two-loop diagram made of quartic vertices contributing to $\mathcal{A}_5$. However, the diagram has no enhancement by $1/c^2$ because the momentum dependent self-energy comes with c^2 due to the $(d+1)$-dimensional rotational symmetry present in the bosonic sector. The contribution from the quartic vertices are further suppressed because κ_i is irrelevant at the fixed point.

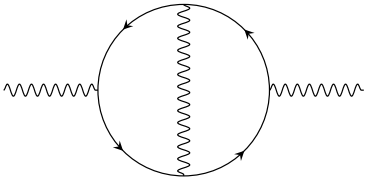

Figure 2.3: Two-loop diagram for the boson self-energy.

Fig. 2.3 gives rise to the quantum effective action whose divergent part is given by

$$\delta\Gamma^{2L}_{0,2} = \frac{1}{\epsilon}\frac{4}{N_c N_f}\frac{g^4}{v^2c^2}h_5(v,c)\int dp\,\frac{1}{4}c^2|\vec{p}|^2\mathrm{Tr}[\Phi(-p)\Phi(p)], \tag{6}$$

where $h_5(v,c)$ is given by $h_5(v,c) = h_5^*\frac{v}{c}$ with $h_5^* \approx 5.7\times10^{-4}$ in the limit $v, c, v/c$ are small. The full definition of $h_5(v,c)$ is given in Appendix A II. The positive sign of Eq. (6) implies that the two-loop correction prevents c from flowing to zero too fast[54]. If c is small, the quantum correction makes the collective mode speed up until the quantum correction becomes $\mathcal{O}(1)$, $\frac{1}{\epsilon}\frac{4}{N_cN_f}\frac{g^4}{v^2c^2}h_5(v,c) \sim 1$. Since $\frac{g^2}{v} \sim \epsilon$, this suggests that $\frac{g^2}{c^3}$ becomes $\mathcal{O}(1)$ in the low energy limit. Once c becomes comparable to $g^{2/3} \sim v^{1/3}$, it flows to zero together with v, although at a slower rate than v. As a result, $w = v/c$ flows to zero at the M1L fixed point for $\epsilon > 0$, unlike at $\epsilon = 0$. This emergent hierarchy in the velocities plays a crucial role in the non-perturbative solution[56, 57]. In order to confirm this picture, we examine the RG flow in the space of $\{\lambda, x, w, \kappa_i\}$, where $x \equiv \frac{g^2}{c^3}$ is expected to flow to an $\mathcal{O}(1)$ value at the fixed point.

The beta functions for the five parameters are expressed in terms of the counter terms as

$$\begin{aligned}
\frac{d\lambda}{dl} &= z\,\lambda\left(\epsilon + Z'_{2,1} + Z'_{3,1} + Z'_{4,1} - 2Z'_{6,1}\right),\\
\frac{dx}{dl} &= z\,x\left(\epsilon + \frac{1}{2}\left(6Z'_{1,1} - 2Z'_{3,1} - Z'_{4,1} + 3Z'_{5,1} - 4Z'_{6,1}\right)\right),\\
\frac{dw}{dl} &= \frac{1}{2}\,z\,w\left(2Z'_{1,1} - 2Z'_{2,1} - Z'_{4,1} + Z'_{5,1}\right),\\
\frac{d\kappa_1}{dl} &= z\,\kappa_1\left(\epsilon + Z'_{4,1} + Z'_{5,1} - Z'_{7,1}\right),\\
\frac{d\kappa_2}{dl} &= z\,\kappa_2\left(\epsilon + Z'_{4,1} + Z'_{5,1} - Z'_{8,1}\right),
\end{aligned} \tag{7}$$

where $Z'_{n,1} \equiv \left(\frac{1}{2}g\partial_g + u_i\partial_{u_i}\right)Z_{n,1}$, and $z = \left[1 + Z'_{1,1} - Z'_{3,1}\right]^{-1}$ is the dynamical critical exponent. In the limit that $v, c, v/c$ are small, the beta functions at the M1L level become

$$\frac{d\lambda}{dl} = z\,\lambda\left(\epsilon - \frac{1}{4\pi}\lambda + \frac{1}{2\pi N_cN_f}\,\lambda w\right), \tag{8}$$

$$\frac{dx}{dl} = z\,x\left(\epsilon - \frac{3N_c^2-7}{8\pi N_cN_f}\,\lambda w + \frac{(N_c^2-1)}{2\pi^2N_cN_f}\,\frac{(\lambda w)^{\frac{3}{2}}}{x^{\frac{1}{2}}} + \frac{1}{8\pi}\lambda - \frac{12\,h_5^*}{N_cN_f}\,\lambda\,x\right), \tag{9}$$

$$\frac{dw}{dl} = \frac{1}{2}\,z\,w\left(-\frac{(N_c^2-1)}{4\pi N_cN_f}\,\lambda w - \frac{(N_c^2-1)}{\pi^2N_cN_f}\,\frac{(\lambda w)^{\frac{3}{2}}}{x^{\frac{1}{2}}} + \frac{1}{4\pi}\lambda - \frac{8\,h_5^*}{N_cN_f}\,\lambda\,x\right), \tag{10}$$

$$\frac{d\kappa_1}{dl} = z\,\kappa_1\left(\epsilon - \frac{1}{4\pi}\lambda - \frac{8\,h_5^*}{N_cN_f}\,\lambda\,x - \frac{1}{2\pi^2}\left((N_c^2+7)\kappa_1 + 2\left(2N_c - \frac{3}{N_c}\right)\kappa_2 + 3\left(1+\frac{3}{N_c^2}\right)\frac{\kappa_2^2}{\kappa_1}\right)\right), \tag{11}$$

$$\frac{d\kappa_2}{dl} = z\,\kappa_2\left(\epsilon - \frac{1}{4\pi}\lambda - \frac{8\,h_5^*}{N_cN_f}\,\lambda\,x - \frac{1}{2\pi^2}\left(12\kappa_1 + 2\left(N_c - \frac{9}{N_c}\right)\kappa_2\right)\right), \tag{12}$$

with $z = \left(1 - \frac{N_c^2-1}{8\pi N_c N_f}\lambda w\right)^{-1}$. The beta functions exhibit a stable fixed point given by

$$\lambda^* = 4\pi\epsilon, \quad x^* = \frac{N_c N_f}{32\pi\, h_5^*}, \quad w^* = 0, \quad \kappa_i^* = 0. \tag{13}$$

It is noted that x is $\mathcal{O}(1)$, and $v, c, v/c$ all vanish at the fixed point.

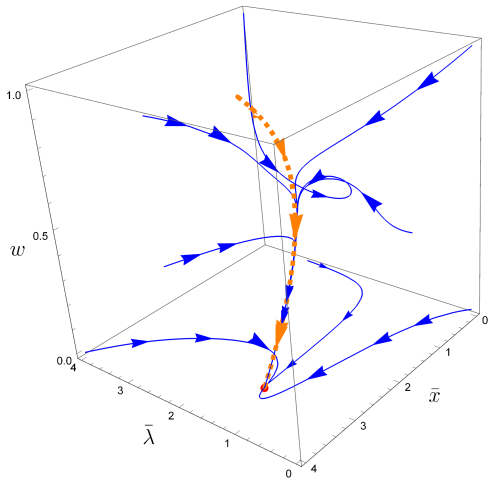

Figure 2.4: The RG flow in the space of (λ, x, w) for $\epsilon = 0.01$ and $N_c = 2, N_f = 1$. The axes are scaled as $\bar{x} \equiv x/10$, $\bar{\lambda} \equiv 10\lambda$. The fixed point $(\bar{\lambda}^*, \bar{x}^*, w^*) = (1.26, 3.49, 0)$ is denoted as a red dot. The solid curves represent the numerically integrated RG flows, and the dotted (orange) line represents the one-dimensional manifold given by $\frac{dx}{dl} = \frac{d\lambda}{dl} = 0$.

In order to understand the flow near the fixed point, we first examine the beta functions for x and λ. Although it may seem arbitrary to focus on the flow of x, λ first with fixed w, this is actually a good description of the full RG flow because the flow of x, λ is much faster than that of w, as will be shown in the following. From Eqs. (8), (9), the beta functions for $(\delta\lambda, \delta x) \equiv (\lambda - \lambda^*, x - x^*)$ are given by

$$\begin{aligned} \frac{d\delta\lambda}{dl} &= f_\lambda(w) - \epsilon\, \delta\lambda + \ldots, \\ \frac{d\delta x}{dl} &= f_x(w) - \frac{N_c N_f}{32\pi\, h_5^*}\left(\frac{48\pi\, h_5^* \epsilon \delta x}{N_c N_f} + \frac{\delta\lambda}{4\pi}\right) + \ldots \end{aligned} \tag{14}$$

to the linear order in the deviation from the fixed point for small w, where $f_\lambda(w) = \frac{d\lambda}{dl}\big|_{\lambda=\lambda^*, x=x^*}$, $f_x(w) = \frac{dx}{dl}\big|_{\lambda=\lambda^*, x=x^*}$, and $\ldots$ represent terms that are higher order in $\delta\lambda, \delta x$. Eq. (14) implies that the perturbations in λ and x are irrelevant at the fixed point, and they flow to w-dependent values exponentially in l. This can be seen from Fig. 2.4, which shows the full numerical solution to the beta functions for (λ, x, w). Once the RG flow reaches the one-dimensional manifold given by $(\lambda, x, w) = \left(\lambda^* + \frac{f_\lambda(w)}{\epsilon}, x^* + \frac{2}{3\epsilon}\left[f_x(w) - \frac{N_c N_f f_\lambda(w)}{128\pi^2\, h_5^* \epsilon}\right], w\right)$, w flows to the fixed point at a slower rate. To compute the flow within this manifold, we set $\frac{d\lambda}{dl} = \frac{dx}{dl} = 0$ in Eq. (7) to express $Z_{1,1}$, $Z_{4,1}$ in terms of $Z_{n,1}$ with $n = 2, 3, 5, 6$. This gives the beta function

for w within the manifold,

$$\frac{dw}{dl} = \frac{2z}{3}\left(-Z'_{2,1} + Z'_{3,1}\right) w, \tag{15}$$

which reduces to

$$\frac{dw}{dl} = -\frac{64\sqrt{2h_5^*}(N_c^2-1)}{3(N_cN_f)^{3/2}}\epsilon^{3/2}\, w^{5/2} \tag{16}$$

to the leading order in w. Because the flow velocity of w vanishes to the linear order in w, w flows to zero as a power-law in the logarithmic length scale, $w \sim l^{-2/3}$. At the fixed point, the quartic couplings are irrelevant and their beta functions become

$$\frac{d\kappa_i}{dl} = -\epsilon\kappa_i, \tag{17}$$

to the leading order in w and κ_i. This confirms that the fixed point in Eq. (13) is stable.

In the small ϵ limit, Eq. (13) does not converge to the one-loop fixed point, $\lambda^* = 0$, $x^* = 0$, $w^* = \frac{N_cN_f}{N_c^2-1}$, $\kappa_i^* = 0$, which represents the correct fixed point at $\epsilon = 0$. Although the beta functions are analytic functions of ϵ, the fixed point is not because the low energy limit and the $\epsilon \to 0$ limit do not commute. One way to understand this non-commutativity is in terms of the 'RG time' that is needed for the flow to approach Eq. (13) for nonzero but small ϵ. In order for w to decrease by a factor of $1/2$, the logarithmic length scale has to change by $\Delta l \sim \epsilon^{-3/2}$ according to Eq. (16). The fixed point described by Eq. (13) can be reached only below the crossover energy scale, $\mu \sim \Lambda e^{-\epsilon^{-3/2}}$, where Λ is a UV cut-off scale. This is illustrated in Fig. 2.5. The crossover energy scale goes to zero as ϵ becomes smaller, and the fixed point in

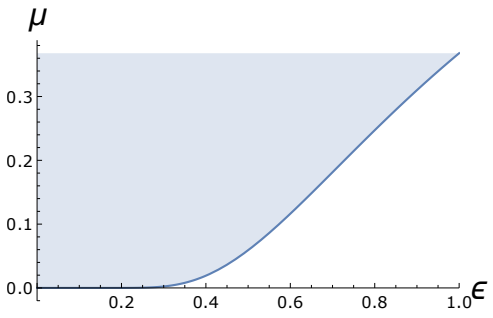

Figure 2.5: The crossover scale between the one-loop and M1L fixed points as a function of ϵ.

Eq. (13) is never reached at $\epsilon = 0$. A converse issue of non-commutativity arises in $2 + \epsilon'$ dimensions[57]. In order to capture the correct physics in two dimensions, one needs to take the $\epsilon' \to 0$ limit first before taking the low energy limit. If the other order of limits is taken, some logarithmic corrections are missed[57].

Although the two-loop diagram in Fig. 2.3 (a) is superficially $\mathcal{O}(\epsilon^2)$, it becomes $\mathcal{O}(\epsilon)$ at the fixed point because the IR singularity caused by the vanishingly small velocities enhances the magnitude of the diagram. Formally, a factor of g^2 coming from one additional loop is canceled by an IR enhancement of c^{-3} in Eq. (6), which makes the two-loop diagram as important as the

one-loop diagrams in the small ϵ limit. This is rather common in field theories of Fermi surfaces where the perturbative expansion is not organized by the number of loops[36, 38, 42, 54].

The breakdown of the naive loop expansion is analogous to the case of the ferromagnetic quantum critical point[60]. In the disordered ferromagnetic quantum critical metal, the perturbative expansion breaks down even near the upper critical dimension, as a dangerously irrelevant operator enters in the beta functions of other couplings in a singular manner[61, 62]. In our case, the velocities play the role of dangerously irrelevant couplings which spoil the naive loop expansion. Although they are marginally irrelevant, one cannot readily set the velocities to zero as quantum corrections are singular in the zero velocity limit. This leads to a subtle balance between the Yukawa coupling and the velocities, making the two-loop diagram as important as the one-loop diagrams. Then the natural question is the role of other higher-loop diagrams. In the following, we show that other higher-loop diagrams are suppressed and the ϵ-expansion is controlled, as is the case for the SDW critical metal with C_2 symmetry[54].

III Emergent small parameter

In this section, we show that the ϵ-expansion is controlled, by providing an upper bound for the magnitudes of general higher-loop diagrams at the M1L fixed point. Furthermore, we show that a large class of diagrams are further suppressed by w, which flows to zero in the low energy limit. Since $\kappa_i = 0$ at the M1L fixed point, only those diagrams without quartic vertices are considered. Among the diagrams made of only Yukawa vertices, we first focus on the diagrams without self-energy corrections. The diagrams without self-energy corrections scale as

$$I \sim \frac{g^{2L+E-2}}{v^{L_f} c^{L-L_f}}, \tag{18}$$

up to potential logarithmic corrections in v and c, where L is the total number of loops, L_f is the number of fermion loops, and E is the number of external lines. The derivation of Eq. (18), which closely follows Ref. [63], can be found in Appendix A III.

A diagram whose overall magnitude is given by Eq. (18) contributes to the counter term as

$$\begin{aligned} \mathcal{A}_1, \mathcal{A}_2, \mathcal{A}_3, \mathcal{A}_4, \mathcal{A}_6 &\sim \lambda^L \, w^{L-L_f}, \\ \mathcal{A}_5 &\sim \lambda^{L-1} \, w^{L-L_f-1} \, x, \end{aligned} \tag{19}$$

up to logarithmic corrections in v and c, where the relations, $g = \left(\frac{\lambda^3 w^3}{x}\right)^{\frac{1}{4}}$, $v = \left(\frac{\lambda w^3}{x}\right)^{\frac{1}{2}}$ and $c = \left(\frac{\lambda w}{x}\right)^{\frac{1}{2}}$ are used. $\mathcal{A}_5$ scales differently from the rest of the counter terms because quantum corrections to the spatial part of the boson kinetic term are enhanced by $\frac{1}{c^2}$. Since the classical action $c^2|\vec{q}|^2$ vanishes in the $c \to 0$ limit, the relative magnitude of quantum

corrections to the classical action is enhanced as $\mathcal{A}_5 \sim \frac{1}{c^2} I$. For example, the two-loop diagram in Fig. 2.3 is $\mathcal{A}_5 \sim \frac{g^4}{vc^3}$. On the other hand, $\mathcal{A}_2$ is not enhanced by $\frac{1}{v}$, even though the fermion kinetic term also loses its dependence on k_x (k_y) for $n = 1, 3$ ($n = 2, 4$) in the small v limit. The difference is attributed to the fact that the fermion self-energy takes the form of $\Sigma(k) \sim \frac{g^{2L}}{v^{L_f} c^{L-L_f}} \tilde{\Sigma}(k_0, vk_x, k_y)$ for $n = 1, 3$ and $\Sigma(k) \sim \frac{g^{2L}}{v^{L_f} c^{L-L_f}} \tilde{\Sigma}(k_0, k_x, vk_y)$ for $n = 2, 4$. Besides the overall factor of $\frac{g^{2L}}{v^{L_f} c^{L-L_f}}$ from Eq. (18), $\tilde{\Sigma}$ becomes independent of k_x (k_y) for $n = 1, 3$ ($n = 2, 4$) in the small v limit. This is because in all fermion self-energy diagrams the external momentum can be directed to flow through a series of fermion propagators of type $n = 1, 3$ ($n = 2, 4$) only, and the fermion propagators become independent of k_x (k_y) when $v = 0$. For example, the one-loop fermion self-energy with $L = 1, L_f = 0$ in Fig. 2.2 is at most $\Sigma \sim \frac{g^2}{c}(vk_x - k_y)$ for $n = 1$. Explicit calculation actually shows that the one-loop diagram is further suppressed by c for an unrelated reason[43].

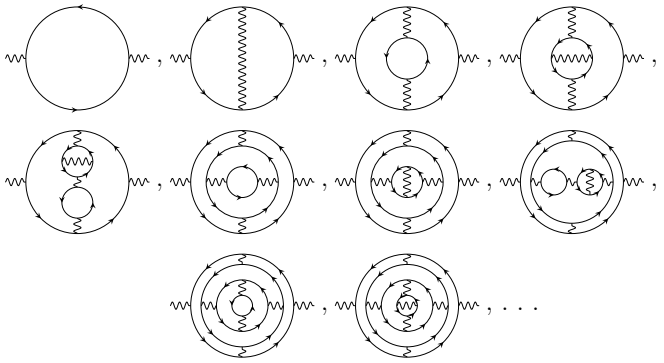

Figure 2.6: Some examples in the infinite series of diagrams that survive in the small w limit.

Now we consider the consequences of Eq. (19). We initially ignore the potential logarithmic corrections in v, c. First, higher-loop diagrams are systematically suppressed by $\lambda^* \sim \epsilon$ as the number of loops increases. However, there is an exception to the usual rule that L-loop diagrams are suppressed by ϵ^L. The quantum correction to the spatial part of the boson kinetic term is suppressed only by ϵ^{L-1}, due to the enhancement by $1/c^2$. Although Eq. (19) suggests that the one-loop contribution to $\mathcal{A}_5$ scales as $\lambda^0 w^{-1} x$, its contribution to $\mathcal{A}_5$ is actually zero because Fig. 2.2 (a) is independent of momentum. Since all self-energy corrections are at most $O(\epsilon)$, diagrams with self-energy insertions are further suppressed by ϵ. This implies that the ϵ-expansion is controlled, and the M1L includes all quantum corrections to the linear order in ϵ.

Second, a large class of higher-loop diagrams are further suppressed by w which flows to zero in the low energy limit. Unlike ϵ, which is fixed at a given dimension, w flows to zero dynamically in the low energy limit. The suppression by w is controlled by the number of non-fermion loops. The only diagram with $L - L_f = 0$ is the one-loop boson self-energy in Fig. 2.2 (a). Since $\mathcal{A}_5$ from Fig. 2.2 (a) vanishes, the leading order contribution to $\mathcal{A}_5$ comes from the two-loop boson self-energy in Fig. 2.3 at $\mathcal{O}(w^0)$. Among the diagrams without self-energy insertions, only Fig. 2.2 (a) and Fig. 2.3 survive in the small w limit. When those self-energy

corrections are included inside a diagram, the diagram with dressed boson propagators is not further suppressed by w (although they are suppressed by ϵ). Other self-energy corrections, including all fermion self-energies, are negligible because they are suppressed by w. Therefore, the complete set of diagrams which survive in the small w limit are generated by dressing the boson propagator in Fig. 2.3 by the self-energy in Fig. 2.2 (a) and Fig. 2.3. This generates a series of diagrams, some of which are shown in Fig. 2.6.

Now we turn our attention to the sub-leading corrections that are potentially logarithmically divergent in v and c in Eq. (19). Diagrams suppressed by at least one power of w still vanish in the small w limit even in the presence of logarithmic divergences in v or c. However, the effect of the logarithms on the diagrams in Fig. 2.6 (which are $\mathcal{O}(w^0)$) cannot be ignored, and this can in principle jeopardize the control of the ϵ-expansion. In Appendix A IV, we demonstrate that the ϵ-expansion is still controlled, by showing that all logarithmic corrections that arise at higher orders in ϵ can be absorbed into $\tilde{x} = x/F(c, v)$, where $F(c, v)$ is defined such that $\tilde{x}$ flows to x^* in the low energy limit. Once physical observables are expressed in terms of the new parameter $\tilde{x}$, they have a well defined expansion in ϵ. At least for small ϵ, the theory is free of perturbative instabilities toward other competing orders [38, 64–68], and it represents a stable non-Fermi liquid state[42, 54, 69].

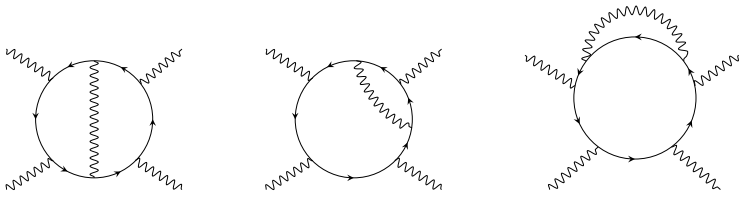

Figure 2.7: Quantum corrections that renormalize the quartic vertices in the small w, ϵ limit.

Although $\kappa_i = 0$ at the M1L fixed point, the quartic vertices are generated from the Yukawa vertices. It happens that the one-loop diagram in Fig. 2.2(d) vanishes, and the leading contributions that source the quartic vertices are shown in Fig. 2.7. Once these diagrams are included, the beta functions for κ_i are modified as

$$\frac{d\kappa_i}{dl} = -\epsilon\,\kappa_i + A_i \lambda^{\frac{5}{2}} w^{\frac{3}{2}} x^{\frac{1}{2}}, \tag{20}$$

where the A_i's are functions that diverge at most logarithmically in w in the small w limit. As a result, the quartic couplings flow to zero as $\kappa_i \sim w^{\frac{3}{2}}$ up to logarithms of w as w flows to zero.

The small parameter w that emerges in the low energy limit suppresses all higher-loop diagrams except for the specific set of diagrams shown in Fig. 2.6. It turns out that w flows to zero in the low energy limit in any dimensions, $2 \leq d < 3$[56, 57]. This allows one to extract the exact critical exponents by non-perturbatively summing the infinite series of diagrams through a self-consistent equation.

IV Physical Properties

Now, we examine the scaling form of the Green's functions. The dynamical critical exponent and the anomalous scaling dimensions at the fixed point are given by

$$z = 1, \quad \eta_\psi = 0, \quad \eta_\phi = \frac{\epsilon}{2}. \tag{21}$$

These critical exponents do not receive higher-order corrections in ϵ in the small w limit, as is shown in Appendix A IV. Indeed, w flows to zero in the low energy limit, and the critical exponents in Eq. (21) are exact in any $0 < \epsilon \leq 1$[57, 63]. At intermediate energy scales, the physical Green's functions receive corrections generated from irrelevant parameters of the theory. The least irrelevant parameter that decays at the slowest rate is w, which decays as $l^{-2/3}$ in the logarithmic scale l. This sub-logarithmic flow introduces super-logarithmic corrections in the Green's functions. The fermion Green's function for the $n = 1$ patch is given by

$$G_1(\mathbf{K}, \vec{k}) = \frac{1}{iF_\psi(|\mathbf{K}|)} \times \frac{1}{F_z(|\mathbf{K}|)\mathbf{\Gamma}\cdot\mathbf{K} + \gamma_{d-1}\left[\frac{\pi N_c N_f}{4\epsilon(N_c^2-1)}\frac{k_x}{\log(1/|\mathbf{K}|)} + k_y\right]} \tag{22}$$

in the limit of small frequency $|\mathbf{K}|$ and fixed $e^{\mathfrak{I}_z(l)}\vec{k} \sim 1$, where $\mathfrak{I}_z(l) = l - \frac{3(N_c^2-1)^{\frac{1}{3}}}{2^{\frac{14}{3}}(h_5^*)^{\frac{1}{3}}} l^{\frac{1}{3}}$ and $l = \log(1/|\mathbf{K}|)$. The universal functions $F_z(|\mathbf{K}|)$ and $F_\psi(|\mathbf{K}|)$,

$$F_z(|\mathbf{K}|) = \exp\left(\frac{3(N_c^2-1)^{\frac{1}{3}}}{2^{\frac{14}{3}}(h_5^*)^{\frac{1}{3}}}\left(\log\frac{1}{|\mathbf{K}|}\right)^{\frac{1}{3}}\right), \tag{23}$$

$$F_\psi(|\mathbf{K}|) = \sqrt{\log\frac{1}{|\mathbf{K}|}}, \tag{24}$$

contain the contributions from the deviations of the dynamical critical exponent and the anomalous scaling dimension of the fermion, respectively, from their fixed point values in Eq. (21). Due to the super-logarithmic correction, the quasiparticle peak is destroyed. All other Green's functions are determined by this one through the C_4 symmetry of the theory.

The scaling form of the spin-spin correlation function is given by

$$D(\mathbf{Q}, \vec{q}) = \frac{1}{|\mathbf{Q}|^{2-\epsilon}F_z(|\mathbf{Q}|)^2 F_\phi(|\mathbf{Q}|)} \times \mathfrak{D}\left(\frac{\vec{q}}{F_z(|\mathbf{Q}|)|\mathbf{Q}|}; \frac{N_c N_f}{2^{\frac{11}{3}}(h_5^*)^{\frac{1}{3}}(N_c^2-1)^{\frac{2}{3}}}\frac{1}{\epsilon}\frac{1}{\log(1/|\mathbf{Q}|)^{\frac{2}{3}}}\right), \tag{25}$$

in the limit of small frequency $|\mathbf{Q}|$ and fixed $e^{\mathfrak{I}_z(\log(1/|\mathbf{Q}|))}\vec{q} \sim 1$. $\mathfrak{D}$ is a universal function, and

$$F_\phi(|\mathbf{Q}|) = \exp\left(-\frac{3(N_c^2-3)}{2^{\frac{11}{3}}(h_5^*)^{\frac{1}{3}}(N_c^2-1)^{\frac{2}{3}}}\left(\log\frac{1}{|\mathbf{K}|}\right)^{\frac{1}{3}}\right) \tag{26}$$

is the universal function which captures the contribution from the deviation of the anomalous scaling dimension of the boson field from its fixed point value in Eq. (21). Unlike the fermion Green's function, the boson has a non-trivial anomalous dimension.

V Physical picture

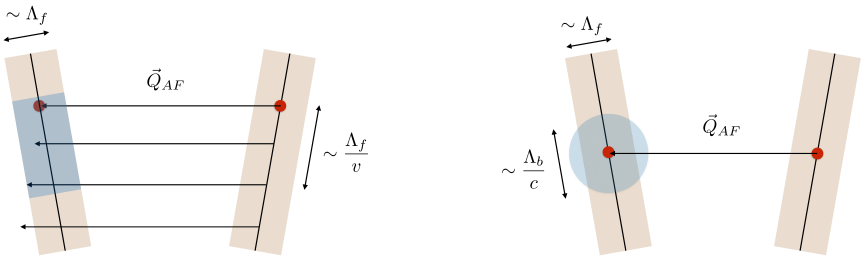

(a) (b)

Figure 2.8: The tilted lines represent patches of Fermi surface connected by the AF ordering vector, where the red dots denote hot spots. The Fermi surfaces are not parallel because of non-zero v. (a) Particle-hole excitations of momentum $\vec{Q}_{AF}$ can stay within the low-energy states of energy $E < \Lambda_f$ as far as their momenta are within the range of Λ_f/v from the hot spots. Therefore the phase space available for Landau damping of the collective mode scales as $1/v$ in the small v limit. (b) The shaded region denotes the phase space available for a fermion when scattered by a collective mode of energy less than Λ_b. Since the energy of the boson with momentum $\vec{q}$ scales as $c|\vec{q}|$, a boson with energy less than Λ_b can transfer momentum up to Λ_b/c to a fermion. Therefore, the phase space grows as $1/c$ in the small c limit.

Finally, we provide a simple physical picture for why $w = v/c$ emerges as a control parameter. The most important factor is the Landau damping which describes the decay of the collective mode into the particle-hole continuum. As the Fermi surface becomes locally nested near the hot spots in the small v limit, the phase space for the particle-hole excitations that a collective mode can decay into increases as $1/v$. A single boson with a fixed momentum can decay into low-energy particle-hole pairs that lie anywhere along the nested Fermi surface of length Λ_f/v, where Λ_f is an energy cut-off for the fermionic excitations. This is illustrated in Fig. 2.8(a). This results in a large screening, which renormalizes the Yukawa vertex to $g^2 \sim \epsilon v$. As the Fermi surface gets nested, g flows to zero.

The dispersionless particle-hole excitations near the hot spots renormalize the velocity of

the collective mode to zero as well, through the mixing between the collective mode and the particle-hole excitations. As the fluctuations of the collective mode become soft, quantum fluctuations are enhanced at low energies. On the other hand, the enhanced quantum fluctuations speeds up the velocity of the collective mode through Fig. 2.3, and a balance is formed such that $c^3 \sim g^2 \sim \epsilon v$ to the leading order in ϵ. As a result, the boson velocity c flows to zero at a much slower rate than v.

Now let us consider the feedback of the collective mode on the propagation of fermions, by examining the process where a fermion is scattered by a collecitve mode. With the initial momentum fixed, the fermion does not have access to the entire Fermi surface. Instead it can only scatter into a region allowed by the maximum momentum carried by a collective mode. The available phase space for the scattering scales as Λ_b/c, where Λ_b is the energy cut-off of the collective mode. This is illustrated in Fig. 2.8(b). Therefore, the scattering of fermions is controlled by $g^2/c \sim \epsilon\, v/c$, where $g^2 \sim \epsilon v$ is used. As v/c flows to zero in the low energy limit, the scattering of fermions by collective modes becomes negligible. This explains why fermions are largely intact in the small w limit, and w emerges as a control parameter.

VI Conclusion

We extended the earlier one-loop analysis of the antiferromagnetic quantum critical metal based on the dimensional regularization scheme which tunes the number of co-dimensions of the one-dimensional Fermi surface. We show that the IR singularities caused by the emergent quasi-locality rearrange the perturbative series such that a two-loop graph becomes as important as the one-loop graphs in the small ϵ limit. With the inclusion of this two-loop effect, higher-loop diagrams are systematically suppressed, and the ϵ-expansion is controlled. Furthermore, a ratio between velocities dynamically flows to zero, which has been confirmed in the non-perturbative solution in $2 \leq d < 3$[56, 57]. The ϵ-expansion provides an independent justification for the ansatz used in the non-perturbative solution.

Chapter 3

Exact Critical Exponents for the Antiferromagnetic Quantum Critical Metal in Two Dimensions

In this chapter, we present a non-perturbative study of the theory in Eq. (1). We solve the theory in $d = 2$ by assuming that the expressions for the critical exponents obtained from the modified-one-loop computation near three dimensions extend to $d = 2$. This amounts to assuming that the critical exponents do not receive quantum corrections beyond the linear order in ϵ. Although this is a highly non-trivial assumption, we show that this is indeed the case, due to the fact that v/c flows to zero at low energies and a large class of diagrams are suppressed in the small v/c limit. Although there are additional logarithmic corrections that arise at $d = 2$, these corrections do not modify the critical exponents. The expansion in v/c is not the same as the perturbative expansion near the Gaussian fixed point. To the leading order in v/c, an infinite series of diagrams has to be included non-perturbatively, as will be shown later.

Until now, the two-dimensional theory had been deemed intractable. However, the non-perturbative solution allows us to solve this strongly interacting theory reliably. We predict the exact critical exponents that govern the scaling of dynamical and thermodynamic observables. This provides the first exact predictions for the AF QCP in layered materials. Besides its experimental relevance, the exact low-energy solution of this theory is also important from a theoretical point of view, in that it may open up a route to tackle other strongly coupled quantum field theories non-perturbatively. There are many strongly interacting theories in condensed matter and other areas of physics, but exact solutions are few and far between. Having as many examples of exact solutions as possible is important for gaining intuition into non-perturbative physics. So far, most examples come from theories in $1 + 1$ dimensions, where the conformal symmetry at the fixed point highly restricts the landscape of available solutions, or from supersymmetric field theories in higher dimensions[70]. In non-relativistic systems, the symmetries of the fixed point are usually not large enough to be useful in the same way. That is why it is important to search for new routes to gain non-perturbative access to strongly interacting theories.

I Low-energy theory and interaction-driven scaling

We start by writing the action in Eq. (1) in terms of the two-component spinors $\Psi_{n,\sigma}$,

$$\begin{aligned}\mathcal{S} \quad &= \textstyle\sum_{n=1}^{4}\sum_{\sigma=\uparrow,\downarrow}\int dk\ \bar{\Psi}_{n,\sigma}(k)\left[i\gamma_0 k_0 + i\gamma_1\varepsilon_n(\vec{k})\right]\Psi_{n,\sigma}(k)\\ &\quad +\tfrac{1}{4}\textstyle\int dq\ \left[q_0^2 + c_0^2|\vec{q}|^2\right]\mathrm{Tr}\left[\Phi(-q)\ \Phi(q)\right]\\ &\quad +ig\textstyle\sum_{n=1}^{4}\sum_{\sigma,\sigma'}\int dkdq\ \left[\bar{\Psi}_{\bar{n},\sigma}(k+q)\Phi_{\sigma,\sigma'}(q)\gamma_1\Psi_{n,\sigma'}(k)\right]\\ &\quad +u\textstyle\int dk_1dk_2dq\ \mathrm{Tr}\left[\Phi(k_1+q)\Phi(k_2-q)\right]\mathrm{Tr}\left[\Phi(-k_1)\Phi(-k_2)\right].\end{aligned} \tag{27}$$

This is done to make contact with the general theory in Eq. (2). However, here we do not generalize to arbitrary N_f and N_c, but keep the physical values of $N_f = 1$, $N_c = 2$. In two dimensions, the gamma matrices are chosen to be $\gamma_0 = \sigma_y, \gamma_1 = \sigma_x$. Here, $\Phi(q) =$

$\sum_{a=1}^{3} \phi^a(q)\tau^a$ is a 2×2 matrix boson field and the τ^a's are the generators of the $SU(2)$ spin.

Two dimensions is too far from the upper critical dimensional of three for the perturbative expansion in ϵ to be reliable in general. However, the emergent expansion parameter $w = v/c$ at the novel fixed point gives us hope that this is not entirely the case. We therefore assume that the critical exponents found in Chapter 1 hold all the way down to $\epsilon = 1$. At the fixed point in general dimensions, the dynamical critical exponent and scaling dimensions of the fields are given by

$$z = 1, \quad [\psi(k)] = -\frac{5-\epsilon}{2}, \quad [\phi(k)] = -(3-\epsilon). \tag{28}$$

By setting $\epsilon = 1$, we arrive at our ansatz for the two-dimensional theory,

$$\begin{aligned} &[k_0] = [k_x] = [k_y] = 1, \\ &[\psi(k)] = [\phi(k)] = -2. \end{aligned} \tag{29}$$

Under Eq. (29), the electron keeps the classical scaling dimension, while the boson has an $O(1)$ anomalous dimension compared to the Gaussian scaling.

The scaling of Eq. (29) amounts to an interaction-driven scaling[69], where the fermion kinetic term and the Yukawa interaction are chosen to be marginal at the expense of treating the entire boson kinetic term as irrelevant, which determines all scaling dimensions uniquely. We could have arrived at such a choice without using the intuition of Eq. (28), since we know the Yukawa interaction plays a dominant role, and the dynamics of the boson is dominated by particle-hole excitations near the Fermi surface in the low-energy limit, unless the number of bosons per fermion is infinite[71]. At this point, Eq. (29) is merely an ansatz. The real test is to show that these exponents are actually exact, which is the main goal of this paper.

Under Eq. (29), the entire boson kinetic term and the quartic coupling are irrelevant. The minimal action which includes only marginal terms is written as

$$\begin{aligned} \mathcal{S} \quad &= \sum_{n=1}^{4} \sum_{\sigma=\uparrow,\downarrow} \int dk\ \bar{\Psi}_{n,\sigma}(k) \left[i\gamma_0 k_0 + i\gamma_1 \varepsilon_n(\vec{k}) \right] \Psi_{n,\sigma}(k) \\ &+ i\sqrt{\tfrac{\pi v}{2}} \sum_{n=1}^{4} \sum_{\sigma,\sigma'} \int dk dq \left[\bar{\Psi}_{\bar{n},\sigma}(k+q) \Phi_{\sigma,\sigma'}(q) \gamma_1 \Psi_{n,\sigma'}(k) \right]. \end{aligned} \tag{30}$$

Here, the fermion-boson coupling is set to be proportional to $\sqrt{v}$ by rescaling the boson field. The Yukawa coupling is replaced with $\sqrt{v}$ because the interaction is screened such that g^2 becomes $O(v)$ in the low-energy limit[43]. Although g and v can be independently tuned in the microscopic theory, they rapidly flow to a universal line defined by $g^2 \sim v$ at low energies[72]. Eq. (30) should be understood as the minimal theory that captures the universal physics at low energies, where the dynamics of the collective mode is dominated by particle-hole excitations rather than the bare kinetic term, and v is the only dimensionless parameter. In the small v limit, g also vanishes because a nested Fermi surface provides a large phase space for low-energy

particle-hole excitations with momentum $\vec{Q}_{AF}$ that screen the interaction. Even when g, v are small, this is a strongly interacting theory because $g^2/v \sim 1$ is the expansion parameter in the conventional perturbative series. With $g^2/v \sim 1$, the leading boson kinetic term which is generated from particle-hole excitations is $O(1)$, as will be seen later.

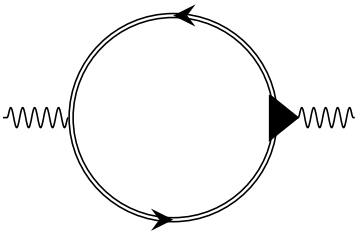

Figure 3.1: The exact boson self-energy. The double line is the fully dressed fermion propagator. The triangle represents the fully dressed vertex.

II Self-consistent solution

Naively the theory is singular due to the absence of a boson kinetic term. However, particle-hole excitations generate a self-energy which provides non-trivial dynamics for the collective mode. The Schwinger-Dyson equation for the boson propagator (shown in Figure 3.1) reads

$$D(q)^{-1} = m_{CT} - \pi v \sum_n \int dk \, \mathrm{Tr}\left[\gamma_1 G_{\bar{n}}(k+q)\Gamma(k,q)G_n(k)\right]. \tag{31}$$

Here $D(k)$, $G(k)$ and $\Gamma(k,q)$ represent the fully dressed propagators of the boson and the fermion, and the vertex function, respectively. m_{CT} is a mass counter term that is added to tune the renormalized mass to zero. The trace in Eq. (31) is over the spinor indices. It is difficult to solve the full self-consistent equation because $G(k)$ and $\Gamma(k,q)$ depend on the unknown $D(q)$. One may use v as a small parameter to solve the equation. The one-loop analysis shows that v flows to zero due to emergent nesting of the Fermi surface near the hot spots[38, 51, 52, 73]. This has been also confirmed in the ϵ expansion based on the dimensional regularization scheme[43, 72]. Of course, the perturbative result valid close to three dimensions does not necessarily extend to two dimensions. Nonetheless, we show that this is indeed the case. Here we proceed with the following steps:

1. we solve the Schwinger-Dyson equation for the boson propagator in the small v limit,
2. we show that v flows to zero at low energies by using the boson propagator obtained under the assumption of $v \ll 1$.

We emphasize that the expansion in v is different from the conventional perturbative expansion in coupling. Rather it involves a non-perturbative summation over an infinite series of diagrams

as will be shown in the following.

We discuss step 1) first. In the small v limit, the solution to the Schwinger-Dyson equation is

$$D(q)^{-1} = |q_0| + c(v)\Big[|q_x| + |q_y|\Big], \tag{32}$$

where the 'velocity' of the strongly damped collective mode is given by

$$c(v) = \frac{1}{4}\sqrt{v\log(1/v)}. \tag{33}$$

Solving the Schwinger-Dyson equation consists of two parts. First, we assume Eq. (32) with a hierarchy of the velocities $v \ll c(v) \ll 1$ as an ansatz to show that only the one-loop vertex correction is important in Eq. (31). Then we show that Eqs. (32) and (33) actually satisfy Eq. (31) with the one-loop dressed vertex.

We begin by estimating the magnitude of general diagrams, assuming that the fully dressed boson propagator is given by Eq. (32) with Eq. (33) in the small v limit. In general, the integrations over loop momenta diverge in the small v limit as fermions and bosons lose their dispersion in some directions. In each fermion loop, the component of the internal momentum tangential to the Fermi surface is unbounded in the small v limit due to nesting. For a small but nonzero v, the divergence is cut off at a scale proportional to $1/v$, and each fermion loop contributes a factor of $1/v$. Each of the remaining loops necessarily has at least one boson propagator. For those loops, the momentum along the Fermi surface is cut off by the energy of the boson which provides a lower cut-off momentum proportional to $1/c$ for $c \gg v$. Therefore, the magnitude of a general L-loop diagram with V vertices, L_f fermion loops and E external legs is at most

$$I \sim v^{V/2-L_f} c^{-(L-L_f)} \sim v^{\frac{1}{2}(E-2)} \left(\frac{v}{c}\right)^{(L-L_f)}, \tag{34}$$

where $V = 2L + E - 2$ is used. Higher-loop diagrams are systematically suppressed with increasing $(L - L_f)$ provided $v \ll c$. This is analogous to the situation where a ratio between velocities is used as a control parameter in a Dirac semi-metal[55] [1]. If Eq. (33) holds, the upper bound becomes $I \sim v^{\frac{1}{2}(E-2)+\frac{1}{2}(L-L_f)}$ up to a logarithmic correction. It is noted that Eq. (34) is only an upper bound because some loop integrals which involve un-nested fermions remain finite even in the small v limit. Some diagrams can also be smaller than the upper bound because their dependences on external momentum are suppressed in the small v and c limit. A systematic proof of Eq. (34) is available in Appendix B I.

For $v \ll c$, the leading order contribution for the boson self-energy ($E = 2$) is generated

[1] There also has been an attempt to use a different ratio of velocities as a control parameter in non-Fermi liquids with critical bosons centered at zero momentum [A. Fitzpatrick, S. Kachru, J. Kaplan, S. A. Kivelson, S. Raghu, arXiv:1402.5413].

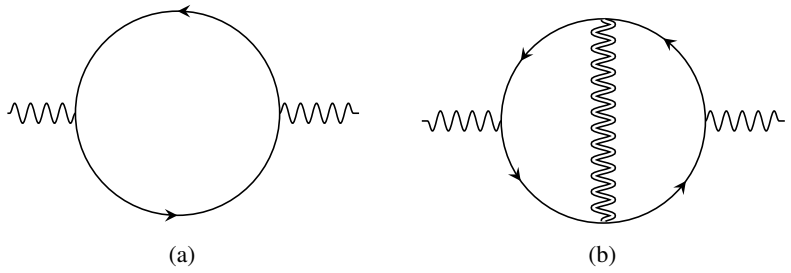

Figure 3.2: The leading order diagrams for the boson self-energy in the small v limit. Solid lines are the bare fermion propagators. The wiggly double line represents the boson propagator consistently dressed with the self-energy in (a) and (b). The dressed boson propagator includes an infinite series of nested self-energies with a fractal structure.

from Figure 3.2(a), which is the only diagram that satisfies $L = L_f$. All other diagrams are sub-leading in v. However, this is not enough because the one-loop diagram gives $D(q)^{-1} = |q_0|$, which is independent of spatial momentum. One has to include the next order diagram (Figure 3.2(b)) which generates a dispersion. Therefore, Eq. (31) is reduced to

$$D(q)^{-1} = m'_{CT} + |q_0| \\ -\frac{\pi^2 v^2}{2} \sum_n \int dp\, dk\, \mathrm{Tr}\left[\gamma_1 G_n^{(0)}(k+p)\gamma_1 G_{\bar{n}}^{(0)}(p+q+k)\gamma_1 G_n^{(0)}(q+k)\gamma_1 G_{\bar{n}}^{(0)}(k)\right] D(p).$$

Here m'_{CT} is a two-loop mass counter term. We can use the free fermion propagator $G_n^{(0)}$ because the fermion self-energy correction is sub-leading in v. An explicit calculation of Eq. (35) confirms that the self-consistent boson propagator takes the form of Eq. (32). The boson velocity satisfies the self-consistent equation $c = \frac{v}{8c}\log(c/v)$, which is solved by Eq. (33) in the small v limit. c is much larger than v in the small v limit because of the enhancement factor $1/c$ in the two-loop diagram : the collective mode speeds up itself through enhanced quantum fluctuations if it gets too slow. We note that the anti-screening nature of the vertex correction associated with the non-Abelian $SU(2)$ vertex, $\sum_{a=1}^{3} \tau^a \tau^b \tau^a = -\tau^b$, is crucial to generate the right sign for the boson kinetic term[54]. This does not hold for Ising-like or XY-like spin fluctuations[74]. The details on the computation of Eq. (35) are available in Appendix B II. It is noted that Eq. (35) constitutes a non-perturbative sum over an infinite series of diagrams beyond the random phase approximation (RPA). The dynamics of the boson generated from the fermionic sector dominates at low energies. This justifies the choice to drop the bare kinetic term in Eq. (30).

So far, we have assumed that v is small to obtain the self-consistent dynamics of the AF collective mode. Now we turn to step 2) and show that v indeed flows to zero in the low-energy limit. According to Eq. (34), the leading quantum corrections to the local action in Eq. (30) are the one-loop diagrams for the fermion self-energy and the vertex function. However, the momentum-dependent one-loop fermion self-energy happens to be smaller than what is expected from Eq. (34) by an additional power of $c \sim \sqrt{v}$. This is because the dependence on the external

momentum is suppressed in the small c limit for the one-loop self-energy. As a result, we include the fermion self-energy up to two loops in order to capture all quantum corrections to the leading order in v. All other higher-loop diagrams are negligible in the small v limit. The self-energy and vertex correction are logarithmically divergent in a UV cut-off. Counter terms are added such that the renormalized quantum effective action becomes independent of the UV cut-off. The full details on the computation of the counter terms and the beta function can be found in Appendix B III. The bare action that includes the counter terms is obtained to be

$$\begin{aligned}\mathcal{S}_B \quad &= \sum_{n=1}^{4}\sum_{\sigma=\uparrow,\downarrow}\int d^3k\ \bar{\Psi}_{n,\sigma}(k)\Big[iZ_1\gamma_0 k_0 + i\gamma_1\varepsilon_n^B(\vec{k})\Big]\Psi_{n,\sigma}(k)\\ &+iZ_6\sqrt{\tfrac{\pi v}{2}}\sum_{n=1}^{4}\sum_{\sigma,\sigma'}\int d^3k d^3q\ \Big[\bar{\Psi}_{\bar{n},\sigma}(k+q)\Phi_{\sigma,\sigma'}(q)\gamma_1\Psi_{n,\sigma'}(k)\Big],\end{aligned} \tag{35}$$

where $\varepsilon_1^B(\vec{k}) = Z_2 v k_x + Z_3 k_y$, $\varepsilon_2^B(\vec{k}) = -Z_3 k_x + Z_2 v k_y$, $\varepsilon_3^B(\vec{k}) = Z_2 v k_x - Z_3 k_y$ and $\varepsilon_4^B(\vec{k}) = Z_3 k_x + Z_2 v k_y$ with $Z_1 = 1 - \frac{3}{4\pi}\frac{v}{c(v)}\log\left(\frac{\Lambda}{\mu}\right)$, $Z_2 = 1 + \frac{15}{4\pi^2}v\log\left(\frac{1}{c(v)}\right)\log\left(\frac{\Lambda}{\mu}\right)$, $Z_3 = 1 - \frac{9}{4\pi^2}v\log\left(\frac{1}{c(v)}\right)\log\left(\frac{\Lambda}{\mu}\right)$ and $Z_6 = 1 - \frac{1}{4\pi}\frac{v}{c(v)}\log\left(\frac{c(v)}{v}\right)\log\left(\frac{\Lambda}{\mu}\right)$. Here Λ is a UV cut-off above which non-linear terms in the fermionic dispersion become important. μ is the scale at which the physical propagators and vertex function are expressed in terms of v through the renormalization conditions, $\frac{-i}{2}\frac{\partial}{\partial k_0}\mathrm{Tr}\left[\gamma_0 G_1(k)^{-1}\right]\Big|_{k=(\mu,0,0)} = 1 + F_1(v)$, $\frac{-i}{2}\frac{\partial}{\partial k_x}\mathrm{Tr}\left[\gamma_1 G_1(k)^{-1}\right]\Big|_{k=(0,\mu,0)} = v\,(1+F_2(v))$, $\frac{-i}{2}\frac{\partial}{\partial k_y}\mathrm{Tr}\left[\gamma_1 G_1(k)^{-1}\right]\Big|_{k=(0,0,\mu)} = 1+F_3(v)$, $\frac{1}{2}\mathrm{Tr}\left[\gamma_1\Gamma(k,q)\right]|_{q=0,k=(\mu,0,0)} = 1 + F_4(v)$, where the $F_i(v)$'s are UV-finite functions of v, which vanish in the small v limit. The specific form of $F_i(v)$ is unimportant, and they can be changed by adding finite counter terms in Z_i. $G_n(k)$ with $n = 2,3,4$ are fixed from $G_1(k)$ by the four-fold rotational symmetry. The bare and renormalized variables are related to each other through $k_{B,x} = k_x$, $k_{B,y} = k_y$, $k_{B,0} = \frac{Z_1}{Z_3}k_0$, $v_B = \frac{Z_2}{Z_3}v$, $\Psi_B(k_B) = \frac{Z_3}{Z_1^{\frac{1}{2}}}\Psi(k)$, $\Phi_B(k_B) = \frac{Z_3^{\frac{1}{2}}Z_6}{Z_1 Z_2^{\frac{1}{2}}}\Phi(k)$. By requiring that the bare quantities are independent of μ, we obtain the beta function $\beta_v \equiv \frac{dv}{d\log\mu}$, which dictates the dependence of the renormalized velocity on the scale,

$$\beta_v = \frac{6}{\pi^2}v^2\log\left(\frac{1}{c(v)}\right). \tag{36}$$

If v is initially small, Eq. (36) is reliable. It predicts that v becomes even smaller and flows to zero as

$$v = \frac{\pi^2}{3}\left(\log\frac{1}{\mu}\ \log\log\frac{1}{\mu}\right)^{-1} \tag{37}$$

in the small μ limit. The way v flows to zero in the low-energy limit does not depend on the initial value of v. This completes the cycle of self-consistency. Eq. (32) obtained in the small v limit becomes asymptotically exact in the low-energy limit within a nonzero basin of attraction

in the space of v whose fixed point is $v = 0$. The dynamical critical exponent and the anomalous dimensions are given by

$$\begin{aligned} z &= 1 + \frac{3}{4\pi}\frac{v}{c(v)}, \\ \eta_\phi &= \frac{1}{4\pi}\frac{v}{c(v)} \log\left(\frac{c(v)}{v}\right), \\ \eta_\psi &= -\frac{3}{8\pi}\frac{v}{c(v)} \end{aligned} \tag{38}$$

to the leading order in v. Here z sets the dimension of frequency relative to momentum. η_ϕ, η_ψ are the corrections to the interaction-driven tree-level scaling dimensions of the boson and fermion, respectively. The critical exponents are controlled by $w \equiv v/c(v)$, which flows to zero as $w = \frac{4\pi}{\sqrt{3}}\left(\log^{1/2}\frac{1}{\mu}\,\log\log\frac{1}{\mu}\right)^{-1}$ in the low-energy limit. This confirms that the scaling dimensions in Eq. (29) become asymptotically exact in the low-energy limit.

III Comparison of fixed points in $d = 2$ and $d = 3 - \epsilon$.

Here, we compare the structure of the fixed points found in this chapter and Chapter 2. The first key difference is that the result in $d = 2$ is non-perturbative. The second is in the relationship between c and v. In the case of $d = 3 - \epsilon$, it is given by $c \sim \epsilon^{1/3} v^{1/3}$, while in $d = 2$ we have $c \sim v^{1/2}$ up to logarithms of v. The difference in powers of v nearly suggests a general relationship $c \sim v^{1/d}$ up to logarithms, which indeed happens to be correct, as shown in Ref. [57]. The difference between $c \sim v^{1/3}$ and $c \sim v^{1/d} \sim v^{1/(3-\epsilon)}$ is attributed to the fact that in the ϵ expansion we only compute the relationship between c and v to the leading order in ϵ. This is described in more detail in Appendix A IV.

The other key differences between the two fixed points is the presence of logarithms of v and c in several physical observables in two dimensions. In particular, $c \sim v^{1/2}\sqrt{\log(1/v)}$, $\beta_v \sim v^2 \log(1/c(v))$, and $\eta_\phi \sim (v/c(v)) \log(c(v)/v)$, while in $d = 3 - \epsilon$ we have $\beta_v \sim v^2$ and $\eta_\phi \sim v/c$. These logarithmic corrections arise from the fact that $d = 2$ corresponds to a critical dimension in the limit that the Fermi surface is nested perfectly. In fact, these logarithms are the reason for the non-commutativity of the $d \to 2$ limit of the general d theory and the low energy limit [57].

IV Physical observables

Although $z - 1$, η_ψ and η_ϕ vanish in the low-energy limit, the sub-logarithmic decay of w with energy introduces corrections to the correlation functions at intermediate energy scales, which

are weaker than power-law but stronger than logarithmic corrections[59]. The retarded Green's function for the hot spot $1+$ takes the form,

$$G^R_{1+}(\omega,\vec{k}) = \frac{1}{F_\psi(\omega)\left[\omega\, F_z(\omega)\left(1+i\frac{\sqrt{3}\pi}{2}\frac{1}{\sqrt{\log\frac{1}{\omega}}\,\log\log\frac{1}{\omega}}\right)-\left(\frac{\pi^2}{3}\frac{k_x}{\log\frac{1}{\omega}\,\log\log\frac{1}{\omega}}+k_y\right)\right]} \tag{39}$$

in the small ω limit with the ratio $\frac{\vec{k}}{\omega\, F_z(\omega)}$ fixed. Here ω is the real frequency. $F_\psi(\omega)$ and $F_z(\omega)$ are functions which capture the contributions from η_ψ and z at intermediate energy scales. In the small ω limit, they are given by

$$F_\psi(\omega) = \left(\log\frac{1}{\omega}\right)^{\frac{3}{8}}, \quad F_z(\omega) = e^{2\sqrt{3}\frac{\left(\log\frac{1}{\omega}\right)^{1/2}}{\log\log\frac{1}{\omega}}}. \tag{40}$$

F_ψ and F_z only contribute as sub-leading corrections instead of modifying the exponents. However, they are still parts of the universal data that characterizes the critical point[38]. The additional logarithmic suppression in the dependence of k_x is due to v which flows to zero in the low-energy limit. The local shape of the Fermi surface is deformed as $k_y \sim \frac{k_x}{\log 1/k_x \log\log 1/k_x}$. The scaling form of the Green's function at different hot spots can be obtained by applying a sequence of 90 degree rotations and a space inversion to Eq. (39). The spectral function at the hot spots exhibits a power-law decay with the super-logarithmic correction as a function of frequency, $A(\omega) \sim \frac{1}{\omega F_z(\omega)F_\psi(\omega)(\log 1/\omega)^{1/2}\log\log 1/\omega}$.

The retarded spin-spin correlation function is given by

$$D^R(\omega,\vec{q}) = \frac{1}{F_\phi(\omega)\left(-i\omega F_z(\omega)+\frac{\pi}{4\sqrt{3}}\frac{|q_x|+|q_y|}{\left(\log\frac{1}{\omega}\right)^{1/2}}\right)} \tag{41}$$

in the small ω limit with fixed $\frac{\vec{q}}{\omega\, F_z(\omega)}$. $F_\phi(\omega)$ is another universal function that describes the super-logarithmic correction of η_ϕ,

$$F_\phi(\omega) = e^{\frac{2}{\sqrt{3}}\left(\log\frac{1}{\omega}\right)^{1/2}} \tag{42}$$

in the small ω limit. The factor of $\left(\log\frac{1}{\omega}\right)^{-1/2}$ in the momentum-dependent term is due to the boson velocity which flows to zero in the low-energy limit. Due to the strong Landau damping, the spin fluctuation is highly incoherent. It will be of great interest to test the scaling forms in Eqs. (39) and (41) from angle resolved photoemission spectroscopy and neutron scattering, respectively.

Now we turn to thermodynamic properties. The total free energy density can be written as $f = \frac{1}{2}\, Tr\left[\log D^{-1} - \Pi D\right] - Tr\left[\log G^{-1} - \Sigma G\right] + \Phi_2$, where Π, Σ are the self-energies of the boson and fermion respectively, and Φ_2 includes the two particle irreducible diagrams[75]. Here, the traces sum over three momenta and flavors. To the leading order in

v, $f_B = \frac{1}{2} Tr[\log D^{-1}]$ and $f_F = Tr[\log G^{(0)}]$ dominate. The dominant fermionic contribution comes from electrons away from the hot spots, $f_F \sim k_F T^2$, where k_F is the size of the Fermi surface. Naively, the bosonic contribution is expected to obey hyperscaling, because low-energy excitations are confined near the ordering vector. However, the free energy of the mode with momentum $\vec{p}$ is suppressed only algebraically as $\frac{T^2}{c(|p_x|+|p_y|)}$ at large momenta, in contrast to the exponential suppression for the free boson. The slow decay is due to the incoherent nature of the damped AF spin fluctuations, which have a significant spectral weight at low energies even at large momenta. As a result, $f_B \sim \int d\vec{p}\, \frac{T^2}{c(|p_x|+|p_y|)}$ is UV divergent. In the presence of the irrelevant local kinetic term, $\frac{c_0^2}{\tilde{\Lambda}}|\vec{p}|^2$ with $c_0 \sim 1$, the momentum integration is cut-off at $p_{max} \sim c\tilde{\Lambda}$, and f_B is proportional to $\tilde{\Lambda}$. From the scaling equation for f_B, $\left[zT\frac{\partial}{\partial T} + \tilde{\Lambda}\frac{\partial}{\partial \tilde{\Lambda}} - \beta_c \frac{\partial}{\partial c} - (2+z)\right] f_B(T, c, \tilde{\Lambda}) = 0$, we obtain $f_B \sim \tilde{\Lambda} T^2 F_z(T)$ in the low temperature limit. Remarkably, the bosonic contribution violates the hyperscaling, and it is larger than the fermionic contribution at low temperatures. In this case, the power-law violation of the hyperscaling is a consequence of the $z = 1$ scaling rather than the fact that v, c flow to zero[76]. The free energy gives rise to the specific heat which exhibits the T-linear behavior with the super-logarithmic correction,

$$c_V \sim \tilde{\Lambda} T F_z(T). \tag{43}$$

It is noted the deviation from the T-linear behavior is stronger than a simple logarithmic correction because $F_z(T)$ includes all powers of $\sqrt{\log \frac{1}{T}}$.

If the system is tuned away from the critical point, the boson acquires a mass term, $(\lambda - \lambda_c) \int dq \mathrm{Tr}\left[\Phi_q \Phi_{-q}\right]$, where λ is a tuning parameter. Due to the suppression of higher-loop diagrams, the scaling dimension of Φ^2 is -4 in momentum space. This implies that $\nu = 1$ in the low-energy limit, which is different from the mean-field exponent. The power-law scaling of the correlation length ξ with λ is modified by a super-logarithmic correction,

$$\xi \sim (\lambda - \lambda_c)^{-1} F_\xi(\lambda - \lambda_c), \tag{44}$$

where $F_\xi(\delta\lambda)$ is a universal function which embodies both the anomalous dimension of the boson and the vertex correction for the mass insertion. The former dominates close to the critical point, and $F_\xi(\delta\lambda)$ is the same as $F_\phi(\delta\lambda)$ to the leading order in small $\delta\lambda$. The derivation of the scaling forms of the physical observables is available in Appendix B IV.

The scaling forms of the physical observables discussed above are valid in the low energy limit. At high energies, there will be crossovers to different behaviors. The first crossover is set by the scale below which the dynamics of the collective mode is dominated by particle-hole excitations, and therefore Eqs. (41) and (43) hold. It is determined by the competition between Eq. (32) and the irrelevant local kinetic term for the collective mode in Eq. (27). For $\omega < \frac{c(v)^2}{c_0^2}\tilde{\Lambda}$, the terms linear in frequency and momentum dominate, where $\tilde{\Lambda}$ is an energy scale associated

with the irrelevant kinetic term. The details on the crossover are described in Appendix B. In the small v limit with $c_0 \sim 1$, this crossover scale for the boson goes as $E_b^* \sim c^2\tilde{\Lambda}$. The second crossover scale, denoted as E_f^*, is the one below which the behavior of the fermions at the hot spots deviates from the Fermi liquid one. For a small but non-zero v, the leading order self-energy correction to the fermion propagator is $\frac{3}{4\pi}\frac{v}{c(v)}\omega \log \frac{\Lambda}{\omega}$, which becomes larger than the bare term for $\omega < E_f^*$ with $E_f^* \sim \Lambda e^{-\frac{\pi}{3}\sqrt{\frac{\log 1/v}{v}}}$. Since v flows to zero only logarithmically, the flow of v can be ignored for the estimation of E_f^*. The value of v changes appreciably below $\Lambda e^{-\frac{1}{v \log 1/v}}$ as is shown in Appendix C.

At sufficiently low temperatures, the system eventually becomes unstable against pairing. An important question is how the crossover scales compare with the superconducting transition temperature T_c. The spin fluctuations renormalize pairing interactions between electrons near the hot spots, and enhance d-wave superconductivity[31, 65, 77–79]. In the small v limit, however, the renormalization of the pairing interaction by the AF spin fluctuations is suppressed by $\frac{v}{c(v)}$ for the same reason that the vertex correction is suppressed. Because the Yukawa coupling is marginal at the fixed point, it adds an additional logarithmic divergence to the usual logarithmic divergence caused by the BCS instability[32, 64, 80]. The pairing vertex is enhanced by $\alpha\frac{v}{c}\log\frac{\Lambda}{\omega}\log\frac{E_b^*}{\omega}$ with $\alpha \sim 1$ at frequency ω. The first logarithm is from the usual BCS mechanism. The second logarithm is from the gapless spin fluctuations, where $E_b^* \sim c^2\tilde{\Lambda}$ is the energy cut-off for the spin fluctuations in the small c limit as is shown in Appendix B. This gives $T_c \sim c\sqrt{\Lambda\tilde{\Lambda}}e^{-\sqrt{\frac{c}{\alpha\, v}}}$. Although T_c is enhanced by the critical spin fluctuations, it remains exponentially small in $\sqrt{\frac{c(v)}{v}} \sim v^{-\frac{1}{4}}$ in the small v limit. There is a hierarchy among the energy scales, $E_f^* \ll T_c \ll E_b^*$ in the small v limit. This suggests that the system undergoes a superconducting transition before the fermions at the hot spots lose coherence. On the one hand, this is similar to the nematic quantum critical point in two dimensions where the system is prone to develop a superconducting instability before the coherence of quasiparticles breaks down[81, 82]. On the other hand, even without superconductivity, the fermions are only weakly perturbed by the spin fluctuations in the present case. It is the collective mode that is heavily dressed by quantum effects. For the collective mode, there is a large window between T_c and E_b^* within which the universal scaling given by Eq. (32) is obeyed. The size of the energy window for the critical scaling is non-universal due to the slow flow of v, and it depends on the bare value of v. Our prediction is that there is a better chance to observe the $z = 1$ critical scaling above T_c, and the enhancement of T_c by AF spin fluctuations is rather minimal[83] in materials whose bare Fermi surfaces are closer to perfect nesting near the hot spots.

V Summary and Discussion

In summary, we solve the low-energy field theory that describes the antiferromagnetic quantum critical metal in two spatial dimensions. We predict the exact critical exponents which govern the universal scaling of physical observables at low temperatures. Finally, we comment on earlier theoretical approaches, and provide a comparison with experiments.

Our results are qualitatively different from earlier theoretical works [38, 51–53, 73, 84] which have invariably predicted the dynamical critical exponent z to be larger than one. In particular, if one uses the one-loop dressed propagators with $z = 2$, individual higher-loop corrections are logarithmically divergent at most. However, this does not imply that the higher-loop corrections are small. The logarithmic corrections remain important in two dimensions due to the strong coupling nature of the theory, and they can introduce $\mathcal{O}(1)$ anomalous dimensions.

Now we make an attempt to compare our predictions with experiments. Electron doped cuprates are probably the simplest examples of quasi-two-dimensional compounds that exhibit antiferromagnetic phase transitions in the presence of itinerant electrons, without having extra degrees of freedom such as local moments or extra bands. In the normal state of the optimally doped $Pr_{0.88}LaCe_{0.12}CuO_{4-\delta}$, inelastic neutron scattering shows an overdamped AF spin fluctuation peaked at (π, π) whose width in momentum space exhibits a weak growth with increasing energy[85]. The theoretical prediction from Eq. (41) is that the width of the incoherent peak scales linearly with energy upto a super-logarithmic correction in the low energy limit. However, it is hard to make a quantitative comparison due to the limited momentum resolution in the experiment. In $Nd_{2-x}Ce_xCuO_{4\pm\delta}$ (NCCO), inelastic neutron scattering suggests that the magnetic correlation length ξ scales inversely with temperature near the critical doping[45], as shown in Fig. 3.3(a). Furthermore, ξ measured at the pseudogap temperature diverges as

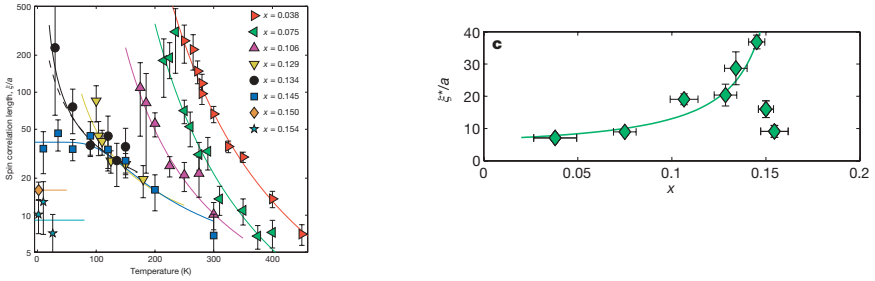

(a) (b)

Figure 3.3: The inelastic neutron scattering data from Ref. [45] on the magnetic correlation length ξ. (a) The temperature dependence of ξ at various doping concentrations x. The critical concentration is $x_c = 0.134$. The fit of the data at this doping corresponds to $\xi(T) \sim 1/T$. (b) The dependence of ξ on $(x - x_c)$ along the pseudogap temperature T^*. The relationship is well fit by $\xi(x - x_c) \sim 1/|x - x_c|$.

$(x - x_c)^{-1}$, as shown in Fig. 3.3(b). If interpreted in terms of the clean AF quantum critical

scenario, which may be questionable due to disorder, this is consistent with $z = 1$ and $\nu = 1$. Angle resolved photoemission spectroscopy (ARPES) for NCCO shows a reduced quasiparticle weight at the hot spots[86, 87]. This is in qualitative agreement with the prediction of Eq. (39), which implies that the quasiparticle weight vanishes at the hot spots, as compared to the region away from the hot spots where quasiparticles are well defined. Although the spectroscopic measurements are in qualitative agreement with the theoretical predictions, we believe that more experiments are needed to make quantitative comparisons. On the theoretical side, transport properties need to be better understood, for which electrons away from hot spots are expected to play an important role.

Chapter 4

Conclusion

In this thesis, we have studied the low-energy effective field theory for the antiferromagnetic quantum critical metal in two approaches. The first approach is perturbative, where a co-dimensional regularization scheme is used to gain controlled access to the low-energy physics. We found a stable fixed point to the leading order in the perturbation theory, at which a ratio of velocities flows to zero at low energies. The ratio of velocities can be used as a new control parameter even in two dimensions, as a large class of diagrams are suppressed at low energies.

In order to solve the theory directly in two dimensions, we construct a non-perturbative ansatz by a straightforward extension of the critical exponents obtained from the perturbative analysis. The infinite set of diagrams that survive in the limit the velocity ratio becomes small is summed through a self-consistent equation that includes a vertex correction. From this, we show that the non-perturbative ansatz is consistent. The emergent control parameter enables us to write down exact critical exponents at this fixed point, as well as other observables such as spin susceptibility and specific heat.

The exact solution of the low-energy theory is an important step towards the full understanding of the layered compounds believed to harbor the AF quantum critical metal. It opens the door to understanding their physical properties in a controlled way. The most obvious open problem to be understood in the future is the superconducting instability. The strong correlations are widely believed to be responsible for the novel superconductivity observed in materials, and a systematic study of this transition is important to understand physical properties of the compounds. Another very important problem is that of magnetic impurities in the otherwise clean metal, also known as the Kondo problem. Every system has some impurities, and the presence of magnetic ones has a particularly stark effect on the resistivity, introducing a logarithmic upturn at low temperatures in the case of conventional metals. However, not much progress has been made for the problem of a magnetic impurity in a non-Fermi liquid, mainly because non-Fermi liquid states have not been well understood even in the clean limit. Our solution provides grounds for a controlled approach to this problem, which is of large experimental interest.

Our analysis in this thesis has focused on the regions on the Fermi surface near the hot spots. Both of the above future directions require a study of the theory that takes into account electrons away from the hot spot. For these problems in which important scatterings are not restricted to the hot spots, a functional renormalization group approach is required to take into account the momentum-dependent renormalization.

Appendix A

Appendix to Chapter 2

I The beta functions and the anomalous dimensions

In this section we summarize the expressions for the beta functions and the anomalous dimensions derived from the minimal subtraction scheme. More details can be found in Ref. [43]. The renormalized action is given by the sum of the classical action and the counter terms which can be expressed in terms of bare fields and bare couplings,

$$\begin{aligned}
\mathcal{S}_{ren} \;=\; & \sum_{n=1}^{4}\sum_{\sigma=1}^{N_c}\sum_{j=1}^{N_f}\int dk_B\;\bar{\Psi}_{B;n,\sigma,j}(k_B)\Big[i\mathbf{\Gamma}\cdot\mathbf{K}_B + i\gamma_{d-1}\epsilon_n(\vec{k}_B;v_B)\Big]\Psi_{B;n,\sigma,j}(k) \\
& +\frac{1}{4}\int dq_B\;\Big[|\mathbf{Q}_B|^2 + \;c_B^2\,|\vec{q}_B|^2\Big]\mathrm{Tr}\left[\Phi_B(-q_B)\;\Phi_B(q_B)\right] \\
& +i\frac{g_B}{\sqrt{N_f}}\sum_{n=1}^{4}\sum_{\sigma,\sigma'=1}^{N_c}\sum_{j=1}^{N_f}\int dk_B\,dq_B\;\Big[\bar{\Psi}_{B;\bar{n},\sigma,j}(k_B+q_B)\Phi_{B;\sigma,\sigma'}(q_B)\gamma_{d-1}\Psi_{B;n,\sigma',j}(k_B)\Big] \\
& +\frac{1}{4}\int dk_{1B}\,dk_{2B}\,dq_B\;\Big[u_{1B}\mathrm{Tr}\left[\Phi_B(k_{1B}+q_B)\Phi_B(k_{2B}-q_B)\right]\mathrm{Tr}\left[\Phi_B(-k_{1B})\Phi_B(-k_{2B})\right] \\
& +u_{2B}\mathrm{Tr}\left[\Phi_B(k_{1B}+q_B)\Phi_B(k_{2B}-q_B)\Phi_B(-k_{1B})\Phi_B(-k_{2B})\right]\Big]. \qquad \text{(A45)}
\end{aligned}$$

The renormalized quantities are related to the bare ones through $\mathbf{K} = \mathcal{Z}_\tau^{-1}\;\mathbf{K}_B$, $\vec{k} = \vec{k}_B$, $\Psi_{n,\sigma,j}(k) = \mathcal{Z}_\psi^{-\frac{1}{2}}\;\Psi_{B;n,\sigma,j}(k_B)$, $\Phi(q) = \mathcal{Z}_\phi^{-\frac{1}{2}}\;\Phi_B(q_B)$, $v = \frac{\mathcal{Z}_3}{\mathcal{Z}_2}\;v_B$, $c = \left[\frac{\mathcal{Z}_\phi\;\mathcal{Z}_\tau^{d-1}}{\mathcal{Z}_5}\right]^{\frac{1}{2}}\;c_B$, $g = \frac{\mathcal{Z}_\psi\;\mathcal{Z}_\phi^{\frac{1}{2}}\;\mathcal{Z}_\tau^{2(d-1)}}{\mathcal{Z}_6}\;\mu^{-\frac{3-d}{2}}\;g_B$, $u_1 = \frac{\mathcal{Z}_\phi^2\mathcal{Z}_\tau^{3(d-1)}}{\mathcal{Z}_7}\;\mu^{-(3-d)}\;u_{1B}$, $u_2 = \frac{\mathcal{Z}_\phi^2\mathcal{Z}_\tau^{3(d-1)}}{\mathcal{Z}_8}\;\mu^{-(3-d)}\;u_{2B}$, where $\mathcal{Z}_\tau = \frac{\mathcal{Z}_1}{\mathcal{Z}_3}$, $\mathcal{Z}_\psi = \mathcal{Z}_1\;\mathcal{Z}_\tau^{-d}$, $\mathcal{Z}_\phi = \mathcal{Z}_4\;\mathcal{Z}_\tau^{-(d+1)}$ and $\mathcal{Z}_n = 1 + \mathcal{A}_n$. The scaling dimension of $\vec{k}$ is fixed to be 1. By requiring that the bare quantities are independent of the scale μ, we obtain the dynamical critical exponent, the anomalous dimensions and the beta functions as

$$z = \left[1 + (Z'_{1,1} - Z'_{3,1})\right]^{-1}, \qquad \text{(A46)}$$

$$\eta_\psi = -\frac{\epsilon}{2}\, z\left(Z'_{1,1} - Z'_{3,1}\right) + \frac{1}{2}\, z\left(2Z'_{1,1} - 3Z'_{3,1}\right), \tag{A47}$$

$$\eta_\phi = -\frac{\epsilon}{2}\, z\left(Z'_{1,1} - Z'_{3,1}\right) + \frac{1}{2}\, z\left(4Z'_{1,1} - 4Z'_{3,1} - Z'_{4,1}\right), \tag{A48}$$

$$\frac{dv}{dl} = -z\, v\left(Z'_{2,1} - Z'_{3,1}\right), \tag{A49}$$

$$\frac{dc}{dl} = -\frac{1}{2}\, z\, c\left(2Z'_{1,1} - 2Z'_{3,1} - Z'_{4,1} + Z'_{5,1}\right), \tag{A50}$$

$$\frac{dg}{dl} = z\, g\left[\frac{\epsilon}{2} + \frac{1}{2}\left(2Z'_{3,1} + Z'_{4,1} - 2Z'_{6,1}\right)\right], \tag{A51}$$

$$\frac{du_1}{dl} = z\, u_1\left[\epsilon - \left(2Z'_{1,1} - 2Z'_{3,1} - 2Z'_{4,1} + Z'_{7,1}\right)\right], \tag{A52}$$

$$\frac{du_2}{dl} = z\, u_2\left[\epsilon - \left(2Z'_{1,1} - 2Z'_{3,1} - 2Z'_{4,1} + Z'_{8,1}\right)\right], \tag{A53}$$

where $l = -\ln\mu$ is the logarithmic length scale, and $Z'_{n,1} \equiv \left(\frac{1}{2}\, g\partial_g + u_i\partial_{u_i}\right) Z_{n,1}$.

II Computation of the boson self energy at two loops

In this section we compute the quantum corrections to the spatial part of the boson self-energy. Among the two-loop diagrams, only Fig. 2.3 contributes. It is written as

$$\delta\Gamma^{2L}_{0,2} = -\frac{\mu^{2\epsilon}}{4}\frac{4g^4}{N_c N_f}\int dp\; \Upsilon^{2L}_{0,2}(p)\mathrm{Tr}[\Phi(-p)\Phi(p)], \tag{B54}$$

where

$$\Upsilon^{2L}_{0,2}(p) = \sum_n \int dk\, dq\; \mathrm{Tr}\left[\gamma_{d-1}G_n(q+k)\gamma_{d-1}G_{\bar{n}}(p+q+k)\gamma_{d-1}G_n(p+k)\gamma_{d-1}G_{\bar{n}}(k)\right] D(q). \tag{B55}$$

Since we are interested in the momentum-dependent part, we set $\mathbf{P} = 0$. We first perform the frequency integrations, which introduces four Feynman parameters x_1, x_2, y_1, y_2, followed by the spatial integrations. The final expression is given by

$$\Upsilon^{2L;a}_{0,2}(\vec{p}) = -\frac{1}{\epsilon}\frac{h_5(v,c)}{v^2}(p_x^2 + p_y^2) + \mathcal{O}(\epsilon^0), \tag{B56}$$

where $h_5(v,c)$ is defined as

$$h_5(v,c) = -\frac{2}{(4\pi)^2}\int_0^1 dx_1 \int_0^{1-x_1} dx_2 \int_0^1 dy_1 \int_0^{1-y_1} dy_2\; \left(Av^2 + B\right), \tag{B57}$$

with

$$A = -\frac{1}{128\pi^2}\left(\frac{4\left(b_1+b_2+b_3\right)\left(2\left(1-y_1-y_2\right) - \left(x_1+x_2\right)\left(1-2y_1-2y_2\right)\right)}{\sqrt{a_1\, a_2\, a_3\, a_4}\left(1-x_1-x_2\right)\left(x_1+x_2\right)^2}\right.$$

$$
\begin{aligned}
&-\frac{2a_1\,(b_1+b_2+b_3)\,(a_2\,a_4\,d_{2,3}+a_3\;(a_4\,d_{2,2}+a_2\,d_{2,4}))}{(a_1\,a_2\,a_3\,a_4)^{\,3/2}}+\frac{4\,(d_{2,5}+d_{2,6}+d_{2,7})}{\sqrt{a_1\,a_2\,a_3\,a_4}}\\
&+\frac{3\,(b_1+b_2+b_3)\,(1-y_1-y_2)\,d_{3,1}}{\sqrt{a_1\,a_2\,a_3}\,a_4^{\,5/2}\,(1-x_1-x_2)^{\,2}\,(x_1+x_2)^{\,2}}+\frac{a_1\,(b_1+b_2+b_3)\,(1-y_1-y_2)\,(a_3\,d_{3,2}+a_2\,d_{3,3})}{(a_1\,a_2\,a_3\,a_4)^{\,3/2}\,(1-x_1-x_2)^{\,2}\,(x_1+x_2)^{\,2}}\\
&-\frac{2a_1\,(1-y_1-y_2)\,(a_2\,a_4\;(d_{3,7}+d_{3,8}+d_{3,9})+a_3\;(a_4\;(d_{3,4}+d_{3,5}+d_{3,6})+a_2\;(d_{3,10}+d_{3,11}+d_{3,12})))}{(a_1\,a_2\,a_3\,a_4)^{\,3/2}\,(1-x_1-x_2)^{\,2}\,(x_1+x_2)^{\,2}}\Bigg),
\end{aligned}
$$

B = A with $(b_2\to -b_2, d_{2,6}\to -d_{2,6}, d_{3,5}\to -d_{3,5}, d_{3,8}\to -d_{3,8}, d_{3,11}\to -d_{3,11})$.

Here $d_{n,m}$ are defined as

$$
\begin{aligned}
d_{2,2} &= -c_1\,((1-x_1-x_2)\,(x_1+x_2))^{\,-2}\,(1-y_1-y_2)\,,\\
d_{2,3} &= (-1+x_1+x_2-c_2\,(-1+c_4+x_1+x_2)+c_4\,(2-x_1-x_2+c_1\,(-1+c_4+x_1+x_2)))\\
&\quad\times(-1+y_1+y_2)\,((1-x_1-x_2)\,(x_1+x_2))^{\,-2},\\
d_{2,4} &= \Big(c_1c_5^2\,(-1+y_1+y_2)+(-1+x_1+x_2)\,(-1+y_1+y_2)-c_8^2\,\big(1-c_1c_4^2-x_1-x_2+c_2\,(-1+c_4+x_1+x_2)\\
&\quad+c_4\,(-2+x_1+x_2-c_1\,(-1+x_1+x_2)))\,(-1+y_1+y_2)-c_5\,(-1+x_1+x_2-c_8\,(-2+c_2+x_1+x_2)\\
&\quad+c_1\,(2-x_1-x_2+c_8\,(-1+2c_4+x_1+x_2)))\,(-1+y_1+y_2)+c_8\,\big(-4+3x_1+3x_2+4y_1-4x_1y_1+x_1^2y_1\\
&\quad-4x_2y_1+2x_1x_2y_1+x_2^2y_1+4y_2-4x_1y_2+x_1^2y_2-4x_2y_2+2x_1x_2y_2+x_2^2y_2+c_2\,(-2+x_1+x_2)\,(-1+y_1+y_2)\\
&\quad-c_4\,(1-x_1-x_2+c_1\,(-2+x_1+x_2))\,(-1+y_1+y_2))\Big)\,((1-x_1-x_2)\,(x_1+x_2))^{\,-2},
\end{aligned}
$$

$$
\begin{aligned}
d_{2,5} &= \Big(c_{11}\,(-c_9+c_8c_{11})\,(-1+x_1+x_2)\,(x_1+x_2)+\big(c_1c_5^2c_{11}^2+c_1c_4^2\,(1+c_9-c_8c_{11})^{\,2}+c_9\,(-1+x_1+x_2)\\
&\quad-(-1+c_2)\,c_9^2\,(-1+x_1+x_2)-2c_8c_9c_{11}\,(-1+x_1+x_2)+c_5c_9c_{11}\,(2-x_1-x_2+c_1\,(-1+x_1+x_2))\\
&\quad+c_2c_{11}\,(-1+c_8c_{11})\,(-2+c_5+x_1+x_2-c_8\,(-1+x_1+x_2))+c_{11}\,(-2-c_{11}+x_1+c_{11}x_1+x_2+c_{11}x_2\\
&\quad-c_9\,(-2+x_1+x_2)^{\,2}+c_8^2c_{11}\,(-1+x_1+x_2)+c_8\,\big(1-x_1-x_2+c_{11}\,(-2+x_1+x_2)^{\,2}\big)\big)\\
&\quad-c_4\,(1+c_9-c_8c_{11})\,(-1-c_{11}+2c_1c_{11}-2c_1c_5c_{11}+2c_8c_{11}-c_1c_8c_{11}+c_2\,(1+c_9-c_8c_{11})+c_{11}x_1-c_1c_{11}x_1\\
&\quad-c_8c_{11}x_1+c_1c_8c_{11}x_1+c_{11}x_2-c_1c_{11}x_2-c_8c_{11}x_2+c_1c_8c_{11}x_2+c_9\,(-2+x_1+x_2-c_1\,(-1+x_1+x_2)))\\
&\quad-c_2c_9\,(-1+x_1+x_2+c_{11}\,(-2+c_5+x_1+x_2-2c_8\,(-1+x_1+x_2)))-c_5c_{11}\,(-1+c_{11}\,(-1+x_1+x_2\\
&\quad-c_8\,(-2+x_1+x_2)+c_1\,(2-x_1-x_2+c_8\,(-1+x_1+x_2)))))\,(-1+y_1+y_2)\Big)\,((1-x_1-x_2)\,(x_1+x_2))^{\,-2},
\end{aligned}
$$

$$
\begin{aligned}
d_{2,6} &= ((1-x_1-x_2)\,(x_1+x_2))^{\,-2}\Big(\,(-c_9c_{12}+c_8c_{11}\,(-1+2c_{12}))\,(-1+x_1+x_2)\,(x_1+x_2)+(((-1+c_2)\,c_8\\
&\quad+c_1\,(c_5-c_4c_8))\,(-\,(-1+c_5)\,c_{11}-c_4\,(1+c_9-c_8c_{11}))\,(-1+c_{12})-(-1+c_5-c_4c_8)\,(1+c_9-c_8c_{11}\\
&\quad-c_2\,(1+c_9-c_8c_{11})+c_1\,(c_5c_{11}+c_4\,(1+c_9-c_8c_{11})))\,(-1+c_{12})+(c_8\,(1+2c_{11}-c_5c_{11}+c_1c_5c_{11}\\
&\quad-2c_8c_{11}+c_2\,(-1+(-1+2c_8)\,c_{11})-(-1+c_1)\,c_4\,(-1+(-1+2c_8)\,c_{11}))+c_9\,(-1+(-1+c_1)\,c_5\,(-1+c_{12})\\
&\quad+2\,(-1+c_2+c_4-c_1c_4)\,c_8\,(-1+c_{12})+2c_{12}-c_2c_{12}-c_4c_{12}+c_1c_4c_{12})+(-1+c_8)\,((-1+c_2-(-1+c_1)\,c_4)\,c_{12}\\
&\quad+c_{11}\,(1+(-1+c_1)\,c_5-2\,(1+(-1+c_1)\,c_5+(-1+c_2+c_4-c_1c_4)\,c_8)\,c_{12})))\,(1-x_1-x_2)
\end{aligned}
$$

$$- c_8c_{11}\left(-1+c_{12}\right)\left(-1+x_1+x_2\right)^2+\left(c_9-c_8c_{11}\right)c_{12}\left(-1+x_1+x_2\right)^2\Big)\left(1-y_1-y_2\right)\Big),$$

$$\begin{aligned}
d_{2,7} &= \left(\left(1-x_1-x_2\right)\left(x_1+x_2\right)\right)^{-2}\Big(\left(\left(-1+c_{12}\right)\left(c_1\left(c_5-c_4c_8\right)\left(1+c_5\left(-1+c_{12}\right)-\left(-1+c_4\right)c_8\left(-1+c_{12}\right)-2c_{12}\right)\right.\right.\\
&- \left(1+c_2\left(-1+c_4\right)-2c_4\right)c_8^2\left(-1+c_{12}\right)+\left(-1+c_5\right)c_{12}+c_8\left(-2+c_2\left(1+c_5\left(-1+c_{12}\right)-2c_{12}\right)-2c_5\left(-1+c_{12}\right)\right.\\
&+ \left.\left.4c_{12}-c_4c_{12}\right)\right)-c_8x_1+\left(1-c_2+\left(-1+c_1\right)c_4\right)c_8^2x_1+\left(-1+c_1\right)c_5\left(-1+c_8\right)c_{12}x_1+c_8c_{12}x_1-2c_8^2c_{12}x_1\\
&- \left(-1+c_1\right)c_5c_8\left(-1+c_{12}\right)c_{12}x_1+\left(1-c_2+\left(-1+c_1\right)c_4\right)c_8^2c_{12}^2x_1+c_{12}\left(-1+\left(1+\left(-1+c_1\right)c_5\right)c_{12}\right)x_1\\
&+ c_8\left(-1+c_{12}\right)x_2+\left(1-c_2+\left(-1+c_1\right)c_4\right)c_8^2\left(-1+c_{12}\right)^2x_2+\left(1+\left(-1+c_1\right)c_5\right)\left(-1+c_{12}\right)c_{12}x_2\\
&+ c_8\left(\left(c_2-\left(-1+c_1\right)c_4\right)c_{12}\left(\left(-1+2c_8+c_{12}\right)x_1+\left(-1+c_{12}\right)x_2\right)-\left(-1+c_1\right)c_5\left(x_1+\left(-1+c_{12}\right)^2x_2\right)\right)\\
&\times\left(-1+y_1+y_2\right)+c_8\left(-1+c_{12}\right)c_{12}\left(x_1+x_2\right)\left(3+\left(-4+x_1+x_2\right)y_1+\left(-4+x_1+x_2\right)y_2\right)\Big),
\end{aligned}$$

$$\begin{aligned}
d_{3,1} &= c_8\left(1-c_5+c_4c_8\right)\left(-\left(-1+c_2\right)c_8+c_1\left(-c_5+c_4c_8\right)\right),\\
d_{3,2} &= c_1c_8,\\
d_{3,3} &= 1-c_5+c_2\left(-1+c_5-3c_4c_8\right)+c_4\left(3c_8+c_1\left(1-2c_5+3c_4c_8\right)\right),\\
d_{3,4} &= c_1c_{11}\left(-c_9+c_8c_{11}\right),\\
d_{3,5} &= -c_1\left(c_8c_{11}\left(1-2c_{12}\right)+c_9c_{12}\right),\\
d_{3,6} &= c_1c_8\left(-1+c_{12}\right)c_{12},\\
d_{3,7} &= c_{11}\left(\left(-1+c_2\right)\left(-1+c_5\right)c_{11}+c_1c_4^2\left(-2-3c_9+3c_8c_{11}\right)\right.\\
&\quad \left.+ c_4\left(-2-3c_9+c_1c_{11}-2c_1c_5c_{11}+3c_8c_{11}+c_2\left(2+3c_9-3c_8c_{11}\right)\right)\right),
\end{aligned}$$

$$\begin{aligned}
d_{3,8} &= c_4\left(-1+c_2-c_1c_4\right)\left(2+3c_9\right)c_{12}-\left(-1+c_5-3c_4c_8-c_1c_4\left(1-2c_5+3c_4c_8\right)+c_2\left(1-c_5+3c_4c_8\right)\right)c_{11}\left(-1+2c_{12}\right),\\
d_{3,9} &= -\left(-1+c_5-3c_4c_8-c_1c_4\left(1-2c_5+3c_4c_8\right)+c_2\left(1-c_5+3c_4c_8\right)\right)\left(-1+c_{12}\right)c_{12},\\
d_{3,10} &= c_1c_4^2c_8+\left(1-c_5+c_2\left(-1+c_5-3c_4c_8\right)+c_4\left(3c_8+c_1\left(1-2c_5+3c_4c_8\right)\right)\right)c_9^2+3c_8\left(-1+c_5-c_4c_8\right)c_{11}\left(1-c_2\right.\\
&+ \left.2\left(c_1c_5+\left(-1+c_2-c_1c_4\right)c_8\right)c_{11}\right)+c_9\left(\left(-1+c_2\right)\left(-1+c_5-2c_4c_8\right)-3\left(\left(-1+c_2\right)c_8\left(-2+2c_5-3c_4c_8\right)\right.\right.\\
&+ \left.\left.c_1\left(c_5^2+c_4c_8\left(2+3c_4c_8\right)-c_5\left(1+4c_4c_8\right)\right)\right)c_{11}\right)-c_4\left(c_1\left(-1+2c_5\right)c_9+c_8\left(-1+c_2+2\left(-1+c_2-2c_1c_4\right)c_9\right.\right.\\
&+ \left.\left.3\left(-\left(-1+c_2\right)c_8+c_1\left(1-2c_5+2c_4c_8\right)\right)c_{11}\right)\right),
\end{aligned}$$

$$\begin{aligned}
d_{3,11} &= -c_1\left(-1+c_5\right)c_5c_9\left(-2+3c_{12}\right)+3c_4\left(1-c_2+c_1c_4\right)c_8^3c_{11}\left(-3+4c_{12}\right)+c_8^2\left(-c_1c_4^2\left(2+3c_9\right)\left(-2+3c_{12}\right)\right.\\
&+ 3\left(-1+c_2\right)\left(-1+c_5\right)c_{11}\left(-3+4c_{12}\right)+c_4\left(4-9c_1c_{11}+18c_1c_5c_{11}+c_9\left(6-9c_{12}\right)-6c_{12}+12c_1c_{11}c_{12}\right.\\
&- \left.\left.24c_1c_5c_{11}c_{12}+c_2\left(2+3c_9\right)\left(-2+3c_{12}\right)\right)\right)+c_8\left(\left(-1+c_5\right)\left(1+2c_9\right)\left(-2+3c_{12}\right)-c_2\left(-1+c_5\right)\left(1+2c_9\right)\right.\\
&\times \left.\left(-2+3c_{12}\right)+c_1\left(c_4\left(-1+2c_5\right)\left(1+2c_9\right)\left(-2+3c_{12}\right)+3\left(-1+c_5\right)c_5c_{11}\left(-3+4c_{12}\right)\right)\right),\\
d_{3,12} &= 3c_8\left(1-c_5+c_4c_8\right)\left(-\left(-1+c_2\right)c_8+c_1\left(-c_5+c_4c_8\right)\right)\left(1-3c_{12}+2c_{12}^2\right),
\end{aligned}$$

where a_n, b_n and c_n are given by

$$
\begin{aligned}
a_1 &= -\mathcal{X}_1\left(-1+y_1+y_2\right)\left(4v^2\left(-1+x_1+x_2\right)\left(x_1+x_2\right)\right)^{-1},\\
a_2 &= -\mathcal{X}_2\left(-1+y_1+y_2\right)\left(\mathcal{X}_1\left(-1+x_1+x_2\right)\left(x_1+x_2\right)\right)^{-1},\\
a_3 &= \mathcal{X}_3\left(\left(x_1+x_2\right)\mathcal{X}_2\right)^{-1},\\
a_4 &= \mathcal{X}_4\left(\left(x_1+x_2\right)\mathcal{X}_3\right)^{-1},\\
b_1 &= \mathcal{X}_4^{-1}\,c^2x_1y_1\left(-1+y_1+y_2\right)\left(c^2\left(-1+x_1\right)x_1y_2+\left(-1+c^2-v^2\right)x_2^2y_2+x_2\left(-c^2+c^2y_1+\left(-1+2c^2-v^2\right)x_1y_2\right)\right),\\
b_2 &= -\mathcal{X}_4^{-1}\,2c^2\left(-1+v^2\right)x_1x_2\left(x_1+x_2\right)y_1y_2\left(-1+y_1+y_2\right),\\
b_3 &= \mathcal{X}_4^{-1}\,c^2x_2\left(\left(-1+c^2-v^2\right)x_1^2y_1+c^2\left(-1+x_2\right)x_2y_1+x_1\left(\left(-1+2c^2-v^2\right)x_2y_1+c^2\left(-1+y_2\right)\right)\right)y_2\left(-1+y_1+y_2\right),\\
c_1 &= -\mathcal{X}_1^{-1}\,c^2\left(-1+v^2\right)\left(-1+x_1+x_2\right),\\
c_2 &= -\mathcal{X}_1^{-1}\,4v^2x_1,\\
c_4 &= c_1\,\mathcal{X}_1\,\mathcal{X}_2^{-1}\,x_1,\\
c_5 &= -\mathcal{X}_1\,\mathcal{X}_2^{-1}\,x_2,\\
c_8 &= \mathcal{X}_3^{-1}\,c^2\left(-1+v^2\right)x_1x_2\left(-1+y_1+y_2\right),\\
c_9 &= \mathcal{X}_3^{-1}\,c^2x_1\left(c^2-c^2x_1+\left(1-c^2+v^2\right)x_2\right)\left(-1+y_1+y_2\right),\\
c_{11} &= -\mathcal{X}_4^{-1}\,\left(c^2\left(-1+v^2\right)x_1x_2\left(x_1+x_2\right)y_1\left(-1+y_1+y_2\right)\right),\\
c_{12} &= -\mathcal{X}_4^{-1}\,\left(c^2x_2\left(\left(1-c^2+v^2\right)x_1^2y_1-c^2\left(-1+x_2\right)x_2y_1+x_1\left(\left(1-2c^2+v^2\right)x_2y_1-c^2\left(-1+y_2\right)\right)\right)\left(-1+y_1+y_2\right)\right)
\end{aligned}
$$

with

$$
\begin{aligned}
\mathcal{X}_1 &= \left(c^2+\left(-4+c^2\right)v^2\right)x_1+c^2\left(1+v^2\right)\left(-1+x_2\right),\\
\mathcal{X}_2 &= c^2\left(-1+c^2-v^2\right)x_1^2+c^2\left(-1+x_2\right)\left(-c^2+\left(-1+c^2-v^2\right)x_2\right)\\
&\quad +x_1\left(c^2\left(1-2c^2+v^2\right)+2\left(c^4+2v^2-c^2\left(1+v^2\right)\right)x_2\right),\\
\mathcal{X}_3 &= c^2\left(-1+c^2-v^2\right)x_1^3y_1+c^2\left(-1+x_2\right)x_2\left(-c^2+\left(-1+c^2-v^2\right)x_2\right)y_1+x_1\left(\left(3c^4+4v^2-3c^2\left(1+v^2\right)\right)x_2^2y_1\right.\\
&\quad +c^2x_2\left(\left(1-3c^2+v^2\right)y_1+\left(-1+c^2-v^2\right)\left(-1+y_2\right)\right)-c^4\left(-1+y_2\right)\Big)+x_1^2\left(\left(c^2\left(1-c^2+v^2\right)\right.\right.\\
&\quad \left.\left.+\left(3c^4+4v^2-3c^2\left(1+v^2\right)\right)x_2\right)y_1+c^4\left(-1+y_2\right)\right),\\
\mathcal{X}_4 &= c^2\left(-1+c^2-v^2\right)x_1^4y_1y_2+x_1^3\left(\left(c^2\left(1-c^2+v^2\right)+4\left(-1+c^2\right)\left(c^2-v^2\right)x_2\right)y_1+c^4\left(-1+y_2\right)\right)y_2\\
&\quad +c^2\left(-1+x_2\right)x_2^2y_1\left(-c^2+c^2y_1+\left(-1+c^2-v^2\right)x_2y_2\right)+x_1x_2\left(c^2\left(-1+2c^2-v^2\right)x_2y_1^2\right.\\
&\quad +c^2\left(-1+y_2\right)\left(-c^2+\left(-1+c^2-v^2\right)x_2y_2\right)+y_1\left(4\left(-1+c^2\right)\left(c^2-v^2\right)x_2^2y_2+c^4\left(-1+2y_2\right)\right.\\
&\quad \left.\left.+c^2x_2\left(1-2c^2+v^2+\left(1-3c^2+v^2\right)y_2\right)\right)\right)+x_1^2\left(2\left(3c^4+4v^2-3c^2\left(1+v^2\right)\right)x_2^2y_1y_2-c^4\left(-1+y_2\right)y_2\right.\\
&\quad \left.+c^2x_2\left(\left(-1+c^2-v^2\right)y_1^2+\left(-1+2c^2-v^2\right)\left(-1+y_2\right)y_2+y_1\left(1-c^2+v^2+\left(1-3c^2+v^2\right)y_2\right)\right)\right).
\end{aligned}
$$

To extract the leading behavior of $h_5(v,c)$ in the limit $v, c, w \equiv v/c$ are small, we approximate the integrand in $h_5(v,c)$ by its leading order term in this limit. This gives $h_5(v,c) = h_5^*\,w$

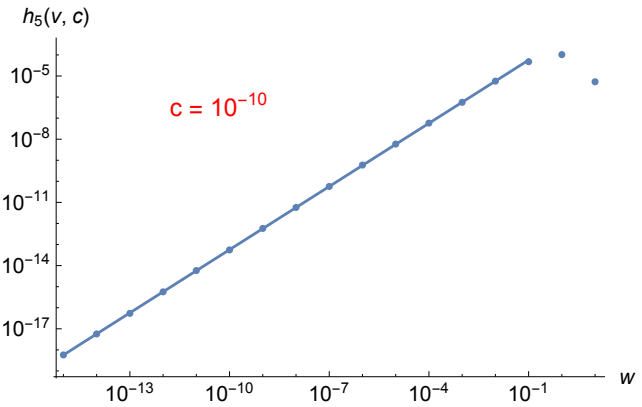

Figure B1: The dots represent $h_5(v,c)$ evaluated as a function of $w = v/c$ at fixed $c = 10^{-10}$. The line represents $L(w) = 5.7 \times 10^{-4}\, w$. It is noted that $h_5(v,c)$ deviates from the line beyond $w \sim 0.1$.

with $h_5^* \approx 5.7 \times 10^{-4}$ to the leading order in v, c, w. In Fig. (B1), we show the full $h_5(v,c)$ as a function of $w = \frac{v}{c}$ for a small value of c, which confirms the linear behavior in the small w limit. The two-loop contribution to the quantum effective action is

$$\delta\Gamma^{2L}_{0,2} = \frac{1}{\epsilon}\frac{4}{N_c N_f}\frac{g^4}{v^2c^2}h_5(v,c)\int dp\,\frac{1}{4}c^2|\vec{p}|^2\mathrm{Tr}[\Phi(-p)\Phi(p)] \;+\; \mathcal{O}(\epsilon^0). \tag{B58}$$

Combining Eq. (B58) with the one-loop quantum effective action obtained in Ref. [43], we obtain the counter terms as

$$Z_{1,1} = -\frac{(N_c^2-1)}{4\pi^2 N_c N_f}\,\frac{g^2}{c}\,h_1(v,c), \tag{B59}$$

$$Z_{2,1} = \frac{(N_c^2-1)}{4\pi^2 N_c N_f}\,\frac{g^2}{c}\,h_2(v,c), \tag{B60}$$

$$Z_{3,1} = -Z_{2,1}, \tag{B61}$$

$$Z_{4,1} = -\frac{1}{4\pi}\,\frac{g^2}{v}, \tag{B62}$$

$$Z_{5,1} = -\frac{4}{N_c N_f}\frac{g^4}{v^2c^2}h_5(v,c), \tag{B63}$$

$$Z_{6,1} = -\frac{1}{8\pi^3 N_c N_f}\,\frac{g^2}{c}\,h_3(v,c), \tag{B64}$$

$$Z_{7,1} = \frac{1}{2\pi^2c^2}\left[(N_c^2+7)u_1 + 2\left(2N_c - \frac{3}{N_c}\right)u_2 + 3\left(1+\frac{3}{N_c^2}\right)\frac{u_2^2}{u_1}\right], \tag{B65}$$

$$Z_{8,1} = \frac{1}{2\pi^2c^2}\left[12u_1 + 2\left(N_c - \frac{9}{N_c}\right)u_2\right]. \tag{B66}$$

Here $h_1(v,c)$, $h_2(v,c)$, and $h_3(v,c)$ are given by[43]

$$h_1(v,c) = \int_0^1 dx\,\sqrt{\frac{1-x}{c^2+(1+v^2-c^2)x}}$$

$$= \frac{\pi\left(1+v^2\right) - 2c\sqrt{1-c^2+v^2} - i\left(1+v^2\right)\left(\log\left(1+v^2\right) - 2\log\left(ic+\sqrt{1-c^2+v^2}\right)\right)}{2\left(1-c^2+v^2\right)^{3/2}},$$

$$h_2(v,c) = c^2\int_0^1 dx\sqrt{\frac{1-x}{(c^2+(1+v^2-c^2)x)^3}}$$

$$= -\frac{c\left(-2\sqrt{1-c^2+v^2} - ic\left(\log\left(-1-v^2\right) - 2\log\left(ic+\sqrt{1-c^2+v^2}\right)\right)\right)}{\left(1-c^2+v^2\right)^{3/2}},$$

$$h_3(v,c) = \int_0^1 dx_1\int_0^{1-x_1} dx_2$$
$$\frac{\pi c\left(8v^2x_1x_2 + 2c^4\left(-1+x_1+x_2\right)^2 - c^2\left(-1+x_1+x_2\right)\left(1+2x_1+2x_2+v^2\left(-1+2x_1+2x_2\right)\right)\right)}{\left(4v^2x_1x_2 + c^4\left(-1+x_1+x_2\right)^2 - c^2\left(1+v^2\right)\left(-1+x_1+x_2\right)\left(x_1+x_2\right)\right)^{3/2}}.$$

From the expressions for $Z_{n,1}$, we obtain the beta functions for $\lambda \equiv \frac{g^2}{v}, x \equiv \frac{g^2}{c^3}, w \equiv \frac{v}{c}, \kappa_i \equiv \frac{u_i}{c^2}$,

$$\frac{d\lambda}{dl} = z\,\lambda\left(\epsilon - \frac{\lambda}{4\pi} + \frac{1}{4\pi^3 N_c N_f}\,\lambda w\, h_3(v,c)\right), \tag{B67}$$

$$\frac{dx}{dl} = z\,x\left(\epsilon - \frac{3(N_c^2-1)}{4\pi^2 N_c N_f}\,\lambda w\, h_1(v,c) + \frac{(N_c^2-1)}{4\pi^2 N_c N_f}\,\lambda w\, h_2(v,c) + \frac{\lambda}{8\pi} - \frac{12}{N_c N_f}\frac{\lambda x}{w}h_5(v,c) + \frac{\lambda w\, h_3(v,c)}{4\pi^3 N_c N_f}\right), \tag{B68}$$

$$\frac{dw}{dl} = \frac{1}{2}\,z\,w\left(-\frac{(N_c^2-1)}{2\pi^2 N_c N_f}\,\lambda w\, h_1(v,c) - \frac{(N_c^2-1)}{2\pi^2 N_c N_f}\,\lambda w\, h_2(v,c) + \frac{\lambda}{4\pi} - \frac{8}{N_c N_f}\frac{\lambda x}{w}h_5(v,c)\right), \tag{B69}$$

$$\frac{d\kappa_1}{dl} = z\,\kappa_1\left(\epsilon - \frac{\lambda}{4\pi} - \frac{8}{N_c N_f}\frac{\lambda x}{w}h_5(v,c) - \frac{1}{2\pi^2}\left((N_c^2+7)\kappa_1 + 2\left(2N_c - \frac{3}{N_c}\right)\kappa_2 + 3\left(1+\frac{3}{N_c^2}\right)\frac{\kappa_2^2}{\kappa_1}\right)\right), \tag{B70}$$

$$\frac{d\kappa_2}{dl} = z\,\kappa_2\left(\epsilon - \frac{\lambda}{4\pi} - \frac{8}{N_c N_f}\frac{\lambda x}{w}h_5(v,c) - \frac{1}{2\pi^2}\left(12\kappa_1 + 2\left(N_c - \frac{9}{N_c}\right)\kappa_2\right)\right). \tag{B71}$$

The leading order behavior of $h_i(v,c)$ in the limit of small v, c, w are $h_1(v,c) = \frac{\pi}{2}$, $h_2(v,c) = 2c$, $h_3(v,c) = 2\pi^2$.

III Upper bound of higher-loop diagrams

Here we estimate the magnitude of higher-loop diagrams without self-energy insertions at the M1L fixed point. Since $\kappa_i = 0$ at the fixed point, we consider diagrams made of Yukawa vertices only. The discussion closely follows the one in Appendix B, and we will be brief here. A general L-loop diagram can be written as

$$I \sim g^V \int \prod_{r=1}^{L} dp_r \left(\prod_{l=1}^{I_f} \frac{1}{\mathbf{K}_l\cdot\mathbf{\Gamma} + \epsilon_{n_l}(k_l)\gamma_{d-1}}\right)\left(\prod_{m=1}^{I_b}\frac{1}{|\mathbf{Q}_m|^2 + c^2(q_{m,x}^2 + q_{m,y}^2)}\right). \tag{C72}$$

Here V is the number of Yukawa vertices. I_f, I_b are the number of fermion and boson propagators, respectively. p_r's represent the internal momenta. k_l (q_m) is the momentum that flows through the l-th fermion (m-th boson) propagator, which is given by a linear combination of the

internal and external momenta. n_l is the patch index of the l-th fermion line. Without loss of generality, we can focus on diagrams that involve only patches 1 and 3. We are ignoring the γ matrices coming from the Yukawa vertices as they play no role in the estimation.

The dependence of k_l and q_m on the internal momenta is determined by the choice of loops. One can choose the loop momenta such that $L - L_f$ boson propagators become exclusive propagators, in the sense that each of them depends exclusively on only one internal momentum, where L_f is the number of fermion loops. Since the limit of small v, c, w does not affect the frequency integrations, we focus on the spatial parts of the propagators. The integrations for $p_{r,x}, p_{r,y}$ in Eq. (C72) can be written as

$$I \sim g^V \int \prod_{r=1}^{L} dp_{r,x} dp_{r,y} \left(\prod_{m=1}^{L-L_f} \frac{1}{(cp_{m,x})^2 + (cp_{m,y})^2} \right) \left(\prod_{l=1}^{I_f} \frac{1}{E_l(p)} \right) R[p].$$

Here we have dropped the frequency variables and all the γ matrices. The first group represents the exclusive boson propagators for the $L - L_f$ non-fermion loops. The second group represents all fermion propagators, and the energy of the fermion is written $E_l(p) \equiv \epsilon_l(k_l(p))$, where $k_l(p)$ is the momentum that flows through the l-th fermion propagator which is a function of internal momenta. $R[p]$ represents the remaining boson propagators in the diagram.

Now we change variables in a way that the divergence in the small v, c limit becomes manifest. The first $L - L_f$ variables are chosen to be $p_i^{'} \equiv cp_{i,x}$ with $1 < i \leq L - L_f$. The remaining $L + L_f$ variables are chosen among $\{E_l(p)\}$. $\{p_i', E_l(p)\}$ are expressed in terms of $\{vp_{r,x}, p_{r,y}\}$ as

$$\begin{pmatrix} p_1^{'} \\ p_2^{'} \\ \vdots \\ p_{L-L_f}^{'} \\ \\ E_1 \\ E_2 \\ \vdots \\ E_{I_f} \end{pmatrix} = \begin{pmatrix} \frac{c}{v}\mathbb{I}_{L-L_f} & 0 \\ \mathbb{A} & \mathbb{V} \end{pmatrix} \begin{pmatrix} vp_{1,x} \\ vp_{2,x} \\ \vdots \\ vp_{L-L_f,x} \\ \\ vp_{L-L_f+1,x} \\ vp_{L-L_f+2,x} \\ \vdots \\ vp_{L,x} \\ p_{1,y} \\ p_{2,y} \\ \vdots \\ p_{L,y} \end{pmatrix}. \tag{C73}$$

Here, $\mathbb{I}_a$ is the $a \times a$ identity matrix. $\mathbb{A}$ is an $I_f \times (L - L_f)$ matrix whose matrix elements are given by $\mathbb{A}_{n,i} = \frac{1}{v}\frac{\partial E_n}{\partial p_{i,x}}$ with $1 \leq n \leq I_f$ and $1 \leq i \leq L - L_f$. $\mathbb{V}$ is an $I_f \times (L + L_f)$

matrix whose first L_f columns are given by $\mathbb{V}_{n,a-(L-L_f)} = \frac{1}{v}\frac{\partial E_n}{\partial p_{a,x}}$ for $L - L_f + 1 \leq a \leq L$ while the remaining L columns are given by $\mathbb{V}_{n,b+L_f} = \frac{\partial E_n}{\partial p_{b,y}}$ for $1 \leq b \leq L$. In Ref. [63] it is shown that the $L + L_f$ column vectors of $\mathbb{V}$ are linearly independent. Therefore, there exist $L + L_f$ row vectors of $\mathbb{V}$ that are linearly independent, which we label to be the l_k-th rows with $k = 1, ..., (L + L_f)$. Let $\tilde{\mathbb{V}}$ be the $(L + L_f) \times (L + L_f)$ matrix consisting of these rows. Then we define $p'_{L-L_f+k} \equiv E_{l_k}$ with $k = 1, ..., (L + L_f)$ as the remaining $(L + L_f)$ integration variables. The new momentum variables are given in terms of the old variables by

$$\begin{pmatrix} p'_1 \\ p'_2 \\ \vdots \\ p'_{2L} \end{pmatrix} = \begin{pmatrix} \frac{c}{v}\mathbb{I}_{L-L_f} & 0 \\ \tilde{\mathbb{A}} & \tilde{\mathbb{V}} \end{pmatrix} \begin{pmatrix} vp_{1,x} \\ vp_{2,x} \\ \vdots \\ vp_{L-L_f,x} \\ \\ vp_{L-L_f+1,x} \\ vp_{L-L_f+2,x} \\ \vdots \\ vp_{L,x} \\ p_{1,y} \\ p_{2,y} \\ \vdots \\ p_{L,y} \end{pmatrix}, \tag{C74}$$

where $\tilde{\mathbb{A}}$ is the collection of the l_k-th rows of $\mathbb{A}$, with $k = 1, ..., (L + L_f)$. The Jacobian of this change of variables is given by $Y^{-1}c^{-(L-L_f)}v^{-L_f}$, where $Y = |\det \tilde{\mathbb{V}}|$ is a numerical constant independent of v, c. Y is nonzero because $\tilde{\mathbb{V}}$ is invertible. In the new basis, it is manifest that for every integration variable p'_r, there is one propagator that guarantees the integrand decays at least as $1/p'_r$, in the limit $c, v \to 0$. Since there is no sub-diagram with a positive degree of UV divergence, the integrations over p'_r are at most logarithmically divergent in the UV cut-off or v, c. Therefore, the diagram is bounded by

$$I \sim \frac{g^V}{v^{L_f} c^{L-L_f}}, \tag{C75}$$

up to potential logarithmic corrections in v and c.

IV Beyond the modified one-loop order

In this appendix, we consider the effects of higher-loop diagrams in the small w limit. To the leading order in w, the higher-loop diagrams that need to be considered are the M1L diagrams

in which the boson propagator is dressed with the self-energy insertions in Figs. 2.2(a) and 2.3. An insertion of the self-energy in Fig. 2.2(a) adds one power of λ to $Z_{n,1}$, while an insertion of the self-energy in Fig. 2.3 adds one power of λx, up to logarithmic corrections in c, v for both insertions. We write the general form of the counter terms from the higher-loop diagrams as

$$Z_{1,1} = \lambda w \sum_{n,m=0}^{\infty} \lambda^{n+m} x^m a_{n,m}(c,v), \tag{D76}$$

$$Z_{2,1} = \frac{(\lambda w)^{\frac{3}{2}}}{x^{\frac{1}{2}}} \sum_{n,m=0}^{\infty} \lambda^{n+m} x^m b_{n,m}(c,v), \tag{D77}$$

$$Z_{3,1} = -Z_{2,1}, \tag{D78}$$

$$Z_{4,1} = -\frac{1}{4\pi}\lambda, \tag{D79}$$

$$Z_{5,1} = \lambda x \sum_{n,m=0}^{\infty} \lambda^{n+m} x^m h_{n,m}(c,v), \tag{D80}$$

$$Z_{6,1} = \lambda w \sum_{n,m=0}^{\infty} \lambda^{n+m} x^m r_{n,m}(c,v). \tag{D81}$$

Here, $a_{n,m}(c,v), b_{n,m}(c,v), h_{n,m}(c,v), r_{n,m}(c,v)$ are functions that grow at most logarithmically in c, v. For $n = m = 0$, they are independent of c, v, and given by $a_{0,0}(c,v) = -\frac{(N_c^2-1)}{8\pi N_c N_f}$, $b_{0,0}(c,v) = \frac{(N_c^2-1)}{2\pi^2 N_c N_f}$, $h_{0,0}(c,v) = -\frac{4\,h_5^*}{N_c N_f}$, $r_{0,0}(c,v) = -\frac{1}{4\pi N_c N_f}$. The relation $Z_{2,1} = -Z_{3,1}$ still holds because the external momentum can be passed through a single fermion line with the opposite patch index to the external lines.

We first establish that the fixed point still exists in the presence of general logarithmic corrections in v, c. It is straightforward to check that $w^* = 0$ remains as a fixed point. At $w = 0$, the beta functions for λ, x read

$$\frac{d\lambda}{dl} = z\,\lambda\left(\epsilon - \frac{1}{4\pi}\lambda\right), \tag{D82}$$

$$\frac{dx}{dl} = zx\left(\epsilon + \frac{1}{8\pi}\lambda + \frac{3}{2}\lambda x \sum_{n,m=0}^{\infty} (n+2m+2)\,\lambda^{n+m} x^m h_{n,m}(c,v)\right). \tag{D83}$$

While λ still flows to $\lambda^* = 4\pi\epsilon$, x no longer flows to an $\mathcal{O}(1)$ fixed point if $h_{n,m}(c,v)$ diverge logarithmically in the small v, c limit. This may be regarded as an indication that the theory has an instability. However, we show that such a runaway flow is an artifact of looking at the wrong parameter x for general ϵ. In other words, the relative rate at which v, c flow to zero depends on ϵ, and we have to take the ϵ-dependence into account in choosing the variable that represents the fixed point. To see this, we define a new variable $\tilde{x} \equiv \frac{x}{F(c,v)}$ with

$$F(c,v) = 1 + \sum_{p=1}^{\infty} \epsilon^p\, f_p(c,v), \tag{D84}$$

where we leave open the possibility that $f_p(c,v)$ depends on both c, v for the sake of full generality. The beta function for $\tilde{x}$ is given by

$$\frac{d\tilde{x}}{dl} = z\,\tilde{x} \quad \left[\epsilon + \left(3 + \frac{\partial_{\log(c)}F}{F}\right) Z'_{1,1} + \frac{\partial_{\log(v)}F}{F} Z'_{2,1} - \left(1 + \frac{\partial_{\log(c)}F}{F} + \frac{\partial_{\log(v)}F}{F}\right) Z'_{3,1} \right.$$
$$\left. -\frac{1}{2}\left(1 + \frac{\partial_{\log(c)}F}{F}\right) Z'_{4,1} + \frac{3}{2}\left(1 + \frac{\partial_{\log(c)}F}{3F}\right) Z'_{5,1} - 2Z'_{6,1}\right], \tag{D85}$$

where $Z'_{n,1} \equiv \left(\frac{1}{2}g\partial_g + u_i\partial_{u_i}\right) Z_{n,1}$. The point of introducing $\tilde{x}$ is that we can determine $F(c,v)$ such that $\tilde{x}$ flows to an $\mathcal{O}(1)$ fixed point, $\tilde{x}^*$. The conditions, $\frac{d\lambda}{dl} = 0$ and $\frac{d\tilde{x}}{dl} = 0$ imply

$$1 + 4\pi\,\tilde{x}^* \left(1 + \sum_{p=1}^{\infty} \epsilon^p\, f_p(c,v)\right) \sum_{n,m=0}^{\infty} (n + 2m + 2)\,\epsilon^{n+m} (\tilde{x}^*)^m \left(1 + \sum_{p=1}^{\infty} \epsilon^p\, f_p(c,v)\right)^m \tilde{h}_{n,m}(c,v) = 0 \tag{D86}$$

to the leading order in w, where $\tilde{h}_{n,m}(c,v) = (4\pi)^{n+m} h_{n,m}(c,v)$. Eq. (D86) can be solved for $\tilde{x}^*$ and $f_p(c,v)$ at every order in ϵ. For $\alpha = 0$, we have

$$1 + 8\pi\tilde{x}^*\tilde{h}_{0,0} = 0$$

which gives $\tilde{x}^* = -\frac{1}{8\pi\tilde{h}_{0,0}} = \frac{N_c N_f}{32\pi\, h_5^*} = x^*$. The equation for general $\alpha > 0$ contains only $f_{\alpha'}$ with $\alpha' \le \alpha$, from which f_α is uniquely fixed. For example, the first few equations in the series read

$$\begin{aligned}
2\tilde{h}_{0,0}f_1 + 4\tilde{x}^*\tilde{h}_{0,1} + 3\tilde{h}_{1,0} = 0 \qquad & \text{for } \alpha = 1, \\
2\tilde{h}_{0,0}f_2 + 6(\tilde{x}^*)^2\tilde{h}_{0,2} + f_1\left(8\tilde{x}^*\tilde{h}_{0,1} + 3\tilde{h}_{1,0}\right) + 5\tilde{x}^*\tilde{h}_{1,1} + 4\tilde{h}_{2,0} = 0 \qquad & \text{for } \alpha = 2, \\
2\tilde{h}_{0,0}f_3 + 4f_1^2\tilde{x}^*\tilde{h}_{0,1} + 8f_2\tilde{x}^*\tilde{h}_{0,1} + 8(\tilde{x}^*)^3\tilde{h}_{0,3} + 3f_2\tilde{h}_{1,0} + 7(\tilde{x}^*)^2\tilde{h}_{1,2} & \\
+2f_1\left(9(\tilde{x}^*)^2\tilde{h}_{0,2} + 5\tilde{x}^*\tilde{h}_{1,1} + 2\tilde{h}_{2,0}\right) + 6\tilde{x}^*\tilde{h}_{2,1} + 5\tilde{h}_{3,0} = 0 \qquad & \text{for } \alpha = 3,
\end{aligned}$$

each of which fixes $f_1(c,v)$, $f_2(c,v)$, $f_3(c,v)$, respectively. Therefore, $f_p(c,v)$ can be determined such that $\tilde{x}$ flows to an $\mathcal{O}(1)$ value to all orders in ϵ. At the fixed point with $(\lambda^*, \tilde{x}^*, w^*) = \left(4\pi\epsilon, \frac{N_c N_f}{32\pi\, h_5^*}, 0\right)$, Eq. (D85) implies that $Z'_{5,1} = -\epsilon$, and $Z_{1,1}$, $Z_{2,1}$, $Z_{3,1}$, $Z_{6,1}$ in Eqs. (D76), (D78), (D78), (D81) vanish because x is divergent at most logarithmically in w. The same conclusion holds for all other higher-loop diagrams suppressed by w. As a result, the ϵ-expansion is well defined, and the fixed point with $w^* = 0$ persists to all orders in ϵ. Furthermore, the critical exponents in Eqs. (A46), (A47), (A48) do not receive perturbative corrections beyond the M1L order at the fixed point. This is a rather remarkable feature attributed to $w^* = 0$.

The remaining question is whether the non-trivial fixed point remains attractive to all orders in ϵ. In the small ϵ limit this is indeed the case. For general ϵ, we cannot prove this from the present perturbative expansion without actually computing the counter terms to all orders in ϵ. However, from the non-perturbative calculation[56, 57], it is shown that w indeed flows to zero

for any $0 < \epsilon \leq 1$.

V Computation of physical properties

Here we provide some details of the derivation of the scaling forms of the Green's functions. The fermion Green's function satisfies the renormalization group equation[43],

$$\left[z\mathbf{K}\cdot\frac{\partial}{\partial\mathbf{K}}+\vec{k}\cdot\frac{\partial}{\partial\vec{k}}-\beta_w\frac{\partial}{\partial w}-\beta_x\frac{\partial}{\partial x}-\beta_\lambda\frac{\partial}{\partial\lambda}-(2\eta_\psi+z(d-1)-d)\right]G_n(k;w,x,\lambda)=0, \tag{E87}$$

where we have set $\kappa_i = 0$ and $\beta_{\kappa_i} = 0$. The solution to this equation is given by

$$G_n(k;w_0,x_0,\lambda_0)=\exp\left(-\mathfrak{I}_\psi(l)\right)G_n(e^l\mathbf{K},e^{\mathfrak{I}_z}\vec{k};,w(l),x(l),\lambda(l)), \tag{E88}$$

where

$$\mathfrak{I}_z(l)=\int_0^l\frac{\mathrm{d}\ell}{z(\ell)}, \tag{E89}$$

$$\mathfrak{I}_\psi(l)=\int_0^l\mathrm{d}\ell\left(\frac{2\eta_\psi(\ell)+z(\ell)(2-\epsilon)-(3-\epsilon)}{z(\ell)}\right), \tag{E90}$$

and $w(l), x(l), \lambda(l)$ are solutions to $\frac{\mathrm{d}w(l)}{\mathrm{d}l} = -\frac{\beta_w}{z(l)}$, $\frac{\mathrm{d}\lambda(l)}{\mathrm{d}l} = -\frac{\beta_\lambda}{z(l)}$, $\frac{\mathrm{d}x(l)}{\mathrm{d}l} = -\frac{\beta_x}{z(l)}$ with initial conditions, $w(0) = w_0, \lambda(0) = \lambda_0, x(0) = x_0$. Because all three parameters flow, the full crossover structure is rather complicated. However, w decays at the slowest rate,

$$w(l)\overset{l\gg1}{=}\frac{N_cN_f}{2^{\frac{11}{3}}(h_5^*)^{\frac{1}{3}}(N_c^2-1)^{\frac{2}{3}}}\frac{1}{\epsilon}\frac{1}{l^{\frac{2}{3}}}, \tag{E91}$$

and the crossover at low energies is dominated by the flow of w. To the leading order in w and ϵ,

$$z-1=\frac{(N_c^2-1)\epsilon}{2N_cN_f}w-\frac{32\sqrt{2}\sqrt{h_5^*}(N_c^2-1)\epsilon^{\frac{3}{2}}}{N_c^{\frac{3}{2}}N_f^{\frac{3}{2}}}w^{\frac{3}{2}}, \tag{E92}$$

$$\eta_\psi=-\frac{(N_c^2-1)\epsilon(2-\epsilon)}{4N_cN_f}w+\frac{8\sqrt{2}\sqrt{h_5^*}(N_c^2-1)(5-2\epsilon)\epsilon^{\frac{3}{2}}}{N_c^{\frac{3}{2}}N_f^{\frac{3}{2}}}w^{\frac{3}{2}}. \tag{E93}$$

Although w flows to zero in the low energy limit, the slow decay of w renormalizes the scaling of the frequency and the field at intermediate energy scales as $\mathfrak{I}_z(l)=\int_0^l\mathrm{d}\ell\left(1-\frac{(N_c^2-1)\epsilon}{2N_cN_f}w(\ell)\right)=$

$l-\frac{3(N_c^2-1)^{\frac{1}{3}}}{2^{\frac{14}{3}}(h_5^*)^{\frac{1}{3}}}l^{\frac{1}{3}}$, $\mathfrak{I}_\psi(l)=-\mathfrak{I}_z(l)+\frac{16\sqrt{2}\sqrt{h_5^*}(N_c^2-1)\epsilon^{\frac{3}{2}}}{N_c^{\frac{3}{2}}N_f^{\frac{3}{2}}}\int_0^l \mathrm{d}\ell\, w(\ell)^{\frac{3}{2}}=-\mathfrak{I}_z(l)+\frac{1}{2}\log(l)$. Using the fact that the fermion Green's function reduces to the bare one in the small $w(l)$ limit, we obtain the scaling form of the Green's function for $n=1$ in the low energy limit with $e^{\mathfrak{I}_z(\log(1/|\mathbf{K}|))}\vec{k}\sim 1$,

$$G_1(\mathbf{K},\vec{k})=\frac{1}{iF_\psi(|\mathbf{K}|)}\frac{1}{F_z(|\mathbf{K}|)\mathbf{\Gamma}\cdot\mathbf{K}+\gamma_{d-1}\left[\frac{\pi N_cN_f}{4\epsilon(N_c^2-1)}\frac{k_x}{\log(1/|\mathbf{K}|)}+k_y\right]}, \tag{E94}$$

where

$$v(l)=w(l)^{\frac{3}{2}}\sqrt{\frac{\lambda(l)}{x(l)}}\approx\frac{\pi N_cN_f}{4(N_c^2-1)}\frac{1}{\epsilon}\frac{1}{l} \tag{E95}$$

and $F_z(|\mathbf{K}|)$, $F_\psi(|\mathbf{K}|)$ are given by Eqs. (23) and (24), respectively.

The Green's function for the boson satisfies the renormalization group equation[43],

$$\left[z\mathbf{Q}\cdot\frac{\partial}{\partial\mathbf{Q}}+\vec{q}\cdot\frac{\partial}{\partial\vec{q}}-\beta_w\frac{\partial}{\partial w}-\beta_x\frac{\partial}{\partial x}-\beta_\lambda\frac{\partial}{\partial\lambda}-(2\eta_\phi+z(d-1)-(d+1))\right]D(q;w,x,\lambda)=0, \tag{E96}$$

which is solved by

$$D(q;w_0,x_0,\lambda_0)=\exp\left(-\mathfrak{I}_\phi(l)\right)D(e^l\mathbf{Q},e^{\mathfrak{I}_z(l)}\vec{q};w(l),x(l),\lambda(l)). \tag{E97}$$

Here $\mathfrak{I}_z(l)$ is defined in Eq. (E89) and

$$\mathfrak{I}_\phi(l)=\int_0^l \mathrm{d}\ell\left(\frac{2\eta_\phi(\ell)+z(\ell)(2-\epsilon)-(4-\epsilon)}{z(\ell)}\right), \tag{E98}$$

with

$$\eta_\phi=\frac{\epsilon}{2}+\frac{((N_c^2-1)(\epsilon-4)+4)\epsilon}{4N_cN_f}w+\frac{16\sqrt{2}\sqrt{h_5^*}(N_c^2-1)(4-\epsilon)\epsilon^{\frac{3}{2}}}{N_c^{\frac{3}{2}}N_f^{\frac{3}{2}}}w^{\frac{3}{2}}. \tag{E99}$$

From $\mathfrak{I}_\phi(l)=-2\mathfrak{I}_z(l)+\int_0^l \mathrm{d}\ell\left(\epsilon-\frac{(N_c^2-3)\epsilon}{N_cN_f}w(l)\right)=-2\mathfrak{I}_z(l)+\epsilon l-\frac{3(N_c^2-3)}{2^{\frac{11}{3}}(h_5^*)^{\frac{1}{3}}(N_c^2-1)^{\frac{2}{3}}}l^{\frac{1}{3}}$, the scaling form of the boson propagator is obtained to be

$$D(q;w_0,x_0,\lambda_0)=\exp\left(2\mathfrak{I}_z(l)-\epsilon l+\frac{3(N_c^2-3)}{2^{\frac{11}{3}}(h_5^*)^{\frac{1}{3}}(N_c^2-1)^{\frac{2}{3}}}l^{\frac{1}{3}}\right)D(e^l\mathbf{Q},e^{\mathfrak{I}_z(l)}\vec{q};w(l),x(l),\lambda(l)), \tag{E100}$$

where $l=\log(1/|\mathbf{Q}|)$ with $e^{\mathfrak{I}_z(l)}\vec{q}\sim 1$.

Appendix B

Appendix to Chapter 3

I Proof of the upper bound for general diagrams

In this section, we prove the upper bound in Eq. (34), assuming that the fully dressed boson propagator is given by Eqs. (32) and (33) in the small v limit. Since the boson propagator is already fully dressed, we do not need to consider boson self-energy corrections within diagrams. The magnitude of a diagram is not simply determined by the number of vertices because in the small v limit patches of the Fermi surface become locally nested, and the collective mode loses its dispersion. When a loop is formed out of dispersionless bosons and nested fermions, the loop momentum along the Fermi surface becomes unbounded. For small but nonzero v and c, the divergent integral is cut off by a scale which is proportional to $1/v$ or $1/c$. This gives rise to enhancement factors of $1/v$ or $1/c$. Our goal is to compute the upper bound of the enhancement factors for general diagrams. A diagram is maximally enhanced when all the patches of the Fermi surface involved in the diagram are nested. Since the patches are nested pairwise $(1, 3$ and $2, 4)$ in the small v limit, it is enough to consider diagrams that are made of patches $1, 3$ to compute the upper bound without loss of generality. Diagrams which involve all four patches are generally smaller in magnitude than those that involve only $1, 3$ or $2, 4$ for fixed L, L_f, E, where L is the total number of loops, L_f is the number of fermion loops and E is the number of external legs. We first show that Eq. (34) holds for an example to illustrate the idea that is used for a general proof in the following subsection.

I-1 Example

The diagram in Figure B.1(a) is a fermion self-energy with one fermion loop and three other loops, which we call 'mixed loops'. For simplicity, we set the external momentum to zero. This does not affect the enhancement factors of $1/c$ and $1/v$ which originate from large internal

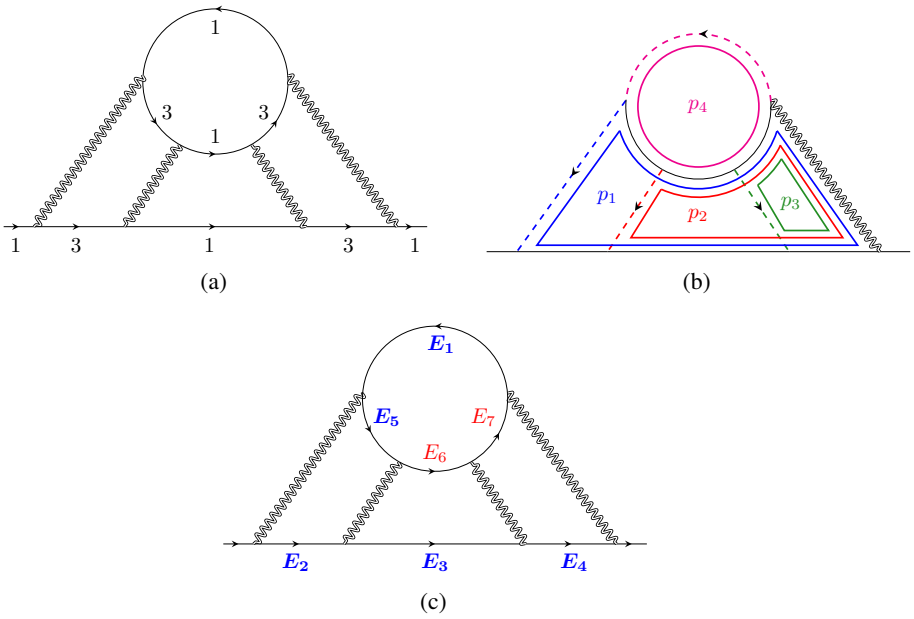

Figure A1: (a) A four-loop diagram with one fermion loop. The numbers next to the fermion lines represent the patch indices. (b) The four exclusive propagators are denoted as dashed lines. The remaining propagators represent the connected tree diagram. Loops (thick solid colored lines) are chosen such that each loop momentum goes through only one of the exclusive propagators. (c) The seven internal fermion propagators whose energies are denoted as E_l with $1 \leq l \leq 7$. $E_1, E_2, .., E_5$ are used as new integration variables along with $p_i^{'} = cp_{i,x}$ with $i = 1, 2, 3$, as discussed in the text.

momenta. We label the loop momenta as shown in Figure B.1(b). With this choice, each mixed loop momentum p_i with $i = 1, 2, 3$ has a boson line that carries only p_i, and the fermion loop momentum p_4 has a fermion line that carries only p_4. These four propagators, denoted in Figure B.1(b) by dashed lines, are called 'exclusive propagators'. In the next section we show that it is always possible to find such exclusive propagators for every loop momentum in a general diagram. The diagram in Figure B.1(a) is written as

$$
\begin{aligned}
I \;\sim\; & v^4 \int \prod_{r=1}^{4} dp_r \left(\prod_{j=1}^{3} \frac{1}{|p_{j,0}| + c(|p_{j,x}| + |p_{j,y}|)} \right) \times \\
& \frac{1}{|p_{1,0} + p_{2,0} + p_{3,0}| + c(|p_{1,x} + p_{2,x} + p_{3,x}| + |p_{1,y} + p_{2,y} + p_{3,y}|)} \times \\
& \frac{1}{ip_{4,0} + E_1} \; \frac{1}{ip_{1,0} + E_2} \; \frac{1}{i\,(p_{1,0} + p_{2,0}) + E_3} \; \frac{1}{i\,(p_{1,0} + p_{2,0} + p_{3,0}) + E_4} \times \\
& \frac{1}{i(p_{4,0} - p_{1,0}) + E_5} \; \frac{1}{i(p_{4,0} - p_{1,0} - p_{2,0}) + E_6} \; \frac{1}{i(p_{4,0} - p_{1,0} - p_{2,0} - p_{3,0}) + E_7},
\end{aligned}
$$

where p_r is the set of internal three-momenta, and E_i represents the energy of the fermion in the i-th fermion propagator as denoted in Figure B.1(c),

$$
E_1 \;=\; v p_{4,x} + p_{4,y},
$$

$$
\begin{aligned}
E_2 &= vp_{1,x} - p_{1,y}, \\
E_3 &= v(p_{1,x} + p_{2,x}) + (p_{1,y} + p_{2,y}), \\
E_4 &= v(p_{1,x} + p_{2,x} + p_{3,x}) - (p_{1,y} + p_{2,y} + p_{3,y}), \\
E_5 &= v(-p_{1,x} + p_{4,x}) - (-p_{1,y} + p_{4,y}), \\
E_6 &= v(-p_{1,x} - p_{2,x} + p_{4,x}) + (-p_{1,y} - p_{2,y} + p_{4,y}), \\
E_7 &= v(-p_{1,x} - p_{2,x} - p_{3,x} + p_{4,x}) - (-p_{1,y} - p_{2,y} - p_{3,y} + p_{4,y}).
\end{aligned} \tag{A101}
$$

Since frequency integrations are not affected by v and c, we focus on the spatial components of momenta from now on. Our aim is to change the variables for the internal momenta so that the enhancement factors of $1/v$ and $1/c$ become manifest. As our first three new variables we choose $p_j^{'} \equiv cp_{j,x}$ with $1 \leq j \leq 3$. The last five variables are chosen to be $p_{l+3}^{'} \equiv E_l$ with $1 \leq l \leq 5$. The transformation between the old variables, written as $\{vp_{i,x}, p_{i,y}\}$, and the new variables is given by

$$
\begin{pmatrix} p_1^{'} \\ p_2^{'} \\ \vdots \\ p_8^{'} \end{pmatrix} = \begin{pmatrix} \frac{c}{v}\mathbb{I}_3 & 0 \\ \tilde{\mathbb{A}} & \tilde{\mathbb{V}} \end{pmatrix} \begin{pmatrix} vp_{1,x} \\ vp_{2,x} \\ vp_{3,x} \\ vp_{4,x} \\ p_{1,y} \\ p_{2,y} \\ p_{3,y} \\ p_{4,y} \end{pmatrix}, \tag{A102}
$$

where $\tilde{\mathbb{A}}$ and $\tilde{\mathbb{V}}$ are written as

$$
\tilde{\mathbb{A}} = \begin{pmatrix} 0 & 0 & 0 \\ 1 & 0 & 0 \\ 1 & 1 & 0 \\ 1 & 1 & 1 \\ -1 & 0 & 0 \end{pmatrix}, \quad \tilde{\mathbb{V}} = \begin{pmatrix} 1 & 0 & 0 & 0 & 1 \\ 0 & -1 & 0 & 0 & 0 \\ 0 & 1 & 1 & 0 & 0 \\ 0 & -1 & -1 & -1 & 0 \\ 1 & 1 & 0 & 0 & -1 \end{pmatrix}, \tag{A103}
$$

and $\mathbb{I}_3$ is the 3×3 identity matrix. For non-zero v, c, the change of variables is non-degenerate, and the Jacobian of the transformation is $(2c^3v)^{-1}$. We show in the following section that such a non-degenerate choice is always possible for general diagrams. An easy mnemonic is that each fermion loop contributes a factor of $1/v$ because of nesting in the small v limit, while each mixed loop contributes a factor of $1/c$ because of the vanishing boson velocity.

In the new coordinates, the momentum integration in Eq. (A101) becomes

$$I \sim \frac{v^3}{c^3}\int\prod_{i=1}^{8}dp_i^{'}\left(\prod_{j=1}^{3}\frac{1}{|p_j^{'}|+O(c)}\right)\left(\prod_{l=4}^{8}\frac{1}{p_l^{'}}\right)\tilde{R}[p^{'}], \tag{A104}$$

where $\tilde{R}[p^{'}]$ includes the propagators that are not explicitly shown. Now, we can safely take the small c limit inside the integrand, because every momentum component has at least one propagator which guarantees that the integrand decays at least as $1/p_j^{'}$ in the large momentum limit. Therefore, the integrations are UV convergent up to potential logarithmic divergences. To leading order in small v, the diagram scales as

$$I \sim \left(\frac{v}{c}\right)^3 \sim v^{\frac{3}{2}}$$

up to potential logarithmic corrections.

I-2 General upper bound

Here we provide a general proof for the upper bound, by generalizing the example discussed in the previous section. We consider a general L-loop diagram that includes fermions from patches $1, 3$,

$$I \sim v^{\frac{V}{2}}\int\prod_{r=1}^{L}dp_r\left(\prod_{l=1}^{I_f}\frac{1}{ik_{l,0}+vk_{l,x}+(-1)^{\frac{n_l-1}{2}}k_{l,y}}\right)\left(\prod_{m=1}^{I_b}\frac{1}{|q_{m,0}|+c(|q_{m,x}|+|q_{m,y}|)}\right) \tag{A105}$$

Here V is the number of vertices. I_f, I_b are the numbers of internal fermion and boson propagators, respectively. p_r is the set of internal three-momenta. k_l (q_m) represents the momentum that flows through the l-th fermion (m-th boson) propagator. These are linear combinations of the internal momenta and external momenta. The way k_l, q_m depend on p_r is determined by how we choose internal loops within a diagram. $n_l = 1, 3$ is the patch index for the l-th fermion propagator. Since the frequency integrations are not affected by v and c, we focus on the spatial components of momenta from now on.

It is convenient to choose loops in such a way that there exists a propagator exclusively assigned to each internal momentum. For this, we follow the procedure given in Sec. VI of [69]. For a given diagram, we cut internal propagators one by one. We continue cutting until all loops disappear while the diagram remains connected. First, we cut one fermion propagator in every fermion loop, which requires cutting L_f fermion lines. The remaining $L_m \equiv L - L_f$ loops, which we call mixed loops, can be removed by cutting boson propagators. After cutting L lines in total, we are left with a connected tree diagram. Now we glue the propagators back one by one to restore the original L-loop diagram. Every time we glue one propagator, we assign one internal momentum such that it goes through the propagator that is just glued back and the

connected tree diagram only. This guarantees that the propagator depends only on the internal momentum which is associated with the loop that is just formed by gluing. In gluing L_f fermion propagators, the associated internal momenta go through the fermion loops. The L_m mixed loops necessarily include both fermion and boson propagators. After all propagators are glued back, L internal momenta are assigned in such a way that for every loop momentum there is one exclusive propagator.

With this choice of loops, Eq. (A105) is written as

$$I \sim v^{\frac{V}{2}} \int \prod_{r=1}^{L} dp_{r,x} dp_{r,y} \left(\prod_{j=1}^{L_m} \frac{1}{c|p_{j,x}| + c|p_{j,y}|} \right) \left(\prod_{l=1}^{I_f} \frac{1}{E_l(p)} \right) R[p]. \quad \text{(A106)}$$

Here, frequency is suppressed, and IR divergences in the integrations over spatial momenta are understood to be cut off by frequencies. Our focus is on the UV divergence that arises in the spatial momentum integrations in the limit of small v and c. The first group in the integrand represents the exclusive boson propagators assigned to the L_m mixed loops. Each of the L_m boson propagators depends on only one internal momentum due to the exclusive nature of our choice of loops. The second group represents all fermion propagators. $E_l(p)$ is the energy of the fermion in the l-th fermion propagator which is given by a linear superposition of $p_{r,x}, p_{r,y}$. $R[p]$ represents the rest of the boson propagators that are not assigned as exclusive propagators.

Our strategy is to find a new basis for the loop momenta such that the divergences in the small v and c limit become manifest. The first L_m variables are chosen to be $cp_{j,x}$ with $j = 1, 2, .., L_m$ while the remaining $2L - L_m$ variables are chosen among $\{E_l(p)\}$. This is possible because $I_f \geq (2L - L_m)$ for diagrams with $E > 0$. We express $p_j^{'} \equiv cp_{j,x}$ and $E_l(p)$ in terms of $vp_{r,x}, p_{r,y}$,

$$\begin{pmatrix} p_1^{'} \\ p_2^{'} \\ \vdots \\ p_{L_m}^{'} \\ E_1 \\ E_2 \\ \vdots \\ E_{I_f} \end{pmatrix} = \begin{pmatrix} \frac{c}{v}\mathbb{I}_{L_m} & 0 \\ \mathbb{A} & \mathbb{V} \end{pmatrix} \begin{pmatrix} vp_{1,x} \\ vp_{2,x} \\ \vdots \\ vp_{L_m,x} \\ vp_{L_m+1,x} \\ \vdots \\ vp_{L,x} \\ p_{1,y} \\ p_{2,y} \\ \vdots \\ p_{L,y} \end{pmatrix}. \quad \text{(A107)}$$

Here $\mathbb{I}_a$ is the $a \times a$ identity matrix. $A_{l,j} = \frac{1}{v}\frac{\partial E_l}{\partial p_{j,x}}$ with $1 \leq l \leq I_f$, $1 \leq j \leq L_m$. $\mathbb{V}$ is an $I_f \times (2L - L_m)$ matrix whose first $L - L_m$ columns are given by $V_{l,i-L_m} = \frac{1}{v}\frac{\partial E_l}{\partial p_{i,x}}$

with $L_m + 1 \leq i \leq L$ and the remaining L columns are given by $V_{l,i+(L-L_m)} = \frac{\partial E_l}{\partial p_{i,y}}$ with $1 \leq i \leq L$. Now we focus on the lower-right corner of the transformation matrix which governs the relation between $\vec{E}^T \equiv (E_1, E_2, .., E_{I_f})$ and $\vec{P}^T \equiv (vp_{L_m+1,x}, .., vp_{L,x}, p_{1,y}, .., p_{L,y})$ when $p_{j,x} = 0$ for $1 \leq j \leq L_m$,

$$\vec{E} = \mathbb{V}\vec{P}. \tag{A108}$$

$\vec{P}$ represents the x, y components of momenta in the fermion loops and the y components of momenta in the mixed loops. The matrix $\mathbb{V}$ can be viewed as a collection of $2L - L_m$ column vectors, each of which have I_f components. We first show that the $2L - L_m$ column vectors are linearly independent.

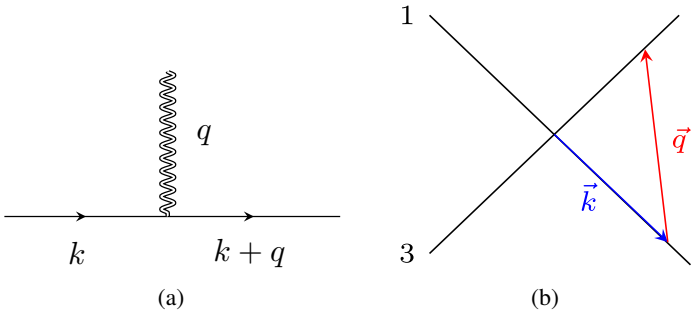

Figure A2: For a boson momentum $\vec{q}$, there exists a unique $\vec{k}$ such that $\varepsilon_1(\vec{k}) = \varepsilon_3(\vec{k} + \vec{q}) = 0$ for $v \neq 0$.

If the column vectors were not linearly independent, there would exist a nonzero $\vec{P}$ such that $\mathbb{V}\vec{P} = 0$. This implies that there exists at least a one-parameter family of x, y-momenta in the L_f fermion loops and y-momenta in the L_m mixed loops such that all internal fermions lie on the Fermi surface. However, this is impossible for the following reason. For $v \neq 0$, a momentum on an external boson leg uniquely fixes the internal momenta on the two fermion lines attached to the boson line if both fermions are required to have zero energy. This is illustrated in Figure A2. Similarly, a momentum on an external fermion leg fixes the momenta on the adjacent internal fermion and boson lines if the internal fermion is required to have zero energy and only the y component of momentum is allowed to vary in the mixed loops. Once the momenta on the internal lines attached to the external lines are fixed, those internal lines in turn fix the momenta of other adjoining internal lines. As a result, all internal momenta are successively fixed by external momenta if we require that $E_l = 0$ for all l. Therefore, there cannot be a non-trivial $\vec{P}$ that satisfies $\mathbb{V}\vec{P} = 0$. This implies that the column vectors in $\mathbb{V}$ must be linearly independent.

Since $\mathbb{V}$ is made of $(2L - L_m)$ independent column vectors, it necessarily includes $(2L - L_m)$ independent row vectors. Let the l_k-th rows with $k = 1, 2, .., (2L - L_m)$ be the set of rows that are linearly independent, and $\tilde{\mathbb{V}}$ be a $(2L - L_m) \times (2L - L_m)$ invertible matrix made of these rows. We choose $p'_{L_m+k} \equiv E_{l_k}$ with $k = 1, 2, .., (2L - L_m)$ as the remaining $(2L - L_m)$ integration variables. The transformation between the original $2L$ momentum variables and the

new variables is given by

$$\begin{pmatrix} p_1^{'} \\ p_2^{'} \\ \vdots \\ p_{2L}^{'} \end{pmatrix} = \begin{pmatrix} \frac{c}{v}\mathbb{I}_{L_m} & 0 \\ \tilde{\mathbb{A}} & \tilde{\mathbb{V}} \end{pmatrix} \begin{pmatrix} vp_{1,x} \\ vp_{2,x} \\ \vdots \\ vp_{L,x} \\ p_{1,y} \\ p_{2,y} \\ \vdots \\ p_{L,y} \end{pmatrix}, \tag{A109}$$

where $\tilde{\mathbb{A}}$ is a $(2L - L_m) \times L_m$ matrix made of the collection of the l_k-th rows of $\mathbb{A}$ with $k = 1, 2, .., (2L - L_m)$. The Jacobian of the transformation is given by $Y^{-1}c^{-L_m}v^{-L_f}$. Here, $Y = |\det \tilde{\mathbb{V}}|$ is a constant independent of v and c, which is nonzero because $\tilde{\mathbb{V}}$ is invertible.

In the new variables, Eq. (A106) becomes

$$I \sim v^{\frac{V}{2}-L_f} c^{-L_m} \int \prod_{i=1}^{2L} dp_i^{'} \left(\prod_{j=1}^{L_m} \frac{1}{|p_j^{'}| + O(c)} \right) \left(\prod_{l=L_m+1}^{2L} \frac{1}{p_l^{'}} \right) \tilde{R}[p^{'}]. \tag{A110}$$

Every component of the loop momenta has at least one propagator which guarantees that the integrand decays at least as $1/p_l^{'}$ in the large momentum limit. $\tilde{R}[p^{'}]$ is the product of all remaining propagators. Therefore, the integrations over the new variables are convergent up to potentially logarithmic divergences. Using $L = \frac{1}{2}(V + 2 - E)$, one can see that a general diagram is bounded by

$$I \sim v^{\frac{E-2}{2}} \left(\frac{v}{c}\right)^{L-L_f} \tag{A111}$$

up to logarithmic corrections. Diagrams with large $(L - L_f)$ are systematically suppressed for $v \ll c$. This bound can be checked explicitly for individual diagrams.

II Derivation of the self-consistent boson self-energy

In this section, we derive Eqs. (32) and (33) from Eq. (35).

The one-loop quantum effective action of the boson generated from Fig. 3.2(a) is written as

$$\Gamma^{1L}_{(0,2)} = \frac{1}{4} \int dq \, \Pi^{1L}(q) \, \mathrm{Tr}\left[\Phi(-q)\Phi(q)\right], \tag{B112}$$

where

$$\Pi^{1L}(q) = -\pi v \sum_{n=1}^{4} \int dk \, \mathrm{Tr}\left[\gamma_1 G_n^{(0)}(k)\gamma_1 G_{\bar{n}}^{(0)}(k+q)\right] \tag{B113}$$

and the bare fermion propagator is $G_n^{(0)}(k) = -i\frac{k_0\gamma_0+\varepsilon_n(\vec{k})\gamma_1}{k_0^2+\varepsilon_n^2(\vec{k})}$ and $dk \equiv \frac{d^3k}{(2\pi)^3}$. The integration of the spatial momentum gives $\Pi^{1L}(q) = -\frac{1}{2}\int dk_0 \frac{(k_0+q_0)k_0}{|k_0+q_0||k_0|}$. The k_0 integration generates a linearly divergent mass renormalization which is removed by a counter term, and a finite self-energy,

$$\Pi^{1L} = |q_0|. \tag{B114}$$

Since the one-loop self-energy depends only on frequency, we have to include higher-loop diagrams to generate a momentum-dependent quantum effective action, even though they are suppressed by powers of v compared to the one-loop self-energy. According to Eq. (34), the next leading diagrams are the ones with $L - L_f = 1$. Among the diagrams with $L - L_f = 1$, the only one that contributes to the momentum-dependent boson self-energy is shown in Figure 3.2(b). In particular, other two-loop diagrams that include fermion self-energy insertions do not contribute. Since the two-loop diagram itself depends on the unknown dressed boson propagator, we need to solve the self-consistent equation for $D(q)$ in Eq. (35). Here, we first assume that the solution takes the form of Eq. (32) with $v \ll c \ll 1$ to compute the two-loop contribution, and show that the resulting boson propagator agrees with the assumed one. The two-loop self-energy reads

$$\begin{aligned}\Pi^{2L}(q) = -\frac{\pi^2 v^2}{2}\sum_{n=1}^{4}\int \mathrm{d}k\mathrm{d}p \Bigg[&\frac{1}{\left(k_0+p_0-i\varepsilon_n(\vec{k}+\vec{p})\right)\left(k_0-i\varepsilon_{\bar{n}}(\vec{k})\right)} \\ \times&\frac{1}{\left(k_0+q_0-i\varepsilon_n(\vec{k}+\vec{q})\right)\left(k_0+p_0+q_0-i\varepsilon_{\bar{n}}(\vec{k}+\vec{p}+\vec{q})\right)}\Bigg] D(p) + \text{c.c.}.\end{aligned} \tag{B115}$$

Here c.c. denotes the complex conjugate. Straightforward integrations over $\vec{k}$ and k_0 give

$$\Pi^{2L}(q_0,\vec{q}) = -\frac{\pi v}{8}\sum_{n=1}^{4}\int \mathrm{d}p \left[\frac{|q_0|-|p_0|}{((p_0+q_0)-i\varepsilon_{\bar{n}}(\vec{p}+\vec{q}))((q_0-p_0)-i\varepsilon_n(\vec{q}-\vec{p}))}\right] D(p) + \text{c.c.}. \tag{B116}$$

Since the frequency-dependent self-energy is already generated from the lower order one-loop graph in Figure 3.2(a), we focus on the momentum-dependent part. This allows us to set the

external frequency to zero to rewrite Eq. (B116) as

$$\Pi^{2L}(0,\vec{q}) = \frac{\pi v}{4}\sum_{n=1}^{4}\int \mathrm{d}p \left[\frac{|p_0|}{(ip_0+\varepsilon_{\bar{n}}(\vec{p}+\vec{q}))(ip_0+\varepsilon_n(\vec{p}-\vec{q}))}\right] D(p). \tag{B117}$$

After subtracting the linearly divergent mass renormalization, $\Delta\Pi^{2L}(0,\vec{q}) \equiv \Pi^{2L}(0,\vec{q}) - \Pi^{2L}(0,0)$ is UV finite,

$$\Delta\Pi^{2L}(0,\vec{q}) = \frac{\pi v}{4}\sum_{n=1}^{4}\int \mathrm{d}p \frac{|p_0|\mathcal{F}^{1L(n)}(p_0,\vec{p},\vec{q};v)}{(p_0^2+\varepsilon_{\bar{n}}^2(\vec{p}+\vec{q}))(p_0^2+\varepsilon_n^2(\vec{p}-\vec{q}))(p_0^2+\varepsilon_{\bar{n}}^2(\vec{p}))(p_0^2+\varepsilon_n^2(\vec{p}))} D(p), \tag{B118}$$

where

$$\begin{aligned}\mathcal{F}^{1L(n)}(p_0,\vec{p},\vec{q};v) = {} & (p_0^2+\varepsilon_n^2(\vec{p}))(p_0^2+\varepsilon_{\bar{n}}^2(\vec{p}))(ip_0-\varepsilon_{\bar{n}}(\vec{p}+\vec{q}))(ip_0-\varepsilon_n(\vec{p}-\vec{q})) \\ & - (p_0^2+\varepsilon_{\bar{n}}^2(\vec{p}+\vec{q}))(p_0^2+\varepsilon_n^2(\vec{p}-\vec{q}))(ip_0-\varepsilon_{\bar{n}}(\vec{p}))(ip_0-\varepsilon_n(\vec{p})).\end{aligned} \tag{B119}$$

Now we consider the contribution of each hot spot separately. For $n=1$, the dependence on q_x is suppressed by v compared to the q_y-dependent self-energy. Therefore, we set $q_x = 0$ for small v. Furthermore, the p_y dependence in $D(p)$ can be safely dropped in the small c limit because $\varepsilon_1(\vec{p})$ and $\varepsilon_3(\vec{p})$ suppress the contributions from large p_y. Rescaling the momentum as $(p_0,p_x,p_y) \to |q_y|(p_0,p_x/c,p_y)$ followed by the integration over p_y, we obtain the contribution from the hot spot $n=1$,

$$\Delta\Pi^{2L}(0,\vec{q}) = \frac{v}{32\pi c}|q_y|\int \mathrm{d}p_0\mathrm{d}p_x \frac{(1+p_0^2-3p_x^2w^2)p_0^2}{(p_0^2+w^2p_x^2)(p_0^2+(wp_x-1)^2)(p_0^2+(wp_x+1)^2)}\frac{1}{|p_0|+|p_x|}, \tag{B120}$$

where $w \equiv v/c$. In the integrand, we can not set $w=0$ because the integration over p_x is logarithmically divergent in the small w limit,

$$\Delta\Pi^{2L(1)}(0,\vec{q}) = \frac{v}{32\pi c}|q_y|\int \mathrm{d}p_0 \frac{1}{1+p_0^2}\left[-2\log(w) - 2p_0\cot^{-1}(p_0) + p_0^2\log\left(\frac{p_0^2}{1+p_0^2}\right) + O(w)\right]. \tag{B121}$$

Finally, the integration over p_0 gives

$$\Delta\Pi^{2L(1)}(0,\vec{q}) = \frac{|q_y|v}{16c}\left[\log\left(\frac{1}{w}\right) - 1 + O(w)\right]. \tag{B122}$$

In the small w limit, the first term dominates. Hot spot 3 generates the same term, and the contribution from hot spots $2,4$ is obtained by replacing q_y with q_x. Summing over contributions

energy	scaling	dynamical critical exponent
$q_0 > \tilde{\Lambda}$	$q_0 \sim c_0 q$	$z = 1$
$\frac{c^2}{c_0^2}\tilde{\Lambda} < q_0 < \tilde{\Lambda}$	$q_0 \sim c_0^2 q^2/\tilde{\Lambda}$	$z = 2$
$q_0 < \frac{c^2}{c_0^2}\tilde{\Lambda}$	$q_0 \sim cq$	$z = 1$

TABLE B1: The energy dependent dynamical critical exponent for $c_0 > c$.

energy	scaling	dynamical critical exponent
$q_0 > \frac{c}{c_0}\tilde{\Lambda}$	$q_0 \sim c_0 q$	$z = 1$
$\tilde{\Lambda} < q_0 < \frac{c}{c_0}\tilde{\Lambda}$	$q_0 \sim \sqrt{c\tilde{\Lambda} q}$	$z = \frac{1}{2}$
$q_0 < \tilde{\Lambda}$	$q_0 \sim cq$	$z = 1$

TABLE B2: The energy dependent dynamical critical exponent for $c_0 < c$.

from all the hot spots, we obtain

$$\Delta\Pi^{2L}(0,\vec{q}) = \frac{v}{8c}\log\left(\frac{c}{v}\right)(|q_x| + |q_y|) + O\left(\frac{1}{vc}\right). \tag{B123}$$

The two-loop diagram indeed reproduces the assumed form of the self-energy which is proportional to $|q_x| + |q_y|$ to the leading order in v. The full Schwinger-Dyson equation now boils down to a self-consistent equation for the boson velocity,

$$c = \frac{v}{8c}\log\left(\frac{c}{v}\right). \tag{B124}$$

c is solved in terms of v as

$$c(v) = \frac{1}{4}\sqrt{v\log\left(\frac{1}{v}\right)}\left(1 + O\left(\frac{\log\log(1/v)}{\log(1/v)}\right)\right). \tag{B125}$$

This is consistent with the assumption that $v \ll c \ll 1$ in the small v limit.

The full propagator of the boson which includes the bare kinetic term in Eq. (27) is given by

$$D(q)^{-1} = |q_0| + c(|q_x| + |q_y|) + \frac{q_0^2}{\tilde{\Lambda}} + \frac{c_0^2}{\tilde{\Lambda}}|\vec{q}|^2, \tag{B126}$$

where $\tilde{\Lambda}$ is a UV scale associated with the coupling. Depending on the ratio between c and c_0, which is determined by microscopic details, one can have different sets of crossovers.

For $c_0 > c$, one has a series of crossovers from the Gaussian scaling with $z = 1$ at high energies, to the scaling with $z = 2$ at intermediate energies and to the non-Fermi liquid scaling with $z = 1$ at low energies. In the low energy limit, the system eventually becomes superconducting. For $c_0 < c$, on the other hand, the $z = 2$ scaling is replaced with a scaling with $z = \frac{1}{2}$ at intermediate energies. This is summarized in Tables B1 and B2.

III Derivation of the beta function for v

In this section, we derive the beta function for v in Eq. (**??**). We first compute the counter terms that need to be added to the local action such that the quantum effective action is independent of the UV cut-off scale to the lowest order in v. Then we derive the beta function for v and its solution, which confirms that v flows to zero in the low-energy limit.

III-1 Frequency-dependent fermion self-energy

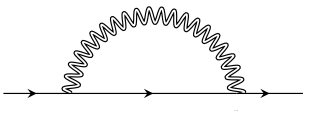

Figure C3: The one-loop diagram for the fermion self-energy.

According to Eq. (34), the leading order fermion self-energy is generated from Fig. C3 in the small v limit. The one-loop fermion self-energy for patch n is given by

$$\Sigma^{1L(n)}(k_0,\vec{k}) = \frac{3\pi v}{2}\int dp\,\gamma_1 G^{(0)}_{\bar{n}}(p+k)\gamma_1 D(p), \tag{C127}$$

where the dressed boson propagator is $D(p) = \frac{1}{|p_0|+c(v)(|p_x|+|p_y|)}$. We first compute $\Sigma^{1L(n)}(k)$ for $n = 1$. The quantum correction is logarithmically divergent, and a UV cut-off Λ is imposed on p_y, which is the momentum perpendicular to the Fermi surface for $n = 1$ in the small v limit. However, the logarithmically divergent term is independent of how UV cut-off is implemented. To extract the frequency-dependent self-energy, we set $\vec{k} = 0$ and rescale $(p_0,p_x,p_y) \to |k_0|(p_0,p_x/c,p_y)$ to rewrite

$$\Sigma^{1L(1)}(k_0,0) = i\gamma_0 k_0 \frac{3\pi v}{2c}\int dp\,\frac{p_0+1}{[(p_0+1)^2+(wp_x-p_y)^2]\,[|p_0|+|p_x|+c|p_y|]}, \tag{C128}$$

where $w = \frac{v}{c}$. Under this rescaling, the UV cut-off for p_y is also rescaled to $\Lambda_0 = \Lambda/|k_0|$. The p_0 integration gives

$$\begin{aligned}\Sigma^{1L(1)}(k_0,0) = i\gamma_0 k_0 \tfrac{3\pi v}{2(2\pi)^3 c}\int_{-\Lambda_0}^{\Lambda_0} dp_y \int dp_x \\ \Big[\tfrac{\pi}{2}|p_y-wp_x|\left(\tfrac{1}{(p_y-wp_x)^2+(-1+|p_x|+c|p_y|)^2}-\tfrac{1}{(p_y-wp_x)^2+(1+|p_x|+c|p_y|)^2}\right) \\ -(p_y-wp_x)\,\mathrm{arccot}(p_y-wp_x)\left(\tfrac{1}{(p_y-wp_x)^2+(-1+|p_x|+c|p_y|)^2}+\tfrac{1}{(p_y-wp_x)^2+(1+|p_x|+c|p_y|)^2}\right) \\ +\tfrac{1}{2}\log\left(\tfrac{1+(p_y-wp_x)^2}{(|p_x|+c|p_y|)^2}\right)\left(\tfrac{1+|p_x|+c|p_y|}{(p_y-wp_x)^2+(1+|p_x|+c|p_y|)^2}-\tfrac{-1+|p_x|+c|p_y|}{(p_y-wp_x)^2+(-1+|p_x|+c|p_y|)^2}\right)\Big]\end{aligned} \tag{C129}$$

The logarithmically divergent contribution is obtained to be

$$\Sigma^{1L(1)}(k_0,0) = \frac{3}{4\pi}\frac{v}{c}\log\left(\frac{\Lambda}{|k_0|}\right) i\gamma_0 k_0 \tag{C130}$$

in the small v limit. The self-energy for other patches is obtained from a series of 90-degree rotations, and the frequency-dependent part is identical for all patches. In order to remove the cut-off dependence in the quantum effective action, we add the counter term,

$$\sum_{n=1}^{4}\sum_{\sigma=\uparrow,\downarrow}\int dk\;\bar{\Psi}_{n,\sigma}(k)\left(Z_{1,1}\,i\gamma_0 k_0\right)\Psi_{n,\sigma}(k) \tag{C131}$$

with

$$Z_{1,1}=-\frac{3}{4\pi}\frac{v}{c}\,\log\left(\frac{\Lambda}{\mu}\right), \tag{C132}$$

where μ is the scale at which the quantum effective action is defined in terms of the renormalized velocity v. The counter term guarantees that the renormalized propagator at the scale μ is expressed solely in terms of v in the $\Lambda/\mu\to\infty$ limit.

III-2 Momentum-dependent fermion self-energy

To compute the momentum-dependent fermion self-energy, we start with Eq. (C127) for $n=1$ and set $k_0=0$. Rescaling $p_x\to\frac{p_x}{c}$ gives

$$\Sigma^{1L(1)}(0,\vec{k})=-\frac{3\pi v}{2c}i\gamma_1\int dp\;\frac{wp_x-p_y+\varepsilon_3(\vec{k})}{\left[p_0^2+(wp_x-p_y+\varepsilon_3(\vec{k}))^2\right]\left[|p_0|+|p_x|+c|p_y|\right]}. \tag{C133}$$

The integration over p_0 results in $\Sigma^{1L(1)}(0,\vec{k})=\Sigma^{1L(1)}(\vec{k})\Big|_{\text{term 1}}+\Sigma^{1L(1)}(\vec{k})\Big|_{\text{term 2}}$, where

$$\Sigma^{1L(1)}(\vec{k})\Big|_{\text{term 1}}=-\,i\gamma_1\frac{3\pi v}{2(2\pi)^3c}\int dp_y\int dp_x\frac{\operatorname{sgn}(wp_x-p_y+\varepsilon_3(\vec{k}))(|p_x|+c|p_y|)\pi}{(p_y-\varepsilon_3(\vec{k})-wp_x)^2+(|p_x|+c|p_y|)^2}, \tag{C134}$$

$$\Sigma^{1L(1)}(\vec{k})\Big|_{\text{term 2}}=-\,i\gamma_1\frac{3\pi v}{2(2\pi)^3c}\int dp_y\int dp_x\frac{(p_y-\varepsilon_3(\vec{k})-wp_x)\log\left(\frac{(|p_x|+c|p_y|)^2}{(p_y-\varepsilon_3(\vec{k})-wp_x)^2}\right)}{(p_y-\varepsilon_3(\vec{k})-wp_x)^2+(|p_x|+c|p_y|)^2}. \tag{C135}$$

We first compute the first term. After performing the p_x integration, we rescale $p_y\to|\varepsilon_3(\vec{k})|p_y$ to obtain

$$\begin{aligned}\Sigma^{1L(1)}(\vec{k})\Big|_{\text{term 1}}=-\tfrac{3\pi^2 v}{2(2\pi)^3c}i\gamma_1\varepsilon_3(\vec{k})\int_{-\Lambda_3}^{\Lambda_3}dp_y\Bigg[&\tfrac{\pi w}{2(1+w^2)}\left(\operatorname{sgn}\left(p_y-1+cw|p_y|\right)+\operatorname{sgn}\left(p_y-1-cw|p_y|\right)\right)\\&+\tfrac{\operatorname{sgn}(p_y-1)}{1+w^2}\left(w\arctan\left(\tfrac{w(-p_y+1)+c|p_y|}{p_y-1+cw|p_y|}\right)+w\arctan\left(\tfrac{w(p_y-1)+c|p_y|}{-p_y+1+cw|p_y|}\right)\right.\\&\left.-2w\arctan\left(w^{-1}\right)-\log\left(\tfrac{c^2w^2p_y^2+(p_y-1)^2+2cw|p_y-1||p_y|}{w^2\left(c^2p_y^2+(p_y-1)^2\right)}\right)\right)\Bigg],\end{aligned} \tag{C136}$$

where $\Lambda_3 = \frac{\Lambda}{|\varepsilon_3(\vec{k})|}$. The remaining p_y integration gives

$$\Sigma^{1L(1)}(\vec{k})\Big|_{\text{term 1}} = \frac{3v(w-c)}{4\pi} \log\left(\frac{\Lambda}{|\varepsilon_3(\vec{k})|}\right) i\gamma_1\varepsilon_3(\vec{k}) \tag{C137}$$

to the leading order in v up to terms that are finite in the large Λ limit.

The second term can be computed similarly in the small v limit,

$$\Sigma^{1L(1)}(\vec{k})\Big|_{\text{term 2}} = -\frac{3}{2\pi^2}\, v \log\left(\frac{1}{c}\right) \log\left(\frac{\Lambda}{|\varepsilon_3(\vec{k})|}\right) i\gamma_1\varepsilon_3(\vec{k}) \tag{C138}$$

up to UV-finite terms. It is noted that the second term is dominant for small v.

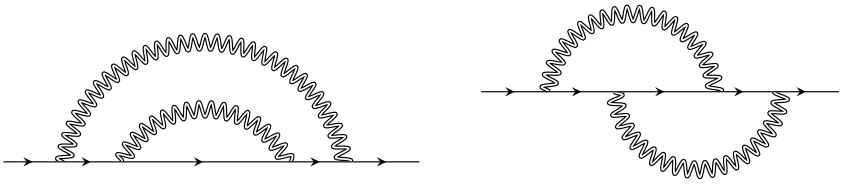

(a) (b)

Figure C4: Two-loop diagrams for the fermion self-energy. While (a) is sub-leading in the small v limit, (b) is of the same order as Figure C3.

According to Eq. (34), the upper bound for the one-loop fermion self-energy is v/c. However, Eq. (C138) is strictly smaller than the upper bound. The extra suppression by c arises due to the fact that the external momentum in Figure C3 can be directed to flow only through the boson propagator, and the diagram becomes independent of the external momentum in the small c limit. Since this suppression does not happen for higher-loop diagrams in general, the one-loop diagram becomes comparable to some two-loop diagrams with $L - L_f = 2$. Therefore, we have to include the two-loop diagrams for the self-energy in order to capture all leading order corrections. The rainbow diagram in Figure B.4(a) is smaller for the same reason as the one-loop diagram. Three and higher-loop diagrams remain negligible, and only Figure B.4(b) contributes to the leading order. The two-loop self-energy for patch n is given by

$$\Sigma^{2L(n)}(k_0,\vec{k}) = \frac{3\pi^2 v^2}{4}\int dpdq\ \left[\gamma_1 G_{\bar{n}}(k+q)\gamma_1 G_n(k+q+p)\gamma_1 G_{\bar{n}}(k+p)\gamma_1\right] D(q)D(p). \tag{C139}$$

It is noted that $\Sigma^{2L(n)}(k_0,0)$ is strictly smaller than $\Sigma^{1L(n)}(k_0,0)$, and only $\Sigma^{2L(n)}(0,\vec{k})$ is of the same order as $\Sigma^{1L(n)}(0,\vec{k})$. Therefore, we only compute $\Sigma^{2L(n)}(0,\vec{k})$. After performing the integrations over p_y, q_y, the self-energy for patch 1 becomes

$$\begin{aligned}\Sigma^{2L(1)}(0,\vec{k}) = \ & -\tfrac{3v^2}{2^8\pi^2c^2} i\gamma_1 \int dp_0 \int dq_0\ (\mathrm{sgn}(p_0)+\mathrm{sgn}(p_0+q_0))(\mathrm{sgn}(q_0)+\mathrm{sgn}(2p_0+q_0)) \times \\ & \int dp_x \int dq_x\ \tfrac{2w(p_x+q_x)+(3vk_x-k_y)}{4(p_0+q_0)^2+(2w(p_x+q_x)+(3vk_x-k_y))^2} \tfrac{1}{|p_0|+|p_x|} \tfrac{1}{|q_0|+|q_x|}.\end{aligned} \tag{C140}$$

We single out the factor of $(3vk_x - k_y)$ by rescaling $(p_0, p_x, q_0, q_x) \to |3vk_x - k_y|(p_0, p_x, q_0, q_x)$. To perform the p_x and q_x integrals, we introduce variables $a = \frac{1}{2}(p_x + q_x), b = \frac{1}{2}(p_x - q_x)$. After the straightforward integration over b, we rescale $a \to \frac{a}{w}$ to obtain

$$\begin{aligned}\Sigma^{2L(1)}(0,\vec{k}) &= -\tfrac{3v^2}{2^7\pi^2c^2} i\gamma_1(3vk_x - k_y)\int dp_0 \int dq_0 \\ &(\mathrm{sgn}(p_0) + \mathrm{sgn}(p_0+q_0))(\mathrm{sgn}(q_0) + \mathrm{sgn}(2p_0+q_0)) \int da\ \tfrac{4a+1}{4(p_0+q_0)^2+(4a+1)^2} \times \\ &\left(\frac{\log\left(\frac{(2|a|+w|p_0|)(2|a|+w|q_0|)}{w^2|p_0||q_0|}\right)}{2|a|+w(|p_0|+|q_0|)} - \frac{\log\left(\frac{w|q_0|}{2|a|+w|p_0|}\right)}{2|a|+w(|p_0|-|q_0|)} - \frac{\log\left(\frac{w|p_0|}{2|a|+w|q_0|}\right)}{2|a|-w(|p_0|-|q_0|)} \right), \end{aligned} \tag{C141}$$

where the frequency integrations are understood to have a UV cut-off, $\Lambda_3' = \frac{\Lambda}{|3vk_x - k_y|}$ in the rescaled variable. In the small w limit, the a integration diverges as $(\log(w))^2$. The sub-leading terms are suppressed compared to the one-loop diagram, and we drop them in the small w limit. The remaining frequency integrations are logarithmically divergent in the UV cut-off,

$$\Sigma^{2L(1)}(0,\vec{k}) = -i\gamma_1 \frac{3}{32\pi^2}\left(\frac{v}{c}\log\frac{c}{v}\right)^2 \log\left(\frac{\Lambda}{|3vk_x - k_y|}\right)(3vk_x - k_y)\,. \tag{C142}$$

This is of the same order as Eq. (C138) because of $\left(\frac{v}{c}\log\frac{c}{v}\right)^2 = 8v\log\frac{1}{c}$ to the leading order in v.

The vertex correction in Figure B.4(b) strengthens the bare vertex, and the two-loop self-energy has the same sign as the one-loop self-energy. In particular, both the one-loop and two-loop quantum corrections enhance nesting, and drive v to a smaller value at low energies. To remove the cut-off dependences of Eq. (C138) and Eq. (C142) in the quantum effective action, we add the counter term

$$\sum_{\sigma=\uparrow,\downarrow}\int dk\ \bar{\Psi}_{1,\sigma}(k)\left(i\gamma_1(Z_{2,1}vk_x + Z_{3,1}k_y)\right)\Psi_{1,\sigma}(k) \tag{C143}$$

with

$$\begin{aligned} Z_{2,1} &= \frac{15}{4\pi^2}v\,\log\left(\frac{1}{c}\right)\log\left(\frac{\Lambda}{\mu}\right), \\ Z_{3,1} &= -\frac{9}{4\pi^2}v\,\log\left(\frac{1}{c}\right)\log\left(\frac{\Lambda}{\mu}\right). \end{aligned} \tag{C144}$$

Counter terms for $n = 2, 3, 4$ are fixed by the four-fold rotational symmetry.

III-3 Upper bound for self-energy at two loops

In this section, we explicitly check that two-loop self-energy corrections $\Sigma^{2L}(k_0, \vec{k})$ that we did not compute, i.e. the diagram in Fig. B.4(a) and the frequency contribution of the diagram in Fig. B.4(b), are sub-leading in v, in agreement with Eq. (34). We take derivatives of $\Sigma^{2L}(k_0, \vec{k})$

with respect to k_0 and $\vec{k}$ in order to compute the logarithmic divergence for each contribution. Since we are only interested in verifying Eq. (34) up to logarithmic corrections, we compute these diagrams by setting all instances of $\log x \to 1$ in the calculation, where x is a function of the internal momenta and v, c. In particular, after differentiating with the appropriate variable, this allows us to set all external momenta and frequencies to zero, as well as all instances of c and w after the factor of $1/c$ from each mixed loop is scaled out, and ignore all arising logarithmic UV and IR divergences.

III-3 .1 Fig. B.4(b)

The self-energy from the diagram in Fig. B.4(b) is given by Eq. (C139). In order to find the contribution to Z_1, we set $n = 1$ for concreteness, rescale $p_x \to p_x/c$, $q_x \to q_x/c$ in the usual way, and set $c = 0$ and $w = 0$ in the integrand. We compute

$$\frac{\partial \Sigma^{2L(1)}(k_0,0)}{\partial k_0}\bigg|_{k_0=0} \propto \frac{v^2}{c^2} i\gamma_0 \int dp \int dq \tag{C145}$$

$$\begin{aligned}
&\{-2(p_0^2+p_y^2)(p_0+q_0)(q_0^2+q_y^2)(q_0(p_y^2+p_0(p_0+q_0))+p_0q_y^2)\\
&+(p_0^2+p_y^2)(q_0^2+q_y^2)(p_0^2+p_y^2+3p_0q_0+q_0^2+p_yq_y+q_y^2)((p_0+q_0)^2+(p_y+q_y)^2)\\
&-2(p_0^2+p_y^2)q_0(q_0(p_y^2+p_0(p_0+q_0))+p_0q_y^2)((p_0+q_0)^2+(p_y+q_y)^2)\\
&-2p_0(q_0^2+q_y^2)(q_0(p_y^2+p_0(p_0+q_0))+p_0q_y^2)((p_0+q_0)^2+(p_y+q_y)^2)\}\\
&\overline{(p_0^2+p_y^2)^2(q_0^2+q_y^2)^2((p_0+q_0)^2+(p_y+q_y)^2)^2\,(|p_0|+|p_x|)\,(|q_0|+|q_x|)},
\end{aligned} \tag{C146}$$

where the coefficients of proportionality in $\propto$ are just numerical coefficients. The integrals over p_y and q_y can be done without a cutoff. The integrals over p_x and q_x require a UV cutoff, but they give only a logarithmic contribution, which we ignore,

$$\frac{\partial \Sigma^{2L(1)}(k_0,0)}{\partial k_0}\bigg|_{k_0=0} \propto \frac{v^2}{c^2} i\gamma_0 \int dp_0 \int dq_0 \frac{(p_0+q_0)(\mathrm{sgn}(q_0)\mathrm{sgn}(2p_0+q_0)+1)(\mathrm{sgn}(p_0)+\mathrm{sgn}(p_0+q_0))}{(|q_0|+|2p_0+q_0|)^3}. \tag{C147}$$

We have cut of all divergences with arbitrary functions of the momenta, frequencies, UV cutoffs, and the velocities, and then set the logarithms of these functions to one. We can bound the integrand by ignoring the sgn functions,

$$\begin{aligned}
&\left|\int dp_0 \int dq_0 \frac{(p_0+q_0)(\mathrm{sgn}(q_0)\mathrm{sgn}(2p_0+q_0)+1)(\mathrm{sgn}(p_0)+\mathrm{sgn}(p_0+q_0))}{(|q_0|+|2p_0+q_0|)^3}\right|\\
&< \left|\int dp_0 \int dq_0 \frac{p_0+q_0}{(|q_0|+|2p_0+q_0|)^3}\right| \propto 1,
\end{aligned} \tag{C148}$$

and therefore

$$\left.\frac{\partial\Sigma^{2L(1)}(k_0,0)}{\partial k_0}\right|_{k_0=0} \propto \frac{v^2}{c^2} i\gamma_0. \tag{C149}$$

III-3 .2 Fig. B.4(a)

The self-energy from the diagram in Fig. B.4(a) is given by

$$\Sigma^{2L(n)}(k_0,\vec{k}) \propto v^2 \int dp \int dq\, \gamma_1 G_{\bar{n}}(k+p)\gamma_1 G_n(k+p+q)\gamma_1 G_{\bar{n}}(k+p)\gamma_1 D(q)D(p) \tag{C150}$$

Here, in computing this diagram, we do the integrations exactly up to numerical factors, without setting any logarithms of the integration variables to one. In order to find the contribution to Z_1, we set $n=1$, rescale the momenta as usual, set $c=w=0$ inside the integrand, and compute

$$\left.\frac{\partial\Sigma^{2L(1)}(k_0,0)}{\partial k_0}\right|_{k_0=0} \propto \frac{v^2}{c^2} i\gamma_0 \int dp \int dq \tag{C151}$$

$$\begin{aligned}
&(p_0^2+p_y^2)((p_0+q_0)^2+(p_y+q_y)^2)(3p_0^2+2p_0q_0+p_y(p_y+2q_y)) \\
&-2(p_0^2+p_y^2)(p_0+q_0)(p_0^3+p_0^2q_0-p_y^2q_0+p_0p_y(p_y+2q_y)) \\
&-4p_0((p_0+q_0)^2+(p_y+q_y)^2)(p_0^3+p_0^2q_0-p_y^2q_0+p_0p_y(p_y+2q_y)) \\
&\overline{(p_0^2+p_y^2)^3((p_0+q_0)^2+(p_y+q_y)^2)^2\,[|p_0|+|p_x|]\,[|q_0|+|q_x|]}.
\end{aligned} \tag{C152}$$

The proportionality sign $\propto$ indicates that there are purely numerical factors missing. We perform the integrals over q_x, p_x with the UV cutoffs Λ. Then we perform the integral over p_y, which gives

$$\begin{aligned}
\left.\frac{\partial\Sigma^{2L(1)}(k_0,0)}{\partial k_0}\right|_{k_0=0} \propto &\frac{v^2}{c^2} i\gamma_0 \int dp_0 \int dq_0 \log\left(1+\frac{\Lambda}{|p_0|}\right)\log\left(1+\frac{\Lambda}{|q_0|}\right) \\
&(2p_0+q_0)(\mathrm{sgn}(p_0+q_0)+\mathrm{sgn}(p_0))\int dq_y \frac{(2p_0+q_0)^2-3q_y^2}{((2p_0+q_0)^2+q_y^2)^3} = 0.
\end{aligned} \tag{C153}$$

Therefore, the contribution of this quantum correction to Z_1 is further suppressed by more powers of v though c and/or w compared to Eq. (34).

As noted below Fig. C4, $\Sigma^{2L(1)}(0,\vec{k})$ is also further suppressed by a factor of c compared to Eq. (34). This is because if we pass the external momentum through the top boson line so that its momentum is $p+k$, rescale $p_x \to p_x/c$ and set $c=0$ in the integrand, $\vec{k}$ disappears from the integral. Therefore, $\Sigma^{2L(1)}(0,\vec{k})$ comes with an additional suppression in c.

III-4 Vertex correction at one loop

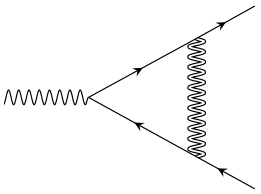

Figure C5: The one-loop diagram for the vertex correction.

The one-loop vertex correction in Fig. C5 is given by

$$\Gamma^{1L}(k,q) = \frac{\pi v}{2}\int dp\, \gamma_1 G^{(0)}_{\bar{n}}(p+k+q)\gamma_1 G^{(0)}_{n}(p+k)\gamma_1 D(p). \tag{C154}$$

We set all external momenta to zero except for k_0, which plays the role of an IR regulator. For $n=1$, it is convenient to rescale $(p_0,p_x,p_y)\to|k_0|(p_0,p_x/c,p_y)$. The p_0 integration gives

$$\begin{aligned}
\Gamma^{1L(1)}(k_0) = {}& \frac{\pi v}{2c}\gamma_1\frac{1}{(2\pi)^3}\int_{-\Lambda_0}^{\Lambda_0} dp_y \int dp_x \\
& \left\{\begin{array}{l}\big[\big((p_y-wp_x)(p_y+wp_x)^3+(-1+(|p_x|+c|p_y|)^2)^2\big)\big(1+(p_y-wp_x)^2+(|p_x|+c|p_y|)^2\big)+\\ (p_y-wp_x)(p_y+wp_x)\big(1+6(|p_x|+c|p_y|)^2+(|p_x|+c|p_y|)^4+(p_y-wp_x)^2(1+(|p_x|+c|p_y|)^2)\big)\\ +(p_y+wp_x)^2\big((-1+(|p_x|+c|p_y|)^2)^2+(p_y-wp_x)^2(1+(|p_x|+c|p_y|)^2)\big)\big]\log(|p_x|+c|p_y|)\end{array}\right\} \\
& -\tfrac{1}{2}\left\{\begin{array}{l}\big((p_y-wp_x)^2+(-1+|p_x|+c|p_y|)^2\big)\big((p_y+wp_x)^2+(-1+|p_x|+c|p_y|)^2\big)\\ \times\big((p_y-wp_x)^2+(1+|p_x|+c|p_y|)^2\big)\big((p_y+wp_x)^2+(1+|p_x|+c|p_y|)^2\big)\end{array}\right\} \\
& +\frac{\left\{\begin{array}{l}2\,\mathrm{arccot}(p_y+wp_x)\big(1+(p_y+wp_x)^2-(|p_x|+c|p_y|)^2\big)\\ +(p_y+wp_x)\log(1+(p_y+wp_x)^2)(1+(p_y+wp_x)^2+(|p_x|+c|p_y|)^2)\\ +\ \pi\,\mathrm{sgn}(p_y+wp_x)(|p_x|+c|p_y|)(-1+(p_y+wp_x)^2+(|p_x|+c|p_y|)^2)\end{array}\right\}}{2p_y\big((p_y+wp_x)^2+(-1+|p_x|+c|p_y|)^2\big)\big((p_y+wp_x)^2+(1+|p_x|+c|p_y|)^2\big)} \\
& +\frac{\left\{\begin{array}{l}2\,\mathrm{arccot}(p_y-p_xw)(1+(p_y-wp_x)^2-(|p_x|+c|p_y|)^2)\\ +(p_y-wp_x)\log(1+(p_y-wp_x)^2)(1+(p_y-wp_x)^2+(|p_x|+c|p_y|)^2)\\ +\ \pi\,\mathrm{sgn}(p_y-wp_x)(|p_x|+c|p_y|)(-1+(p_y-wp_x)^2+(|p_x|+c|p_y|)^2)\end{array}\right\}}{2p_y\big((p_y-wp_x)^2+(-1+|p_x|+c|p_y|)^2\big)\big((p_y-wp_x)^2+(1+|p_x|+c|p_y|)^2\big)},
\end{aligned}$$

where the rescaled cut-off for p_y is $\Lambda_0=\frac{\Lambda}{|k_0|}$. After the $\vec{p}$ integration, the logarithmically divergent contribution is obtained to be

$$\Gamma^{1L(1)}(k_0) = \frac{1}{4\pi}\frac{v}{c}\log\left(\frac{c}{v}\right)\log\left(\frac{\Lambda}{|k_0|}\right)\gamma_1 \tag{C155}$$

in the small v limit. The vertex corrections for different n are the same. The counter term for the vertex becomes

$$Z_{6,1}\, i\sqrt{\frac{\pi v}{2}} \sum_{n=1}^{4} \sum_{\sigma,\sigma'=\uparrow,\downarrow} \int dk \int dq\; \bar{\Psi}_{n,\sigma}(k+q)\Phi_{\sigma,\sigma'}(q)\gamma_1 \Psi_{\bar{n},\sigma'}(k) \tag{C156}$$

with

$$Z_{6,1} = -\frac{1}{4\pi}\frac{v}{c}\log\left(\frac{c}{v}\right)\log\left(\frac{\Lambda}{\mu}\right). \tag{C157}$$

III-5 Upper bound for vertex correction at two loops

In this section, we explicitly check that two-loop vertex corrections are sub-leading in v, in agreement with Eq. (34). The four quantum corrections to the vertex at two loops are shown in Fig. C6. As for the two-loop self-energy contributions, we compute these diagrams by setting

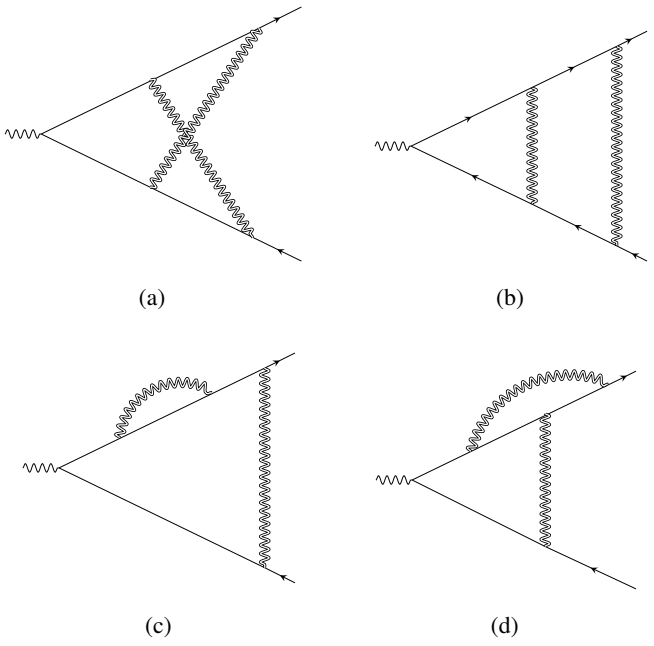

Figure C6: Two-loop diagrams that contribute to vertex corrections.

all instances of $\log x \to 1$ in the calculation, where x is a function of the internal momenta and v, c.

III-5 .1 Fig. B.6(a)

The vertex correction from Fig. B.6(a) is

$$\Gamma_1^{2L}(k,q) \propto v^2 \int dp \int d\tilde{p}\, \gamma_1 G_{\bar{n}}(k+p)\gamma_1 G_n(k+p+\tilde{p})\gamma_1 G_{\bar{n}}(k+q+p+\tilde{p})$$

$$\times \gamma_1 G_n(k+q+\tilde{p})\gamma_1 D(p)D(\tilde{p}). \tag{C158}$$

As usual, we fix $n=1$ for concreteness. We rescale $p_x \to p_x/c$, $\tilde{p}_x \to \tilde{p}_x/c$ in the usual way, and set $c=0$ in the integrand. We set $k=q=0$ and $w=0$, which gives

$$\begin{aligned}\Gamma_1^{2L,(1)}(0,0) &\propto \frac{v^2}{c^2} i\gamma_1 \int dp \int d\tilde{p} \frac{(p_0\tilde{p}_0+\tilde{p}_y p_y)((p_0+\tilde{p}_0)^2+(\tilde{p}_y+p_y)^2)}{\left[p_0^2+p_y^2\right]\left[\tilde{p}_0^2+\tilde{p}_y^2\right]\left[(p_0+\tilde{p}_0)^2+(p_y+\tilde{p}_y)^2\right]^2\left[|p_0|+|p_x|\right]\left[|\tilde{p}_0|+|\tilde{p}_x|\right]} \\ &\propto v^2 \frac{v^2}{c^2} i\gamma_1 \int dp_x d\tilde{p}_x \int d\tilde{p}_0 \frac{1}{\tilde{p}_0\left[|\tilde{p}_0|+|\tilde{p}_x|\right]} \int dp_0 \frac{1}{\left[|p_0|+|p_x|\right]} \frac{sgn(p_0)-sgn(p_0+\tilde{p}_0)}{(p_0+\tilde{p}_0)} \\ &\propto \frac{v^2}{c^2} i\gamma_1 \int d\tilde{p}_0 \int dp_0 \frac{sgn(p_0)-sgn(p_0+\tilde{p}_0)}{\tilde{p}_0(p_0+\tilde{p}_0)} \propto \frac{v^2}{c^2} i\gamma_1,\end{aligned}$$

where we have cut of all divergences with arbitrary functions of the momenta, frequencies, UV cutoffs, and the velocities, and then set the logarithms of these functions to one.

III-5 .2 Fig. B.6(b)

The vertex correction from Fig. B.6(b) is

$$\begin{aligned}\Gamma_2^{2L}(k,q) \propto v^2 \int dp \int d\tilde{p} \quad & \gamma_1 G_{\bar{n}}(k+p)\gamma_1 G_n(k+p+\tilde{p})\gamma_1 G_{\bar{n}}(k+q+p+\tilde{p}) \\ & \times \gamma_1 G_n(k+q+p)\gamma_1 D(p)D(\tilde{p}).\end{aligned} \tag{C159}$$

Again, we fix $n=1$ for concreteness, rescale the p_x and $\tilde{p}_x$ components of the momentum in the usual way, and set $w=c=0$ in the integrand, as well as $k=q=0$. This gives

$$\Gamma_2^{2L,(1)}(0,0) \propto \frac{v^2}{c^2} i\gamma_1 \int dp \int d\tilde{p} \frac{(p_0^2+p_y^2)(p_0^2+2p_0\tilde{p}_0+\tilde{p}_0^2+(\tilde{p}_y+p_y)^2)}{\left[p_0^2+p_y^2\right]^2\left[(p_0+\tilde{p}_0)^2+(p_y+\tilde{p}_y)^2\right]^2\left[|p_0|+|p_x|\right]\left[|\tilde{p}_0|+|\tilde{p}_x|\right]} \tag{C160}$$

$$\propto \frac{v^2}{c^2} i\gamma_1 \int dp_0 \,\mathrm{sgn}(p_0) \int d\tilde{p}_0 \frac{\mathrm{sgn}(\tilde{p}_0+p_0)}{(\tilde{p}_0+p_0)^2} \propto \frac{v^2}{c^2} i\gamma_1.$$

III-5 .3 Fig. B.6(c)

The vertex correction from Fig. B.6(c) is

$$\Gamma_3^{2L}(k,q) \propto v^2 \int dp \int d\tilde{p}\, \gamma_1 G_{\bar{n}}(k+p)\gamma_1 G_n(k+p+\tilde{p})\gamma_1 G_{\bar{n}}(k+p)\gamma_1 G_n(k+q+p)\gamma_1 D(p)D(\tilde{p}).$$

As before, this gives

$$\Gamma_3^{2L,(1)}(0,0) \propto \frac{v^2}{c^2} i\gamma_1 \int dp \int d\tilde{p} \frac{p_0^2+p_0\tilde{p}_0+p_y(\tilde{p}_y+p_y)}{\left[p_0^2+p_y^2\right]^2\left[(p_0+\tilde{p}_0)^2+(p_y+\tilde{p}_y)^2\right]\left[|p_0|+|p_x|\right]\left[|\tilde{p}_0|+|\tilde{p}_x|\right]} \tag{C161}$$

$$\propto \frac{v^2}{c^2} i\gamma_1 \int dp_0 \frac{\mathrm{sgn}(p_0)}{p_0^2} \int d\tilde{p}_0 \,\mathrm{sgn}(\tilde{p}_0 + p_0) \propto \frac{v^2}{c^2} i\gamma_1 .$$

III-5 .4 Fig. B.6(d)

The vertex correction from Fig. B.6(d) is

$$\Gamma_4^{2L}(k,q) \propto v^2 \int dp \int d\tilde{p}\, \gamma_1 G_{\bar{n}}(k+p)\gamma_1 G_n(k+p+\tilde{p})\gamma_1 G_{\bar{n}}(k+\tilde{p})\gamma_1 G_n(k+q+\tilde{p})\gamma_1 D(p) D(\tilde{p}).$$

As before, this gives

$$\begin{aligned}
\Gamma_4^{2L,(1)}(0,0) &\propto \frac{v^2}{c^2} i\gamma_1 \int dp \int d\tilde{p} \frac{p_0^2 + p_0\tilde{p}_0 + p_y(\tilde{p}_y + p_y)}{\left[p_0^2 + p_y^2\right]\left[\tilde{p}_0^2 + \tilde{p}_y^2\right]\left[(p_0+\tilde{p}_0)^2 + (p_y+\tilde{p}_y)^2\right]\left[|p_0| + |p_x|\right]\left[|\tilde{p}_0| + |\tilde{p}_x|\right]} \\
&\propto i\gamma_1 \frac{v^2}{c^2} \int dp_0 \int d\tilde{p}_0 \left(\frac{\mathrm{sgn}(p_0)\mathrm{sgn}(p_0+2\tilde{p}_0)+1}{|\tilde{p}_0|(|p_0| + |p_0+2\tilde{p}_0|)} + \frac{\mathrm{sgn}(p_0+2\tilde{p}_0)(\mathrm{sgn}(\tilde{p}_0) - \mathrm{sgn}(\tilde{p}_0+p_0))}{|p_0|(|p_0| + |p_0+2\tilde{p}_0|)} \right) \\
&< 2\frac{v^2}{c^2} i\gamma_1 \int dp_0 \int d\tilde{p}_0 \left(\frac{1}{|\tilde{p}_0|(|p_0| + |p_0+2\tilde{p}_0|)} + \frac{1}{|p_0|(|p_0| + |p_0+2\tilde{p}_0|)} \right) \lesssim \frac{v^2}{c^2} i\gamma_1 .
\end{aligned} \tag{C162}$$

III-6 The beta function for v

The counter terms in Eqs. (C131), (C143), (C156) are added to the action in Eq. (30) to obtain the bare action,

$$\begin{aligned}
\mathcal{S}_B = &\sum_{n=1}^{4} \sum_{\sigma=\uparrow,\downarrow} \int dk\; \bar{\Psi}_{n,\sigma}(k) \left[iZ_1 \gamma_0 k_0 + i\gamma_1 \varepsilon_n^B(\vec{k}) \right] \Psi_{n,\sigma}(k) \\
&+ iZ_6 \sqrt{\frac{\pi v}{2}} \sum_{n=1}^{4} \sum_{\sigma,\sigma'} \int dk\; dq \left[\bar{\Psi}_{\bar{n},\sigma}(k+q) \Phi_{\sigma,\sigma'}(q) \gamma_1 \Psi_{n,\sigma'}(k) \right],
\end{aligned} \tag{C163}$$

where $\varepsilon_1^B(\vec{k}) = Z_2 v k_x + Z_3 k_y$, $\varepsilon_2^B(\vec{k}) = -Z_3 k_x + Z_2 v k_y$, $\varepsilon_3^B(\vec{k}) = Z_2 v k_x - Z_3 k_y$, $\varepsilon_4^B(\vec{k}) = Z_3 k_x + Z_2 v k_y$. Here $Z_n = 1 + Z_{n,1}$ is given in Eqs. (C132), (C144) and (C157). The bare action generates the physical quantum effective action which is expressed solely in terms of the renormalized coupling v measured at an energy scale μ. The relationship between the renormalized and bare quantities is given by

$$k_{x,B} = k_x;\; k_{y,B} = k_y;\; k_{0,B} = \frac{Z_1}{Z_3} k_0;\; v_B = \frac{Z_2}{Z_3} v;\; \Psi_B(k_B) = \frac{Z_3}{Z_1^{\frac{1}{2}}} \Psi(k);\; \Phi_B(k_B) = \frac{Z_3^{\frac{1}{2}} Z_6}{Z_1 Z_2^{\frac{1}{2}}} \Phi(k). \tag{C164}$$

The beta function for v is obtained by requiring that the bare coupling v_B does not depend on μ,

$$\left(Z_2 Z_3 + v\left(\frac{\partial Z_2}{\partial v} Z_3 - Z_2 \frac{\partial Z_3}{\partial v}\right)\right)\beta_v + v\left(\frac{\partial Z_2}{\partial \log \mu} Z_3 - Z_2 \frac{\partial Z_3}{\partial \log \mu}\right) = 0. \tag{C165}$$

This gives the beta function which describes the flow of v under the change of the scale μ,

$$\frac{dv}{d\log\mu} = \frac{6}{\pi^2} v^2 \log\left[4\left(\frac{1}{v \log 1/v}\right)^{\frac{1}{2}}\right] \tag{C166}$$

to the leading order in v. Introducing a logarithmic scale $\ell = -\log\mu$, the beta function can be rewritten as $\frac{dv}{d\ell} = \frac{3}{\pi^2} v^2 \log v$ up to $\log\log v$. The solution is given by

$$Ei[\log 1/v(\ell)] = Ei[\log 1/v(0)] + \frac{3}{\pi^2}\ell, \tag{C167}$$

where $Ei(x)$ is the exponential integral function, which goes as $Ei(x) = e^x\left[\frac{1}{x} + O(1/x^2)\right]$ in the large x limit. Therefore, v flows to zero as

$$v(\ell) = \frac{\pi^2}{3}\frac{1}{\ell\ \log\ell} \tag{C168}$$

for $\ell \gg \frac{1}{v(0)\log 1/v(0)}$. For sufficiently large ℓ, $v(\ell)$ decays to zero in a manner which is independent of its initial value. The velocity of the collective mode flows to zero at a slower rate,

$$c(\ell) = \frac{\pi}{4\sqrt{3}}\frac{1}{\sqrt{\ell}}, \tag{C169}$$

and the ratio $w = v/c$ flows to zero as

$$w(\ell) = \frac{4\pi}{\sqrt{3}}\frac{1}{\sqrt{\ell}\log\ell}. \tag{C170}$$

Similarly, the multiplicative renormalization for the frequency and fields in Eq. (C164) generates the deviation of the dynamical critical exponent from one and the anomalous dimensions for the fields,

$$\eta_\phi = \frac{d}{d\ \log\mu}\log\left(\frac{Z_3^{\frac{1}{2}} Z_6}{Z_1 Z_2^{\frac{1}{2}}}\right), \tag{C171}$$

$$\eta_\psi = \frac{d}{d\ \log\mu}\log\left(\frac{Z_3}{Z_1^{\frac{1}{2}}}\right), \tag{C172}$$

$$z = 1 + \frac{d}{d\ \log\mu}\log\left(\frac{Z_1}{Z_3}\right) \tag{C173}$$

which reduce to the expressions in Eqs. (38) to the leading order in v.

IV Derivation of the scaling forms for physical observables

In this section, we derive the expressions for the Green's functions and the specific heat in Eqs. (39), (41) and (43).

IV-1 The Green's function

We derive the form of the electron Green's function near hot spot $1+$. The Green's functions for all other hot spots are determined from that of $1+$ by symmetry. The Green's function satisfies the renormalization group equation,

$$\left[\frac{1-2\eta_\psi-(z-1)}{z}+k_0\frac{\partial}{\partial k_0}+\frac{1}{z}\vec{k}\cdot\frac{\partial}{\partial\vec{k}}-\frac{\beta_v}{z}\frac{\partial}{\partial v}\right]G_{1+}(k_0,\vec{k};v)=0. \tag{D174}$$

The solution becomes

$$G_{1+}(k_0,\vec{k};v)=e^{\int_0^l\frac{1-2\eta_\psi(v(l'))-[z(v(l'))-1]}{z(v(l'))}dl'}G_{1+}\left(e^l k_0, e^{\int_0^l\frac{1}{z(v(l'))}dl'}\vec{k};v(l)\right), \tag{D175}$$

where $v(l)$ satisfies $\frac{dv(l)}{dl}=-\frac{\beta_v}{z(v)}$ with the initial condition $v(0)=v$, and $z(v)$ and $\eta_\psi(v)$ depend on l through $v(l)$. We write $\frac{1-2\eta_\psi-(z-1)}{z}=\frac{1}{z}-2\tilde{\eta}_\psi$, where $\tilde{\eta}_\psi=\frac{1}{2}\frac{\partial\log Z_3}{\partial\log\mu}$ to the leading order in v. Although $\tilde{\eta}_\psi$ is sub-leading compared to $1/z$, we keep it because only $\tilde{\eta}_\psi$ contributes to the net anomalous dimension of the propagator. From Eqs. (C168)-(C170), one obtains the solution to the scaling equation,

$$G_{1+}(k_0,\vec{k};v)=\exp\left(l-2\sqrt{3}\frac{\sqrt{l}}{\log(l)}-\frac{3}{8}\log l\right)G_{1+}\left(e^l k_0,\exp\left(l-2\sqrt{3}\frac{\sqrt{l}}{\log(l)}\right)\vec{k},\frac{\pi^2}{3}\frac{1}{l\log(l)}\right) \tag{D176}$$

in the large l limit. We choose $l=\log(1/k_0)$ and take the small $k_0>0$ limit with $\exp\left(l-2\sqrt{3}\frac{\sqrt{l}}{\log(l)}\right)\vec{k}\sim 1$. By using the fact that the Green's function is given by $G_{1+}(k_0,\vec{k};v)=(ik_0+vk_x+k_y)^{-1}$ in the small v limit, we readily obtain

$$G_{1+}(k_0,\vec{k};v)=\frac{1}{F_\psi(k_0)\left[ik_0\ F_z(k_0)+\left(\frac{\pi^2}{3}\frac{k_x}{\log\frac{1}{k_0}\ \log\log\frac{1}{k_0}}+k_y\right)\right]} \tag{D177}$$

in the low-energy limit with fixed $\frac{\vec{k}}{k_0 F_z(k_0)}$, where $F_\psi(k_0) = \left(\log \frac{1}{k_0}\right)^{\frac{3}{8}}$ and $F_z(k_0) = e^{2\sqrt{3}\frac{\left(\log \frac{1}{k_0}\right)^{1/2}}{\log\log \frac{1}{k_0}}}$. The analytic continuation to the real frequency gives Eq. (39).

Similarly, the Green's function of the boson satisfies

$$\left[\frac{1-2\eta_\phi-(z-1)}{z} + q_0\frac{\partial}{\partial q_0} + \frac{1}{z}\vec{q}\cdot\frac{\partial}{\partial \vec{q}} - \frac{\beta_c}{z}\frac{\partial}{\partial c}\right] D(q_0,\vec{q};c) = 0, \tag{D178}$$

where $\beta_c = \frac{dc}{d\log\mu}$. Here we view the boson propagator as a function of c instead of v because it depends on v only through c to the leading order. However, this does not affect any physical observable since in the end there is only one independent parameter. The solution to the scaling equation takes the form,

$$D(q_0,\vec{q},c) = \exp\left(l - \frac{2\sqrt{l}}{\sqrt{3}} - 2\sqrt{3}\frac{\sqrt{l}}{\log l}\right) D\left(e^l q_0, \exp\left(l - 2\sqrt{3}\frac{\sqrt{l}}{\log(l)}\right)\vec{q}; \frac{\pi}{4\sqrt{3}}\frac{1}{\sqrt{l}}\right). \tag{D179}$$

By choosing $l = \log(1/q_0)$ and using the fact that the boson propagator is given by Eq. (32) in the limit of small v and c, we obtain

$$D(q_0,\vec{q}) = \frac{1}{F_\phi(q_0)\left(|q_0|F_z(q_0) + \frac{\pi}{4\sqrt{3}}\frac{|q_x|+|q_y|}{\left(\log\frac{1}{q_0}\right)^{1/2}}\right)} \tag{D180}$$

in the low-energy limit with fixed $\frac{\vec{q}}{q_0 F_z(q_0)}$. Here $F_\phi(q_0) \equiv e^{\frac{2}{\sqrt{3}}\left(\log\frac{1}{q_0}\right)^{1/2}}$ is a universal function which describes the contribution from the boson anomalous dimension. The analytic continuation gives the retarded correlation function in Eq. (41).

IV-2 Free energy

Here we compute the leading contribution to the free energy which is generated from the quadratic action of the dressed boson,

$$f_B(T) = \int \frac{d\vec{k}}{(2\pi)^2} f_B(\vec{k},T), \tag{D181}$$

where $f_B(\vec{k},T)$ is the contribution from the mode with momentum $\vec{k}$,

$$f_B(\vec{k},T) = \frac{3}{2}\left(T\sum_{\omega_m} - \int\frac{\mathrm{d}\omega_m}{2\pi}\right)\log\left[|\omega_m| + \varepsilon(\vec{k})\right] \tag{D182}$$

with $\varepsilon(\vec{k}) = c(|k_x| + |k_y|)$ and $\omega_m = 2\pi T m$. The thermal mass is ignored because it is higher order in v, and the temperature independent ground state energy is subtracted.

Using the identity $\log a = -\int_0^\infty \frac{\mathrm{d}x}{x}\left(e^{-xa} - e^{-x}\right)$, we write the free energy per mode as

$$f_B(\vec{k}, T) = -\frac{3}{2}\left(T\sum_{\omega_m} - \int \frac{\mathrm{d}\omega_m}{2\pi}\right)\int_0^\infty \frac{\mathrm{d}x}{x}\left(e^{-x(|\omega_m| + \varepsilon(\vec{k}))} - e^{-x}\right). \tag{D183}$$

The summation over the Matsubara frequency results in

$$f_B(\vec{k}, T) = -\frac{3T}{2}\int_0^\infty \frac{\mathrm{d}x}{x}\left(\coth(\pi T x) - \frac{1}{\pi T x}\right)e^{-x\varepsilon(\vec{k})}. \tag{D184}$$

For $\varepsilon(\vec{k}) \gg T$, the free energy is suppressed only algebraically,

$$f_B(\vec{k}, T) \quad = -\tfrac{\pi}{2}\tfrac{T^2}{\varepsilon(\vec{k})}\left(1 + O(T/\varepsilon(\vec{k}))\right). \tag{D185}$$

This is in contrast to the non-interacting boson, whose contribution is exponentially suppressed at large momenta. Due to the relatively large contribution from high momentum modes, the bosonic free energy becomes unbounded without a UV cut-off. This leads to a violation of hyperscaling.

$$f_B(T) \sim -T^2\tilde{\Lambda}, \tag{D186}$$

where $\tilde{\Lambda}$ is a UV cut-off associated with irrelevant terms as is discussed in the Appendix B.

Eq. (D186) is obtained without including the renormalization of the velocity and anomalous dimensions in Eq. (38), which alter the scaling at intermediate energy scales. In order to take those into account, we consider the scaling equation for f_B,

$$\left[\left(1 + \frac{2}{z}\right) - T\frac{\partial}{\partial T} + \frac{\beta_c}{z}\frac{\partial}{\partial c} - \frac{\tilde{\Lambda}}{z}\frac{\partial}{\partial\tilde{\Lambda}}\right]f_B(T, c, \tilde{\Lambda}) = 0. \tag{D187}$$

The solution takes the form,

$$f_B(T, c, \tilde{\Lambda}) = e^{-\int_0^l \mathrm{d}l'\left(1 + \frac{2}{z(l')}\right)} f_B\left(e^l T, c(l), e^{\int_0^l \frac{\mathrm{d}l'}{z(l')}}\tilde{\Lambda}\right), \tag{D188}$$

where $c(l)$ satisfies $\frac{dc(l)}{dl} = -\frac{\beta_c}{z(c)}$ with the initial condition $c(0) = c$. In the large l limit, $z \approx 1$ and $c(l)$ is given by Eq. (C169). By choosing $l = \log 1/T$ and using the fact that f_B is linearly proportional to $\tilde{\Lambda}$, we obtain

$$f_B \sim \tilde{\Lambda}T^2 F_z(T). \tag{D189}$$

This is the dominant term at low temperatures because the contribution of free electrons away from the hot spots only goes as T^2. The contributions from vertex corrections are sub-leading in v. Therefore, the specific heat in the low temperature limit is given by Eq. (43).

Bibliography

[1] M. Kardar, Statistical physics of fields (Cambridge University Press, 2007).

[2] D. Sornette,
Critical phenomena in natural sciences: chaos, fractals, selforganization and disorder: concepts and tools (Springer Science & Business Media, 2006).

[3] S. Sachdev, Quantum phase transitions (Wiley Online Library, 2007).

[4] X.-G. Wen,
Quantum field theory of many-body systems: from the origin of sound to an origin of light and electrons (Oxford University Press on Demand, 2004).

[5] L. Landau, Sov. Phys. JETP **3**, 920 (1957).

[6] H. Bruus and K. Flensberg,
Many-body quantum theory in condensed matter physics: an introduction (Oxford University Press, 2004).

[7] A. A. Abrikosov, L. P. Gorkov, and I. E. Dzyaloshinski,
Methods of quantum field theory in statistical physics (Courier Corporation, 2012).

[8] R. Shankar, Rev. Mod. Phys. **66**, 129 (1994).

[9] J. Polchinski, ArXiv High Energy Physics - Theory e-prints (1992), hep-th/9210046 .

[10] K. G. Wilson, Reviews of Modern Physics **47**, 773 (1975).

[11] G. Baym and C. Pethick, Landau Fermi-liquid theory: concepts and applications (John Wiley & Sons, 2008).

[12] A. J. Schofield, Contemporary Physics **40**, 95 (1999).

[13] J. A. Hertz, Phys. Rev. B **14**, 1165 (1976).

[14] A. J. Millis, Phys. Rev. B **48**, 7183 (1993).

[15] T. Holstein, R. E. Norton, and P. Pincus, Phys. Rev. B **8**, 2649 (1973).

[16] M. Y. Reizer, Phys. Rev. B **40**, 11571 (1989).

[17] P. A. Lee and N. Nagaosa, Phys. Rev. B **46**, 5621 (1992).

[18] B. L. Altshuler, L. B. Ioffe, and A. J. Millis, Phys. Rev. B **50**, 14048 (1994).

[19] J. Polchinski, Nuclear Physics B **422**, 617 (1994).

[20] B. I. Halperin, P. A. Lee, and N. Read, Physical Review B **47**, 7312 (1993).

[21] C. Nayak and F. Wilczek, Nuclear Physics B **430**, 534 (1994).

[22] P. A. Lee, N. Nagaosa, and X.-G. Wen, Reviews of modern physics **78**, 17 (2006).

[23] H. Watanabe and A. Vishwanath, Proceedings of the National Academy of Sciences **111**, 16314 (2014).

[24] S.-i. Tomonaga, Progress of Theoretical Physics **5**, 544 (1950).

[25] J. Luttinger, Journal of Mathematical Physics **4**, 1154 (1963).

[26] D. C. Mattis and E. H. Lieb, Journal of Mathematical Physics **6**, 304 (1965).

[27] F. Haldane, Journal of Physics C: Solid State Physics **14**, 2585 (1981).

[28] M. Brando, D. Belitz, F. Grosche, and T. Kirkpatrick, Reviews of Modern Physics **88**, 025006 (2016).

[29] V. Oganesyan, S. A. Kivelson, and E. Fradkin, Physical Review B **64**, 195109 (2001).

[30] K. Sun, B. M. Fregoso, M. J. Lawler, and E. Fradkin, Physical Review B **78**, 085124 (2008).

[31] T. Moriya, Y. Takahashi, and K. Ueda, Journal of the Physical Society of Japan **59**, 2905 (1990), http://dx.doi.org/10.1143/JPSJ.59.2905 .

[32] P. Monthoux, A. V. Balatsky, and D. Pines, Phys. Rev. B **46**, 14803 (1992).

[33] S. Sachdev, A. V. Chubukov, and A. Sokol, Physical Review B **51**, 14874 (1995).

[34] Y. B. Kim, A. Furusaki, X.-G. Wen, and P. A. Lee, Phys. Rev. B **50**, 17917 (1994).

[35] P. Säterskog, B. Meszena, and K. Schalm, ArXiv e-prints (2016), arXiv:1612.05326 [cond-mat.str-el] .

[36] S.-S. Lee, Phys. Rev. B **80**, 165102 (2009).

[37] M. A. Metlitski and S. Sachdev, Phys. Rev. B **82**, 075127 (2010).

[38] M. A. Metlitski and S. Sachdev, Phys. Rev. B **82**, 075128 (2010).

[39] C. Nayak and F. Wilczek, Nuclear Physics B **417**, 359 (1994).

[40] D. F. Mross, J. McGreevy, H. Liu, and T. Senthil, Phys. Rev. B **82**, 045121 (2010).

[41] T. Holder and W. Metzner, Phys. Rev. B **92**, 041112 (2015).

[42] D. Dalidovich and S.-S. Lee, Phys. Rev. B **88**, 245106 (2013).

[43] S. Sur and S.-S. Lee, Phys. Rev. B **91**, 125136 (2015).

[44] T. Helm, M. V. Kartsovnik, I. Sheikin, M. Bartkowiak, F. Wolff-Fabris, N. Bittner, W. Biberacher, M. Lambacher, A. Erb, J. Wosnitza, and R. Gross, Phys. Rev. Lett. **105**, 247002 (2010).

[45] E. M. Motoyama, G. Yu, I. M. Vishik, O. P. Vajk, P. K. Mang, and M. Greven, Nature **445**, 186 (2007).

[46] K. Hashimoto, K. Cho, T. Shibauchi, S. Kasahara, Y. Mizukami, R. Katsumata, Y. Tsuruhara, T. Terashima, H. Ikeda, M. A. Tanatar, H. Kitano, N. Salovich, R. W. Giannetta, P. Walmsley, A. Carrington, R. Prozorov, and Y. Matsuda, Science **336**, 1554 (2012), http://www.sciencemag.org/content/336/6088/1554.full.pdf .

[47] T. Park, F. Ronning, H. Yuan, M. Salamon, R. Movshovich, J. Sarrao, and J. Thompson, Nature **440**, 65 (2006).

[48] J. Custers, P. Gegenwart, H. Wilhelm, K. Neumaier, Y. Tokiwa, O. Trovarelli, C. Geibel, F. Steglich, C. Pépin, and P. Coleman, Nature **424**, 524 (2003), cond-mat/0308001 .

[49] C. Xu, M. Müller, and S. Sachdev, Phys. Rev. B **78**, 020501 (2008), arXiv:0804.4293 [cond-mat.str-el] .

[50] C. Fang, H. Yao, W.-F. Tsai, J. Hu, and S. A. Kivelson, Phys. Rev. B **77**, 224509 (2008), arXiv:0804.3843 [cond-mat.str-el] .

[51] A. Abanov, A. V. Chubukov, and J. Schmalian, Advances in Physics **52**, 119 (2003), http://www.tandfonline.com/doi/pdf/10.1080/0001873021000057123 .

[52] A. Abanov and A. V. Chubukov, Phys. Rev. Lett. **84**, 5608 (2000).

[53] A. Abanov and A. Chubukov, Phys. Rev. Lett. **93**, 255702 (2004).

[54] S. Sur and S.-S. Lee, Phys. Rev. B **94**, 195135 (2016).

[55] Y. Huh and S. Sachdev, Phys. Rev. B **78**, 064512 (2008).

[56] A. Schlief, P. Lunts, and S.-S. Lee, Physical Review X **7**, 021010 (2017), arXiv:1608.06927 [cond-mat.str-el] .

[57] A. Schlief, P. Lunts, and S.-S. Lee, in preparation .

[58] T. Senthil and R. Shankar, Phys. Rev. Lett. **102**, 046406 (2009).

[59] C. Varma, P. B. Littlewood, S. Schmitt-Rink, E. Abrahams, and A. Ruckenstein, Physical Review Letters **63**, 1996 (1989).

[60] M. Brando, D. Belitz, F. M. Grosche, and T. R. Kirkpatrick, Rev. Mod. Phys. **88**, 025006 (2016).

[61] D. Belitz, T. R. Kirkpatrick, M. T. Mercaldo, and S. L. Sessions, Phys. Rev. B **63**, 174428 (2001).

[62] D. Belitz, T. R. Kirkpatrick, and J. Rollbühler, Phys. Rev. Lett. **93**, 155701 (2004).

[63] A. Schlief, P. Lunts, and S.-S. Lee, ArXiv e-prints (2016), arXiv:1608.06927 [cond-mat.str-el] .

[64] A. V. Chubukov and J. Schmalian, Phys. Rev. B **72**, 174520 (2005).

[65] E. Berg, M. A. Metlitski, and S. Sachdev, Science **338**, 1606 (2012), http://www.sciencemag.org/content/338/6114/1606.full.pdf .

[66] K. B. Efetov, H. Meier, and C. Pepin, Nat Phys **9**, 442 (2013), article.

[67] Y. Wang, A. Abanov, B. L. Altshuler, E. A. Yuzbashyan, and A. V. Chubukov, Phys. Rev. Lett. **117**, 157001 (2016).

[68] H. Meier, C. Pépin, M. Einenkel, and K. B. Efetov, Phys. Rev. B **89**, 195115 (2014).

[69] S. Sur and S.-S. Lee, Phys. Rev. B **90**, 045121 (2014).

[70] N. Seiberg, Physics Letters B **318**, 469 (1993).

[71] A. L. Fitzpatrick, S. Kachru, J. Kaplan, and S. Raghu, Phys. Rev. B **88**, 125116 (2013).

[72] P. Lunts, A. Schlief, and S.-S. Lee, Phys. Rev. B **95**, 245109 (2017).

[73] S. A. Maier and P. Strack, Phys. Rev. B **93**, 165114 (2016).

[74] C. M. Varma, Phys. Rev. Lett. **115**, 186405 (2015).

[75] J. M. Luttinger and J. C. Ward, Phys. Rev. **118**, 1417 (1960).

[76] A. A. Patel, P. Strack, and S. Sachdev, Phys. Rev. B **92**, 165105 (2015).

[77] D. Scalapino, E. Loh Jr, and J. Hirsch, Physical Review B **34**, 8190 (1986).

[78] K. Miyake, S. Schmitt-Rink, and C. M. Varma, Phys. Rev. B **34**, 6554 (1986).

[79] Z.-X. Li, F. Wang, H. Yao, and D.-H. Lee, ArXiv e-prints (2015), arXiv:1512.04541 [cond-mat.supr-con] .

[80] D. T. Son, Phys. Rev. D **59**, 094019 (1999).

[81] M. A. Metlitski, D. F. Mross, S. Sachdev, and T. Senthil, Phys. Rev. B **91**, 115111 (2015).

[82] S. Lederer, Y. Schattner, E. Berg, and S. A. Kivelson, Phys. Rev. Lett. **114**, 097001 (2015).

[83] M. Horio, T. Adachi, Y. Mori, A. Takahashi, T. Yoshida, H. Suzuki, L. C. C. Ambolode II, K. Okazaki, K. Ono, H. Kumigashira, H. Anzai, M. Arita, H. Namatame, M. Taniguchi, D. Ootsuki, K. Sawada, M. Takahashi, T. Mizokawa, Y. Koike, and A. Fujimori, Nature Communications **7**, 10567 EP (2016), article.

[84] E. Abrahams and P. Wolfle, Proceedings of the National Academy of Sciences **109**, 3238 (2012), http://www.pnas.org/content/109/9/3238.full.pdf .

[85] S. D. Wilson, P. Dai, S. Li, S. Chi, H. J. Kang, and J. W. Lynn, Nature **442**, 59 (2006).

[86] N. P. Armitage, D. H. Lu, C. Kim, A. Damascelli, K. M. Shen, F. Ronning, D. L. Feng, P. Bogdanov, Z.-X. Shen, Y. Onose, Y. Taguchi, Y. Tokura, P. K. Mang, N. Kaneko, and M. Greven, Phys. Rev. Lett. **87**, 147003 (2001).

[87] F. Schmitt, W. S. Lee, D.-H. Lu, W. Meevasana, E. Motoyama, M. Greven, and Z.-X. Shen, Phys. Rev. B **78**, 100505 (2008).